



Title	Study of Phenylazothiazoles as Visible-Light Photoswitches
Author(s)	林, 潤澤
Citation	北海道大学. 博士(生命科学) 甲第15776号
Issue Date	2024-03-25
DOI	10.14943/doctoral.k15776
Doc URL	http://hdl.handle.net/2115/91880
Type	theses (doctoral)
File Information	Runze_Lin.pdf



[Instructions for use](#)

Study of Phenylazothiazoles as Visible-Light

Photoswitches

(可視光分子スイッチとしてのフェニルアゾチアゾール類の
研究)

A Thesis

Submitted for the degree of

Doctor of Life Science

By

Runze Lin

Laboratory of Smart Molecules

Transdisciplinary Life Science Course

Graduate School of Life Science

Hokkaido University

March, 2024

Table of Contents

1. Introduction.....	3
1.1 Using light in therapy.....	3
1.2 Photopharmacology.....	4
1.3 Photoswitches.....	5
1.4 Heteroaryl azo-photoswitches.....	7
2. Results and discussion.....	10
2.1 Synthesis of Phenylazothiazoles.....	10
2.1.1 NMR spectra (^1H , ^{13}C) and Mass spectra of PAT 1-11.....	12
2.2 Photoisomerization and photophysical properties of Phenylazothiazoles.....	26
2.2.1 Measurement of isomer conversion at PSS by NMR (PAT 1–5, 9 and 11).....	33
2.2.2 Measurement of isomer conversion at PSS by absorption spectra (PAT 11).....	37
2.2.3 Absorption spectra of PAT derivatives.....	38
2.2.4 Laser flash photolysis.....	42
2.2.5 Isomerization quantum yields.....	43
2.2.6 Photophysical and thermal isomerization properties of PATs in aqueous media.....	78
2.3 X-ray single-crystal structures of Phenylazothiazoles.....	80
2.4 Theoretical calculations.....	81
2.4.1 Time-dependent density-functional theory (TDDFT) calculations.....	85
2.5 Reductive stability.....	96
3. Conclusions.....	98
4. Experimental Section.....	99
4.1 Experimental and instrumental methods.....	99
4.2 Synthesis.....	100
4.3 Measurement of isomer conversion at PSS by absorption spectra (PAT 11).....	104
4.4 Methods for isomerization quantum yields.....	106
4.5 Half-lives, Arrhenius plots and Eyring Plots.....	109
4.6 Single crystal X-ray structure analysis.....	110
5. References.....	111

1. Introduction

1.1 Using light in therapy

Pharmacotherapy involves the administration of drugs to treat diseases and alleviate symptoms.¹ The advancement in pharmacotherapy has greatly provided humanity with a higher quality of life. However, the development of pharmacotherapy is constrained by one main factor: the poor selectivity of drugs, which originates from the drug affinity for targets other than indeed² as well as the spatial and temporal uncontrolled drug efficacy. Such poor drug selectivity will lead to many problems such as side effect³ or drug resistance.⁴

To improve the spatial and temporal selectivity of drugs, recently, some strategies have emerged aiming at establishing an external modality using the irradiation of light.⁵⁻⁸ The combination of light and therapeutic effects has long captured the interest of humanity for thousands of years.⁹ Since light is the most readily available natural energy source, and light can serve as a non-invasive regulatory tool, delivering stimuli precisely with negligible toxicity or pollution. Till now, one major strategy, photodynamic therapy (PDT) has already been used in clinical treatment achieving spatial and temporal control (Figure 1a). Under the action of photosensitizer, energy is transferred from $^3\text{O}_2$ to $^1\text{O}_2$ upon light irradiation.¹⁰⁻¹¹ However, such strategy shows no target selectivity in the irradiated region since the generated $^1\text{O}_2$ will kill both normal and abnormal cells. Another example of such strategies is photoreactive caged-compounds (Figure 1b).¹²⁻¹⁴ The drug molecules caged with photocleavable leaving group are initially inactive, upon light irradiation they will cleavage and release the bioactive parts. But still, the problems of this method are that it's not able to switch the drug activity reversibly between a high efficacy state and a low efficacy state, as well as the release of potentially harmful leaving groups.

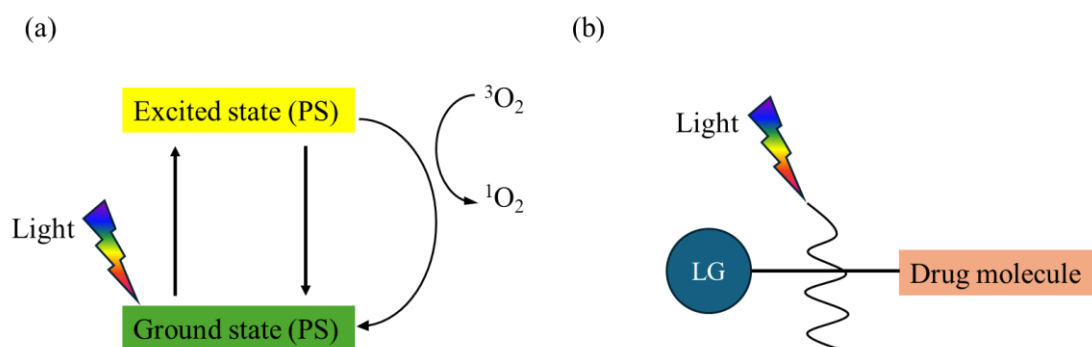


Figure 1. Figure showing two methods combining light with therapy: (a) photodynamic therapy (PDT) and (b) photocleavable drugs.

1.2 Photopharmacology

Now photopharmacology, another strategy combining light as regulatory tool, is raising more and more attentions to overcome the aforementioned drawbacks. The principle of photopharmacology is to introduce a photoswitching motif into the bioactive molecules, endowing the molecules with photoswitchability.¹⁵ That is, the bioactivity of molecules can be freely switched on and off by light irradiation (Figure 2a). Consequently, dynamic regulation of bio-systems can be accomplished in any time and space. For example, Feringa and co-workers reported a photoswitching antibiotic by incorporating an azobenzene motif into quinolones (Figure 2b).¹⁶ When the antibiotic was applied to *Micrococcus luteus*, the minimum inhibitory concentration (MIC) can be switched reversibly from 16 $\mu\text{g}/\text{ml}$ in initial state to 2 $\mu\text{g}/\text{ml}$ after light irradiation. Also, in our group, Mafy and co-workers reported a photoswitchable inhibitor of CENP-E to control the mitotic process reversibly (Figure 2c).¹⁷ There are hundreds of works have already been reported using such strategy in cell and animal model experiments, however, challenges remain when it comes to clinical treatment.¹⁸⁻¹⁹ One major challenge is that currently no favourable photoswitches can be used in applications of photopharmacology.

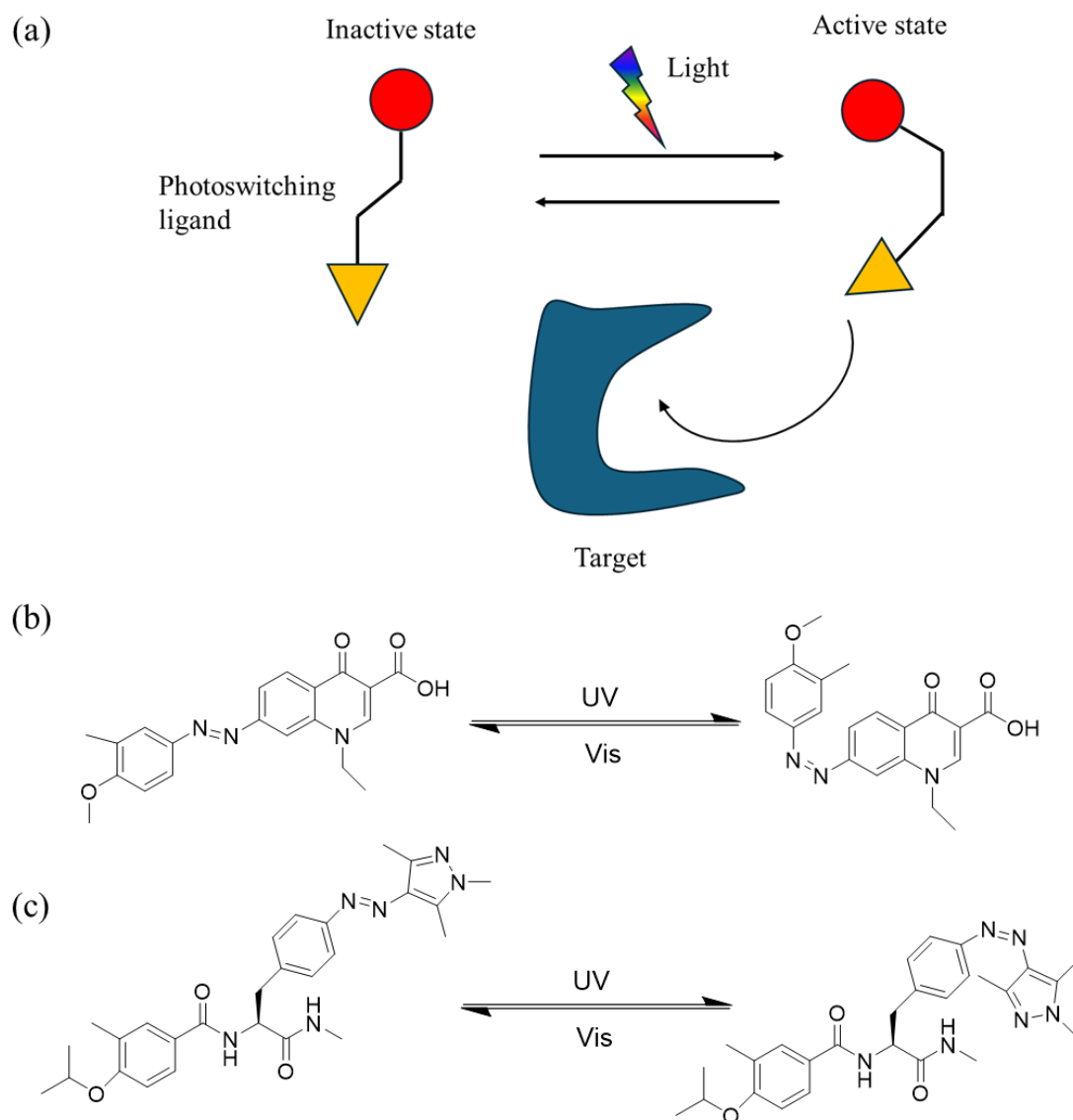


Figure 2. (a) Figure showing principle of photopharmacology. (b) Photoswitching antibiotic reported by Feringa *et al.* (c) Photoswitching CENP-E inhibitor reported by Mafy *et al.*

1.3 Photoswitches

To contribute to the development of photopharmacology, there is a growing demand in optimizing the new photoswitches with good photoswitching abilities. The performance of a photoswitch is determined based on distinct factors such as the absorption maximum wavelength (λ_{max}), quantum yield (Φ), relative abundance of *E* and *Z* isomers at the photostationary state (PSS), thermal stability of the isomers, and fatigue-resistant photoswitching cycle.²⁰ Among those reported photoswitches,

azobenzenes (Figure 3a) fulfill most of the requests mentioned above than other occasionally used photoswitches including diarylethenes, spiropyrans, stilbenes (Figure 3b, 3c and 3d).²¹⁻²⁴ Since 1930s, azobenzenes are usually considered as the most reliable photoswitching motifs.²⁵ Azo-based photoswitches absorb specific wavelengths of light and undergo reversible conversion between their *trans* (*E*) and *cis* (*Z*) isomers with large structural changes, which have been utilized for diverse applications in biology,²⁶⁻²⁹ and pharmacology.^{15, 30-32} However, azobenzene has one fatal drawback: its photoisomerization requires excitation with ultraviolet light (UV). UV irradiation, as it known to all, has short wavelength with high energy and penetrates poorly in tissue. For conventional azobenzene photoswitches, one method for tuning the spectral characteristics and thereby altering photoswitch properties is to substitute suitable functional groups on the phenyl rings.³³⁻⁴⁰ But still, the redshift in the absorption bands always accompanied by a significant decrease in the half-lives.

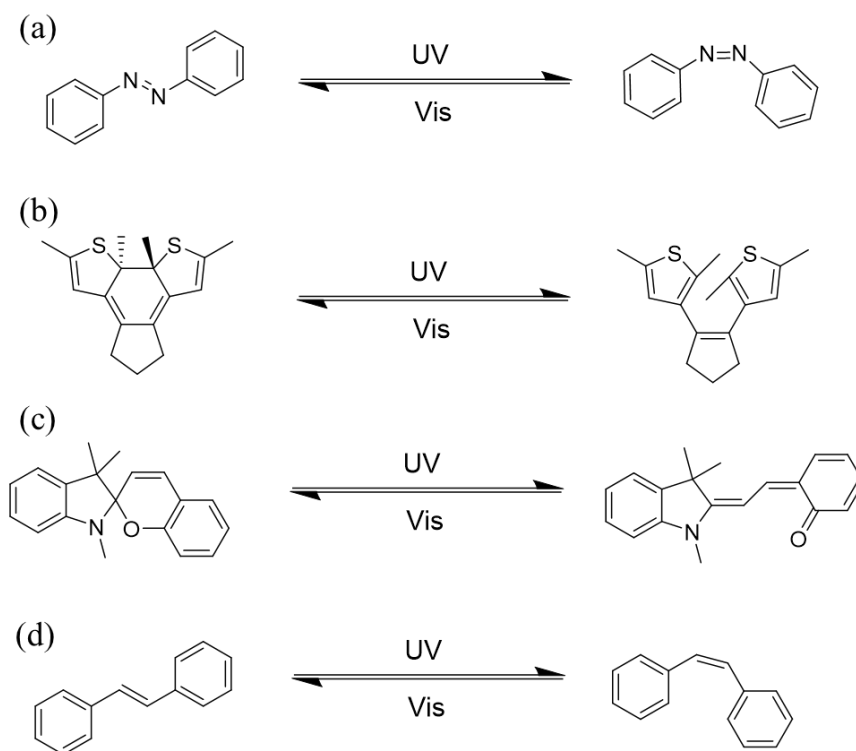


Figure 3. Figure showing often used photoswitches. (a) Azobenzene, (b) diarylethene, (c) spiropyran, (d) stilbene.

1.4 Heteroaryl azo-photoswitches

“Heteroaryl azo”-based photoswitches have recently received considerable attention owing to their photophysical characteristics originating from the heterocyclic aryl motifs.⁴¹ Photoswitches with a five-membered heteroaryl motif exhibit distinct photophysical properties, steric profiles, and molecular geometries.^{42–45} Many drug molecules possess a five-membered heteroaryl motif;^{46–49} hence, their photoswitchable analogs can be used in the field of photopharmacology, provided that the photoswitch isomerizes when exposed to visible light.^{50,51} Pyrrole, pyrazole, imidazole, isoxazole, triazole, and thiophene are considered as the five-membered heteroaryl motifs that have been used in the development of photoswitches (Figure 4a).^{52–58} Some of these photoswitches have shown exceptionally long half-lives,^{52, 56b} while arylazooxazole shows interesting switching properties in solid state.⁵⁹ However, they require ultraviolet-light irradiation for *E*→*Z* isomerization. In the case of thiophene-based photoswitches, both *E*→*Z* (365 nm) and *Z*→*E* (285 nm) isomerizations require UV irradiation.⁵⁸ Conversely, azobenzazoles can be isomerized using visible light, albeit with relatively short half-lives of the *Z* isomers (e.g., 0.4 s for benzothiazole).^{60,61} Our interest was to investigate novel thiazole-based photoswitches as a new class of “heteroaryl azo” compounds with isomerization induced by visible light and relatively long half-lives of the *Z* isomers. Previously, a visible-light switchable p38 α kinase inhibitor comprising 4,5-disubstituted phenylazothiazole (**PAT**) was reported; however, the azo moiety was reduced to hydrazine in the presence of dithiothreitol (DTT).⁶² Recently in our laboratory, they reported a visible-light switchable Rho kinase inhibitor based on a pyridine-appended **PAT** that was stable in the presence of DTT and glutathione (Figure 4b).⁶³ Motivated by this finding, in the present study, I focused on the fundamental properties and substituent effects of **PAT** compounds, aiming to

establish a new category of visible-light photoswitches. I envisioned that the electron-donating sulfur heteroatom of thiazole should have a favorable effect to reduce the energy gap of $\pi \rightarrow \pi^*$ transitions, enabling isomerization via visible-light absorption. I indeed found that **PAT** photoswitches generally isomerize reversibly under visible-light irradiation, resulting in an excellent composition of *E* and *Z* isomers at the PSS and reasonably long thermal half-lives of the *Z* isomers. Interestingly, electron-donating or withdrawing substituents at the *ortho* or *para* positions on the phenyl ring of the photoswitch compound resulted in a further shift of the λ_{max} to longer wavelengths with a smaller thermal stability compensation effect for some **PAT** derivatives. I also demonstrated the unusual T-shaped geometry of the *Z* isomer of **PAT** using X-ray crystal analysis. In addition, **PAT** photoswitches without strong electron-withdrawing substituents showed excellent stability against DTT and glutathione reductants.

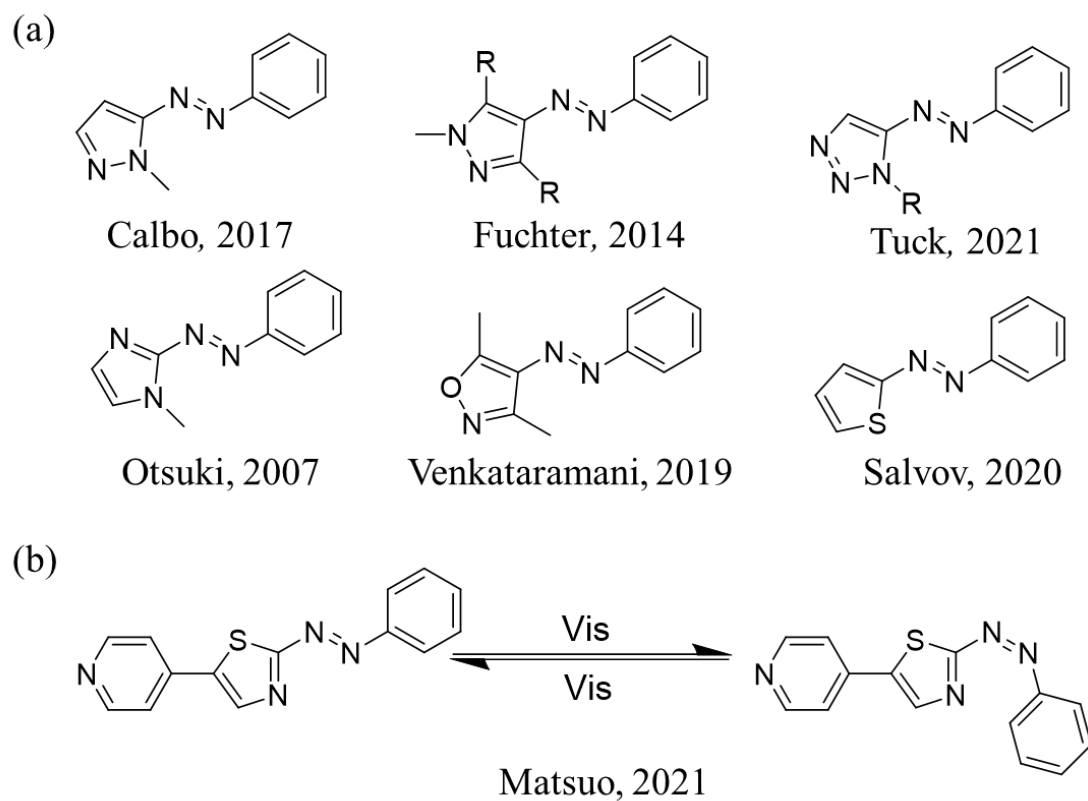


Figure 4. (a) Hetero azo-photoswitches containing five-membered rings reported previously. (b) Photoswitching Rho kinase inhibitor reported by Tamaoki's group.

2. Results and discussion

2.1 Synthesis of Phenylazothiazoles

I synthesized compounds **1–5** and **9** from the corresponding phenyl hydrazine hydrochlorides via thiazoline cyclization followed by oxidation (Figure 1a, Scheme 1-5).⁶⁴ The yield (<10%) of the oxidation reaction of 4,5-dihydrothiazole to azothiazole was enhanced (>30%) using silver dioxide as the oxidizing agent instead of air. For **6–8**, a nitro-appended PAT derivative was selectively reduced to an amine using zinc, which was then methylated using methyl iodide (Figure 5a). Compounds **10** and **11** were synthesized from aminothiazole via a direct azo coupling reaction (Figure 5a, Scheme 1-5). The compounds were unambiguously characterized using a variety of analytical methods (¹H NMR, ¹³C NMR, and mass spectroscopy; Figures 6–38). The synthesis of **1** was reported previously without any study on its photophysical properties.⁶⁵

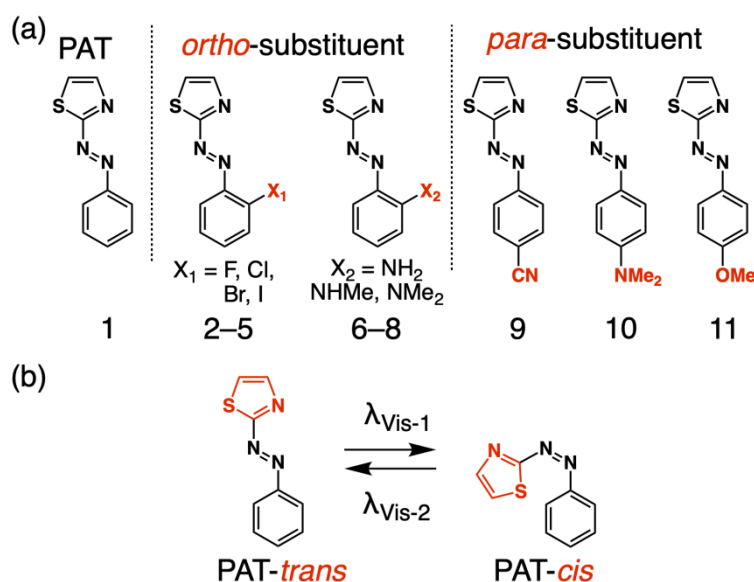
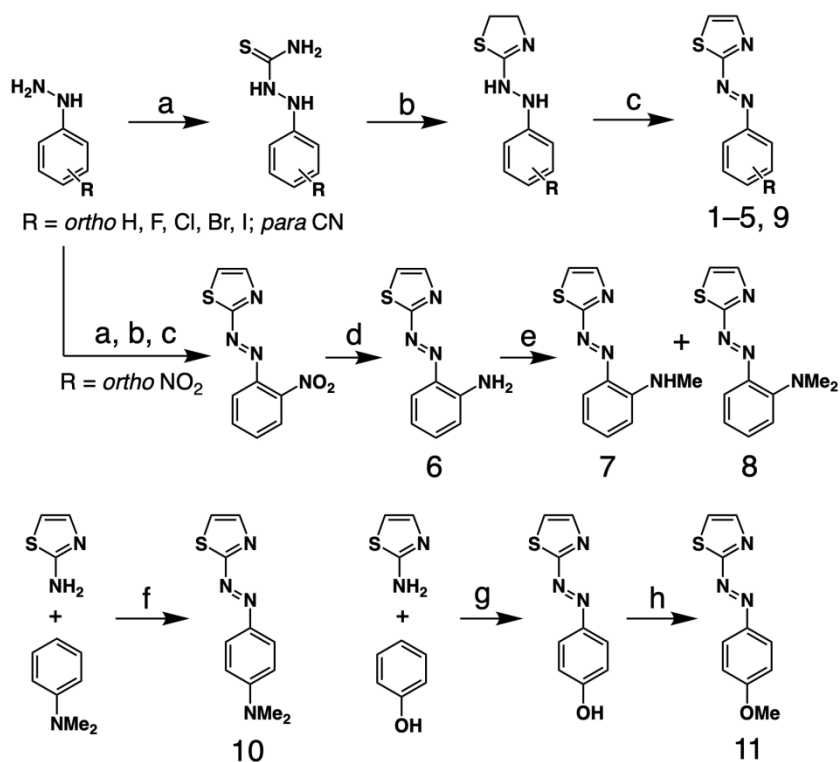


Figure 5. (a) Molecular structures of un [**1**], *ortho*- (F [**2**], Cl [**3**], Br [**4**], I [**5**], NH₂ [**6**], NHMe [**7**], NMe₂ [**8**]) and *para*- (CN [**9**], NMe₂ [**10**], OMe [**11**]) substituted PAT. (b) Scheme showing the reversible isomerization of **1** using visible-light irradiation having different wavelengths.



Scheme 1. Reagents and conditions. (a) NH_4SCN , $\text{EtOH}/\text{H}_2\text{O}$ (9:1 v/v), 25°C ; (b) $\text{BrCH}_2\text{CH}_2\text{NH}_2\cdot\text{HBr}$, iPrOH , 110°C , then NaHCO_3 ; (c) Na_2CO_3 [or Ag_2O], EtOH , 110°C ; (d) Zn , NH_4Cl , MeOH , 25°C ; (e) MeI , DMF , 30°C (f) Concentrated H_2SO_4 , NaNO_2 , 0°C (g) Concentrated HCl , aqueous NaNO_2 , 0°C ; (h) K_2CO_3 , DMF , then dimethyl sulfate, 25°C .

2.1.1 NMR spectra (^1H , ^{13}C) and Mass spectra of PAT 1-11.

^1H NMR spectra of PAT 1-11.

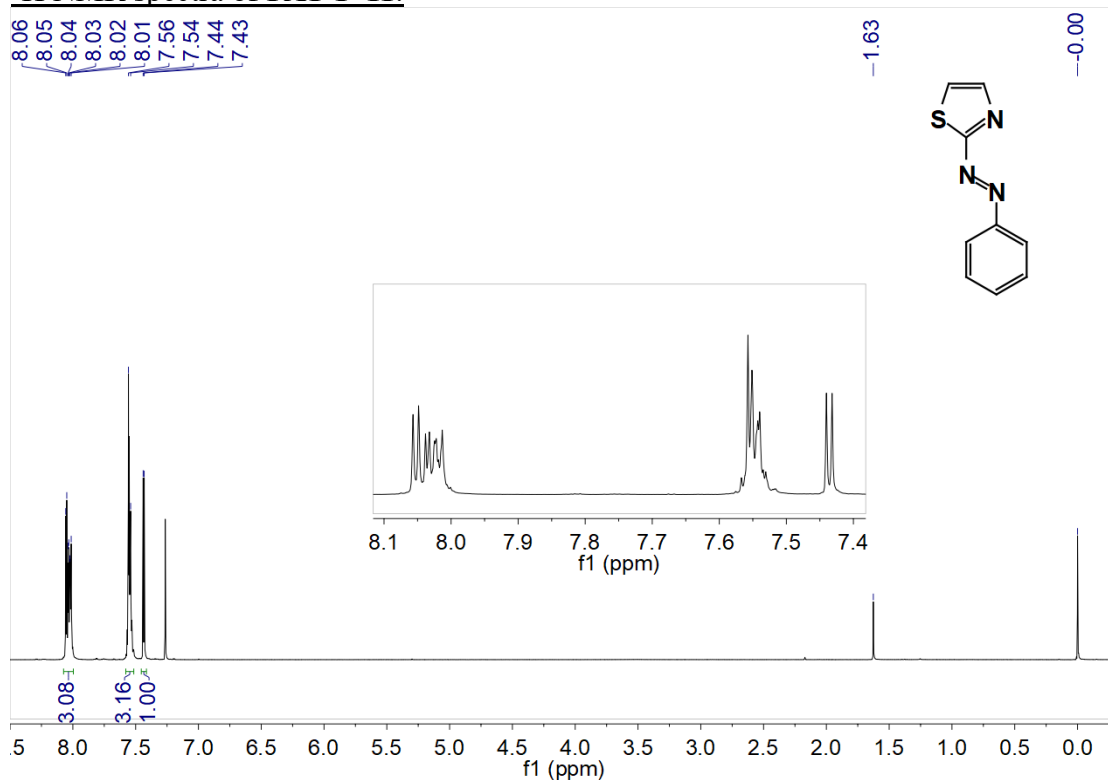


Figure 6: ^1H NMR of PAT 1 in CDCl_3 . ^1H NMR (400 MHz, CDCl_3) δ 8.06 (d, $J = 3.2$ Hz, 1H), 8.04 – 8.01 (m, 2H), 7.56 – 7.51 (m, 3H), 7.44 (d, $J = 3.2$ Hz, 1H).

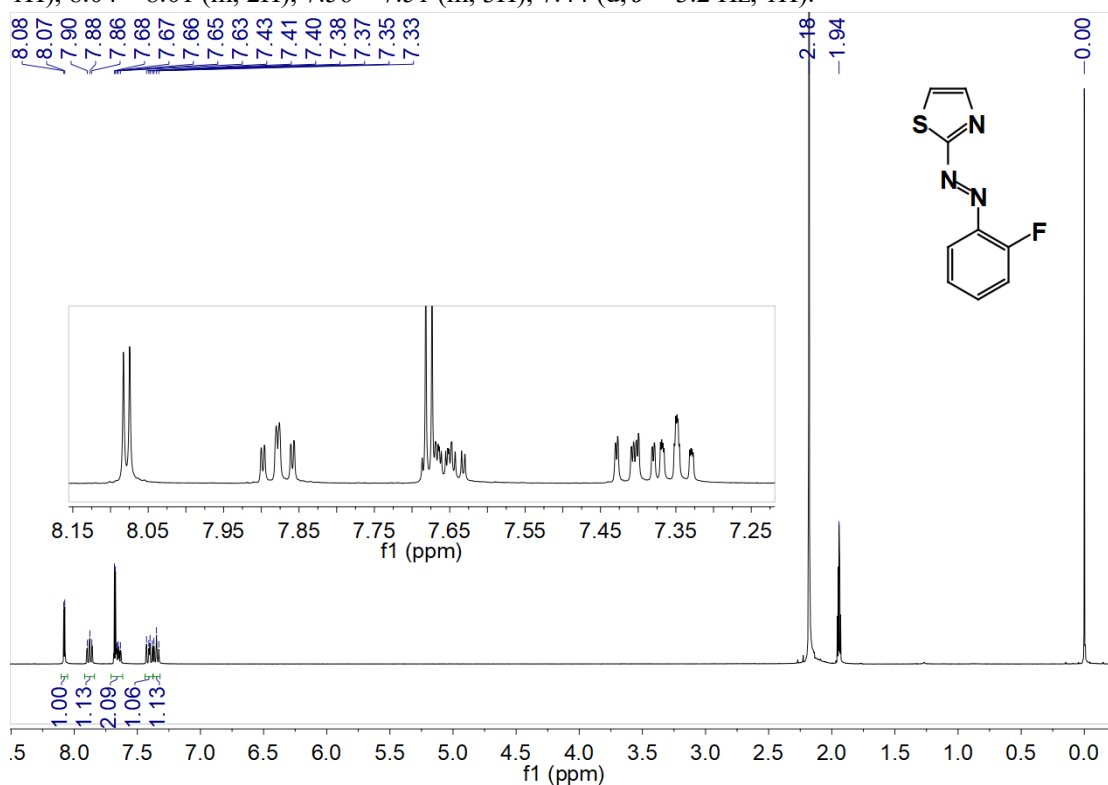
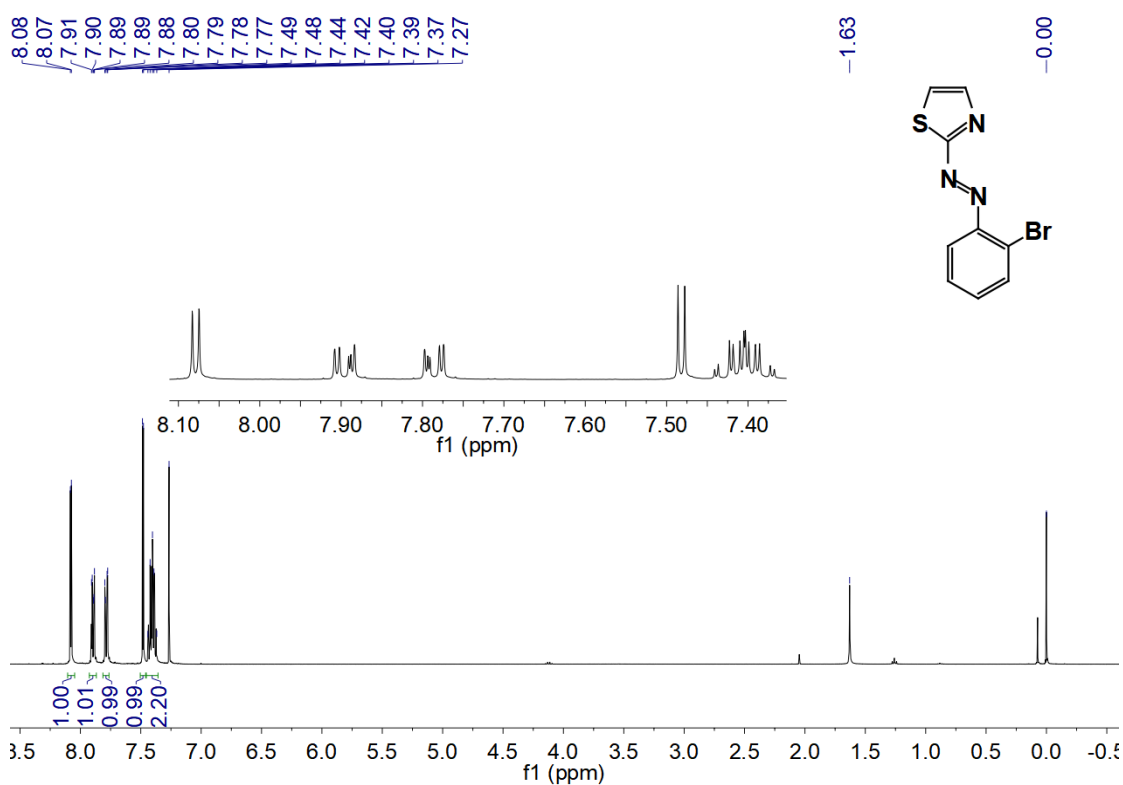
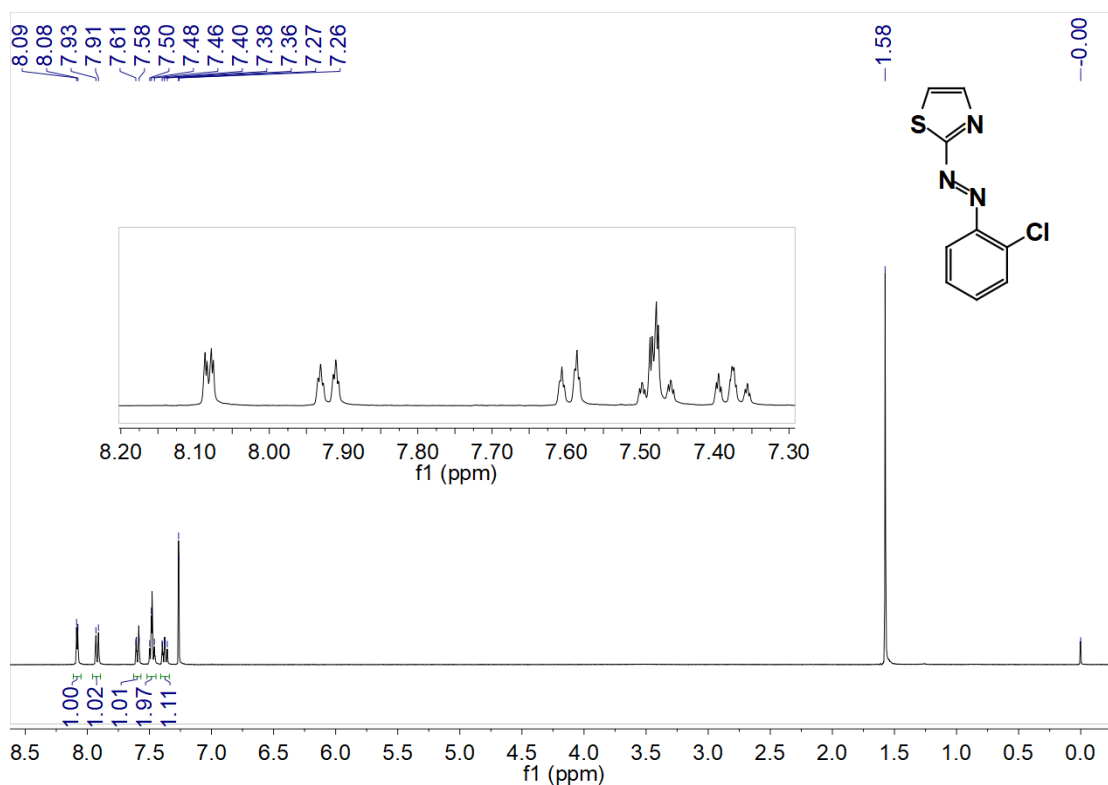
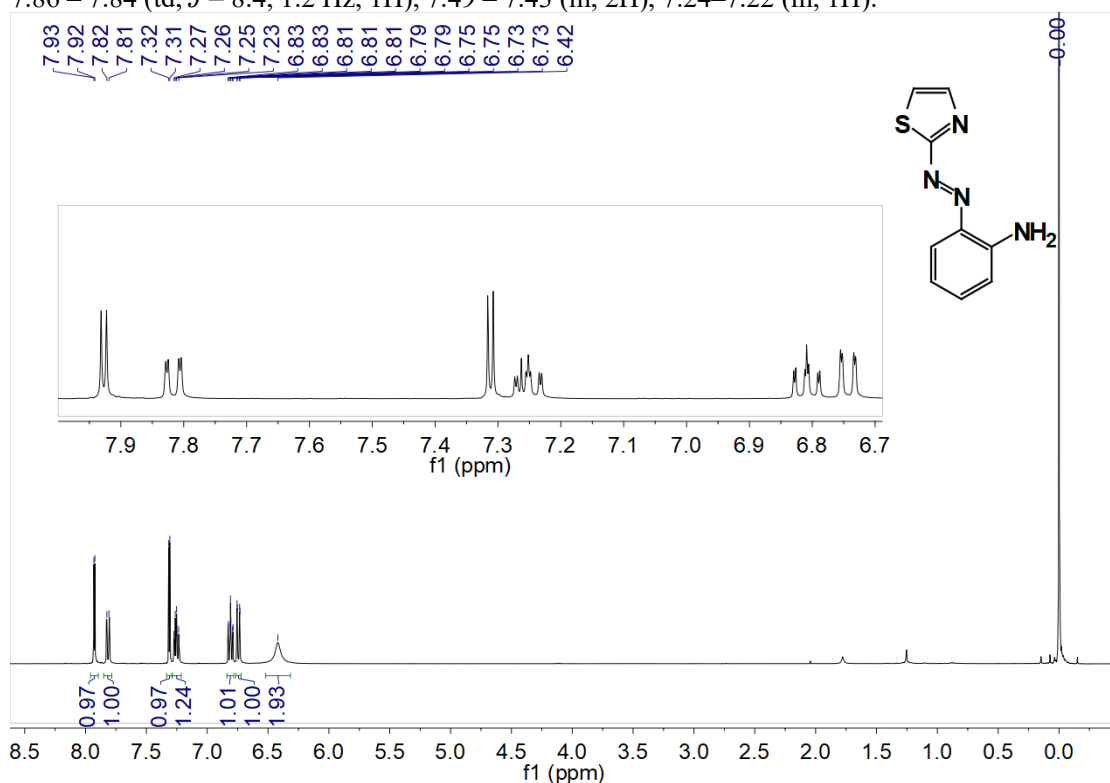
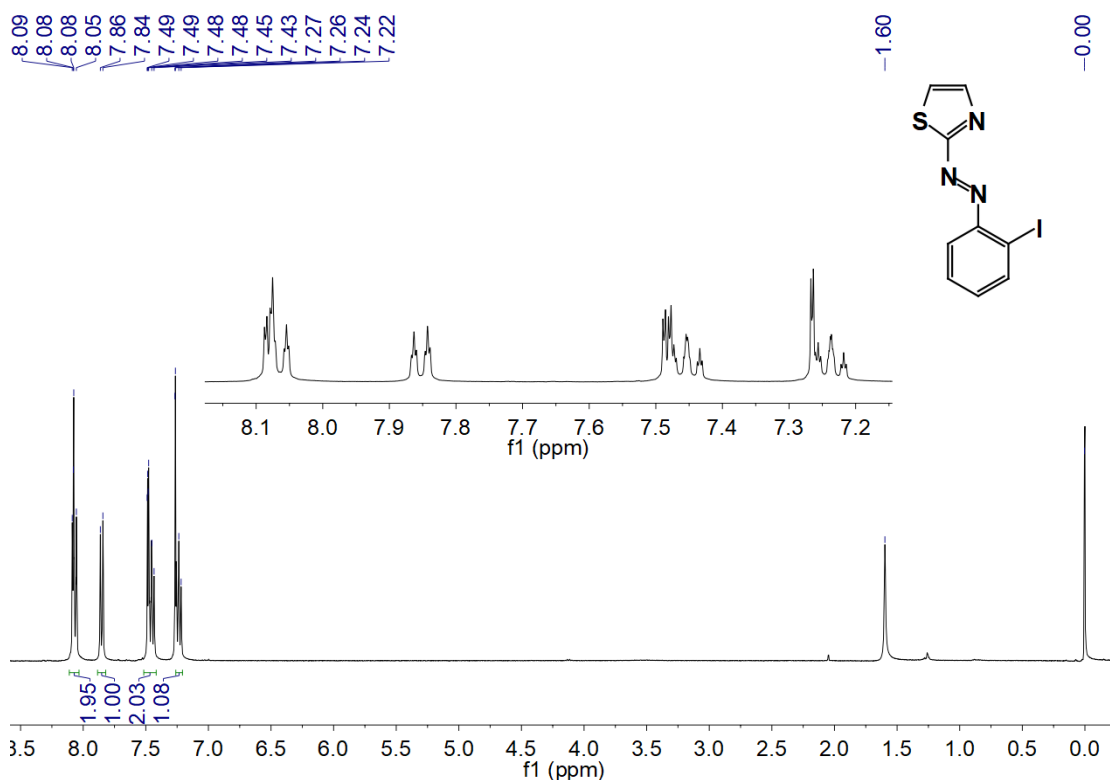
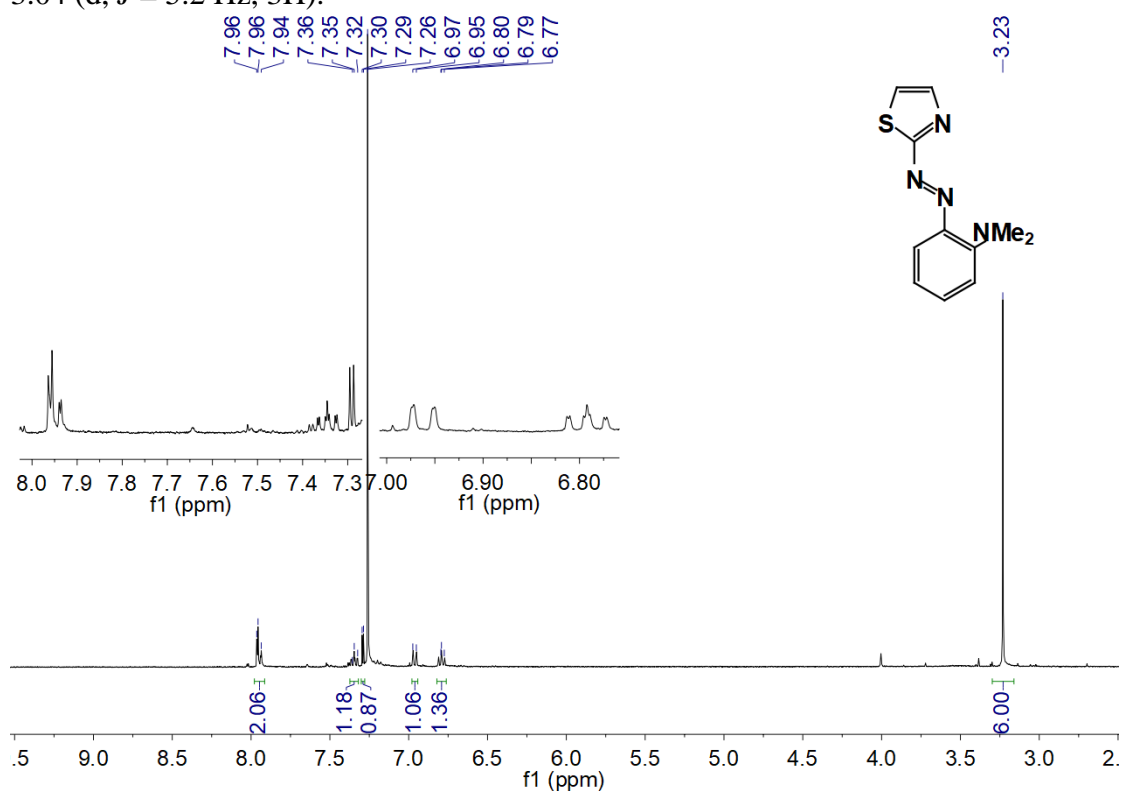
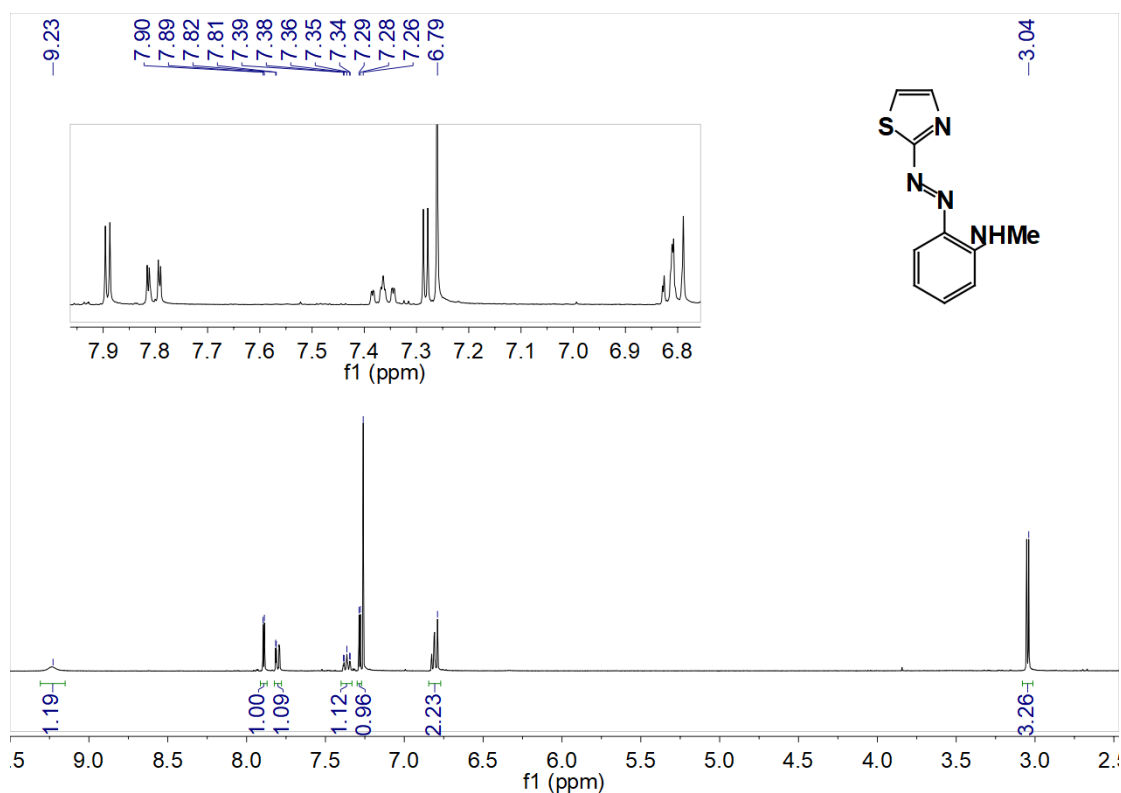


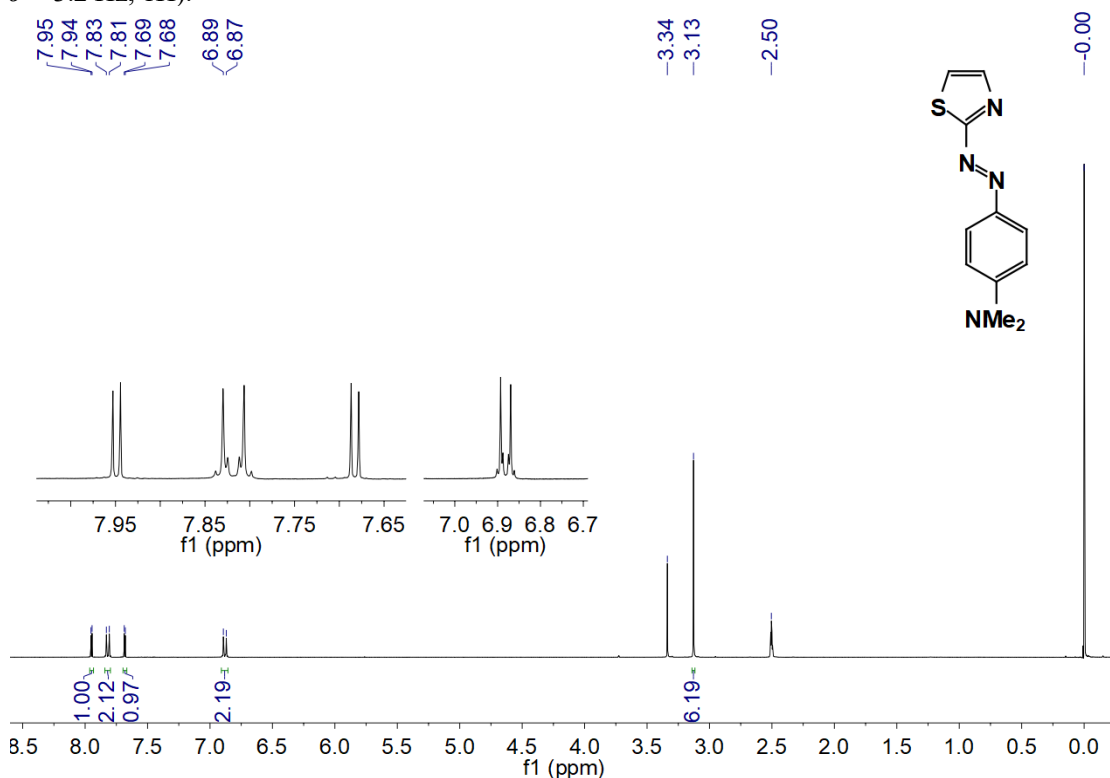
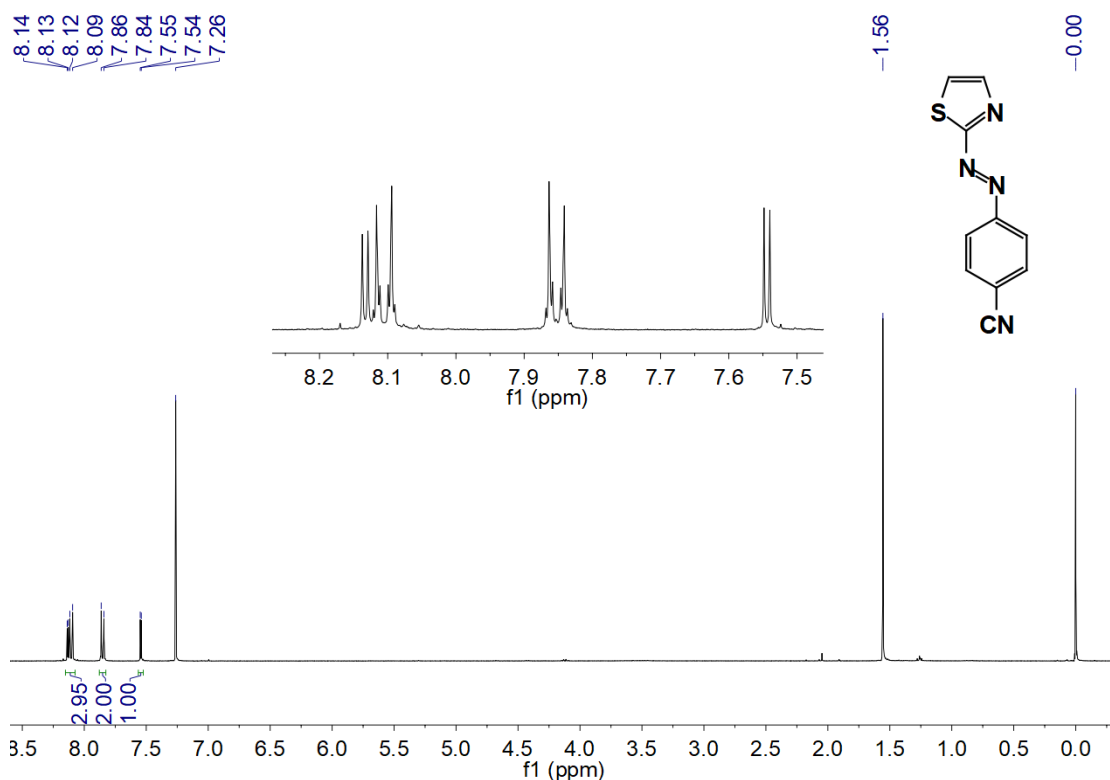
Figure 7: ^1H NMR of PAT 2 in CD_3CN . ^1H NMR (400 MHz, CD_3CN) δ 8.08 (d, $J = 3.2$ Hz, 1H), 7.90 – 7.85 (td, $J = 1.6, 8.0, 7.6$ Hz, 1H), 7.68 (d, $J = 3.2$ Hz, 1H), 7.67 – 7.63 (m, 1H), 7.43–

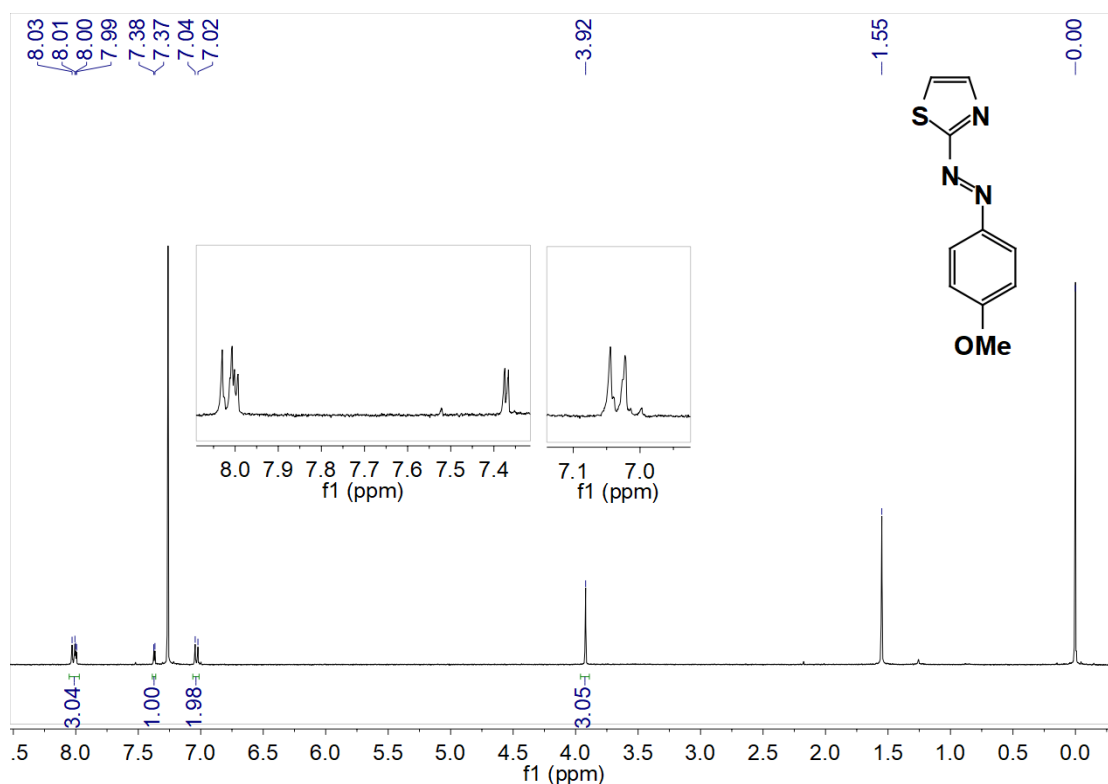
7.37 (ddd, $J = 0.8, 8.4$ Hz, 1H), 7.37–7.33 (tdd, $J = 0.4, 1.2, 7.2$ Hz, 1H).



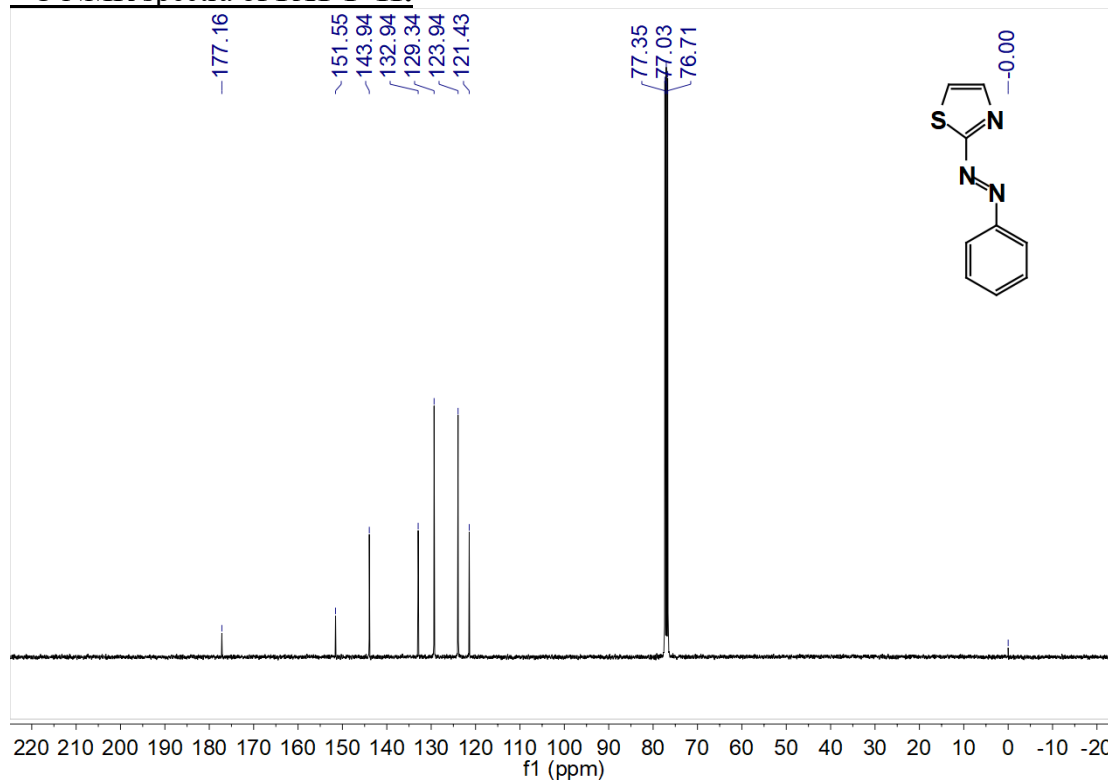








^{13}C NMR spectra of PAT 1–11.



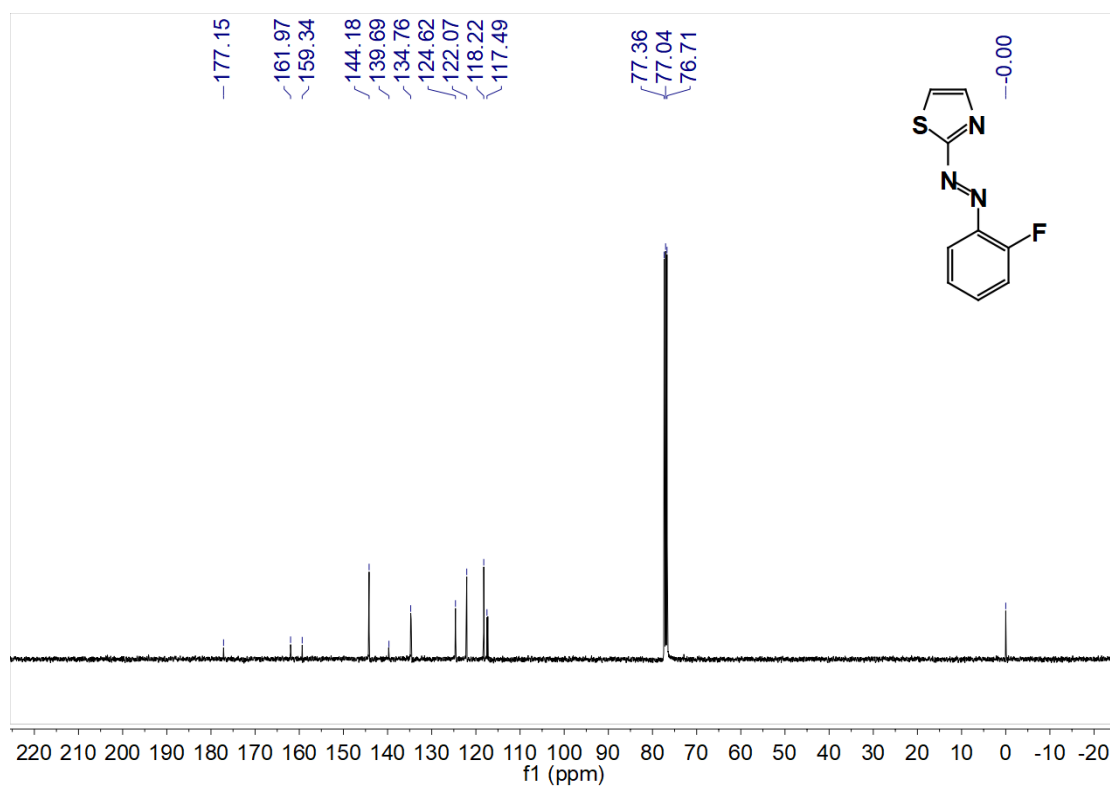


Figure 18: ¹³C NMR of PAT 2 in CDCl₃. ¹³C NMR (400 MHz, CDCl₃) δ 177.15, 161.97, 159.34, 144.18, 139.69, 134.76, 124.62, 122.07, 118.22, 117.49.

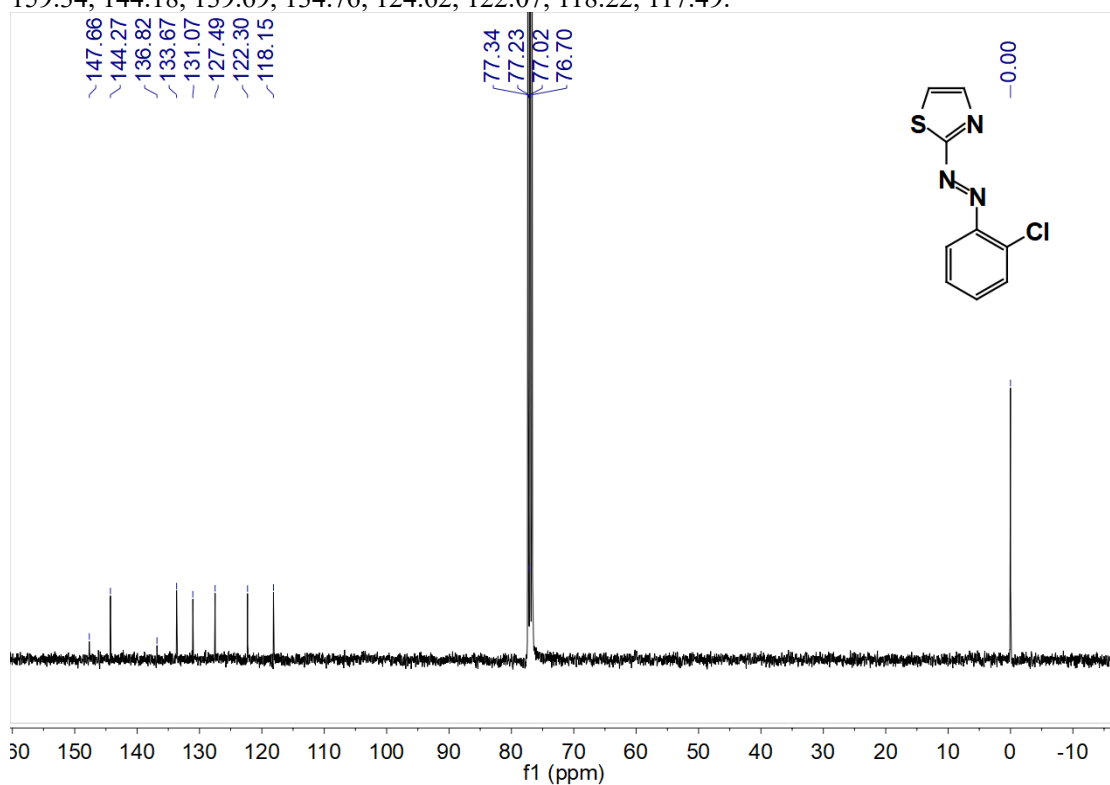
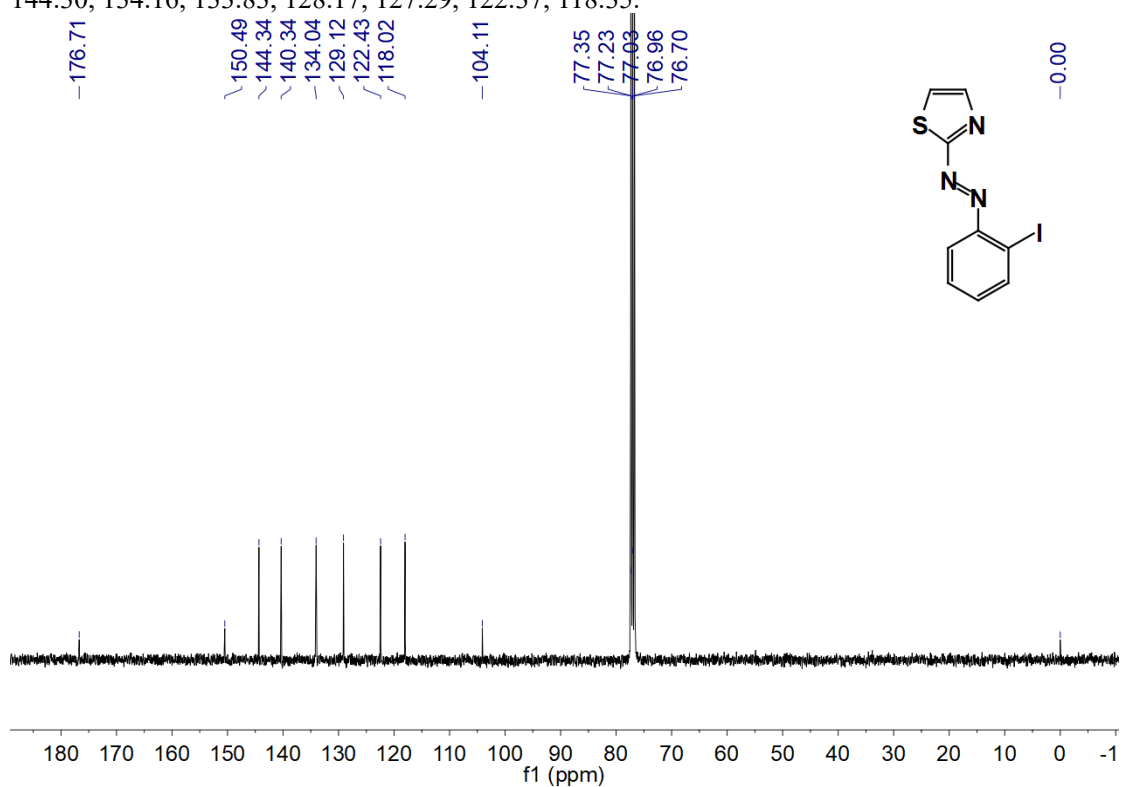
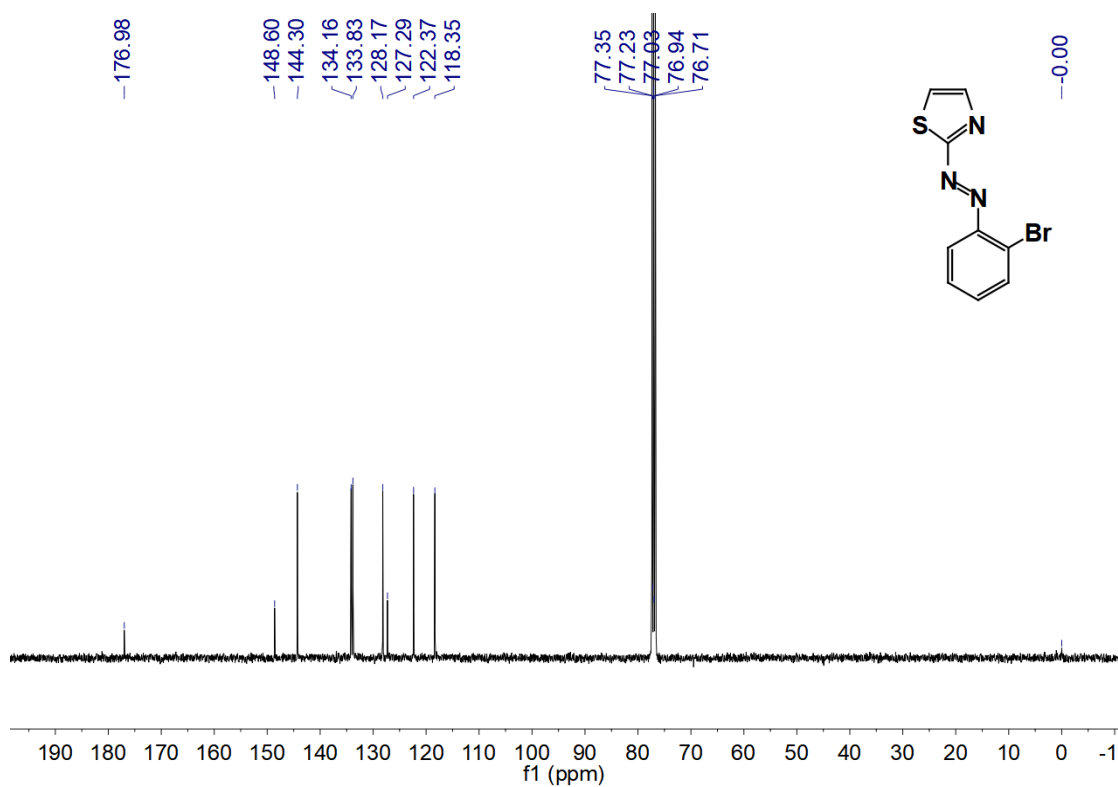
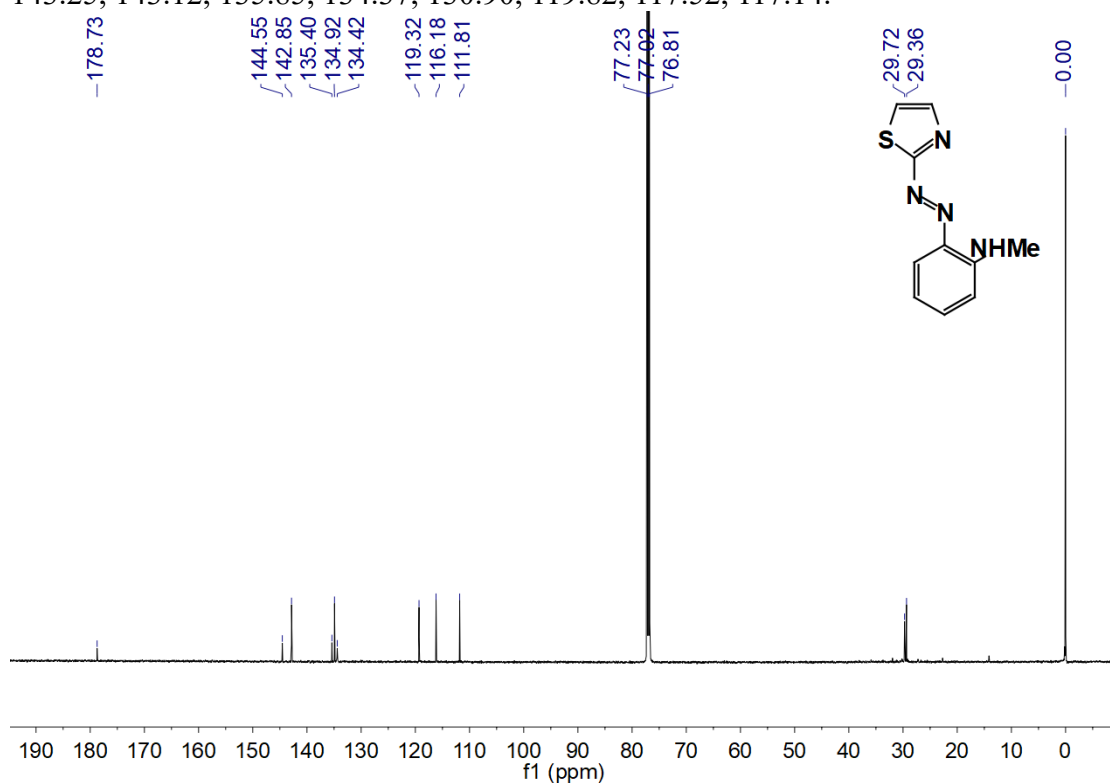
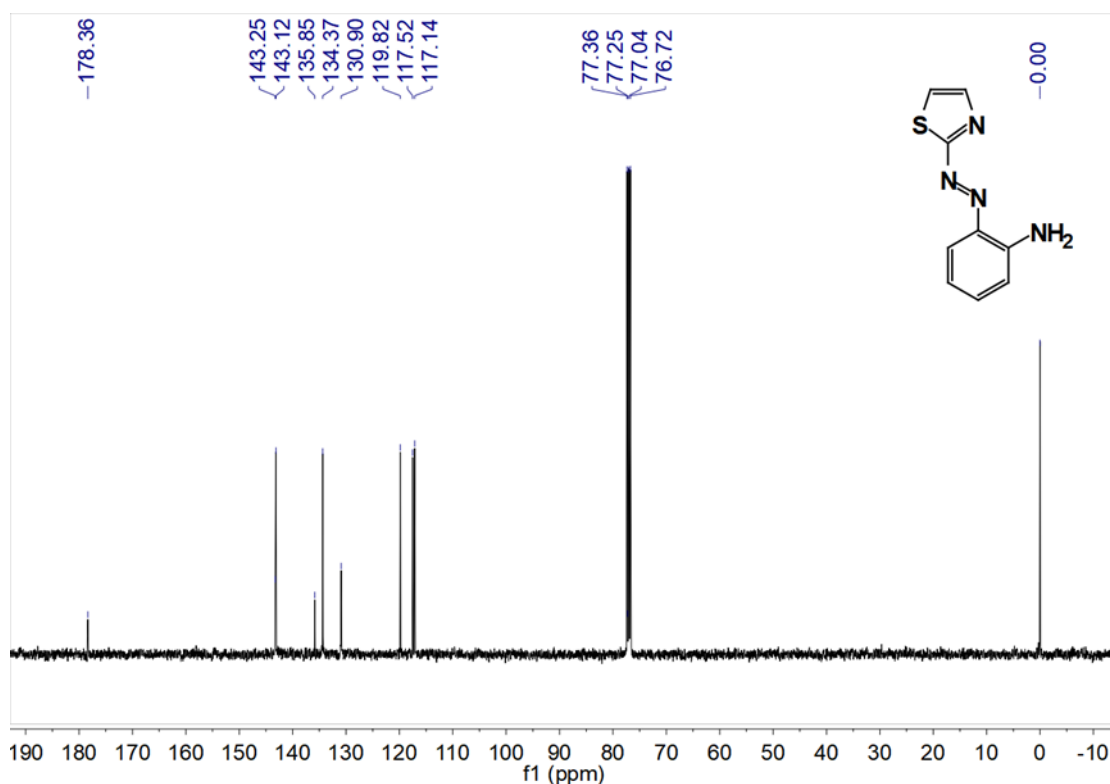


Figure 19: ¹³C NMR of PAT 3 in CDCl₃. ¹³C NMR (400 MHz, CDCl₃) δ 147.66, 144.27, 136.82, 133.67, 131.07, 127.49, 122.30, 118.15.





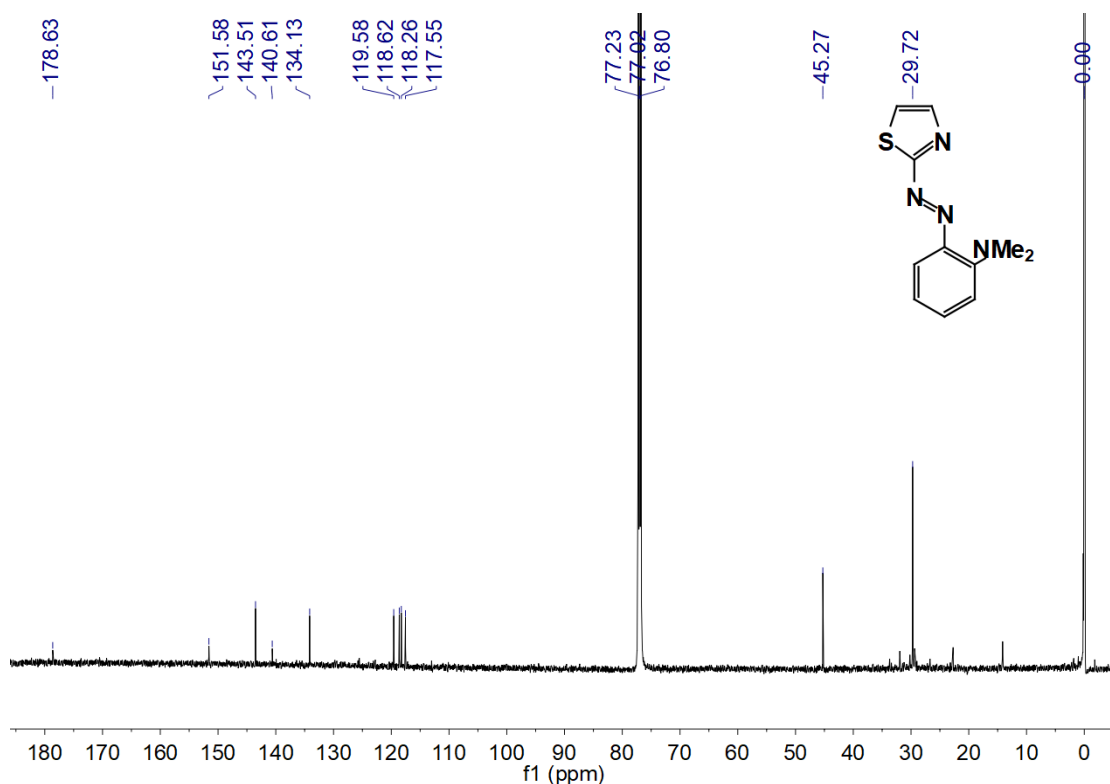


Figure 24: ¹³C NMR of PAT 8 in CDCl₃. Peak at δ 29.72 was not assigned. ¹³C NMR (600 MHz, CDCl₃) δ 178.63, 151.58, 143.51, 140.61, 134.13, 119.58, 118.62, 118.26, 117.55, 45.27.

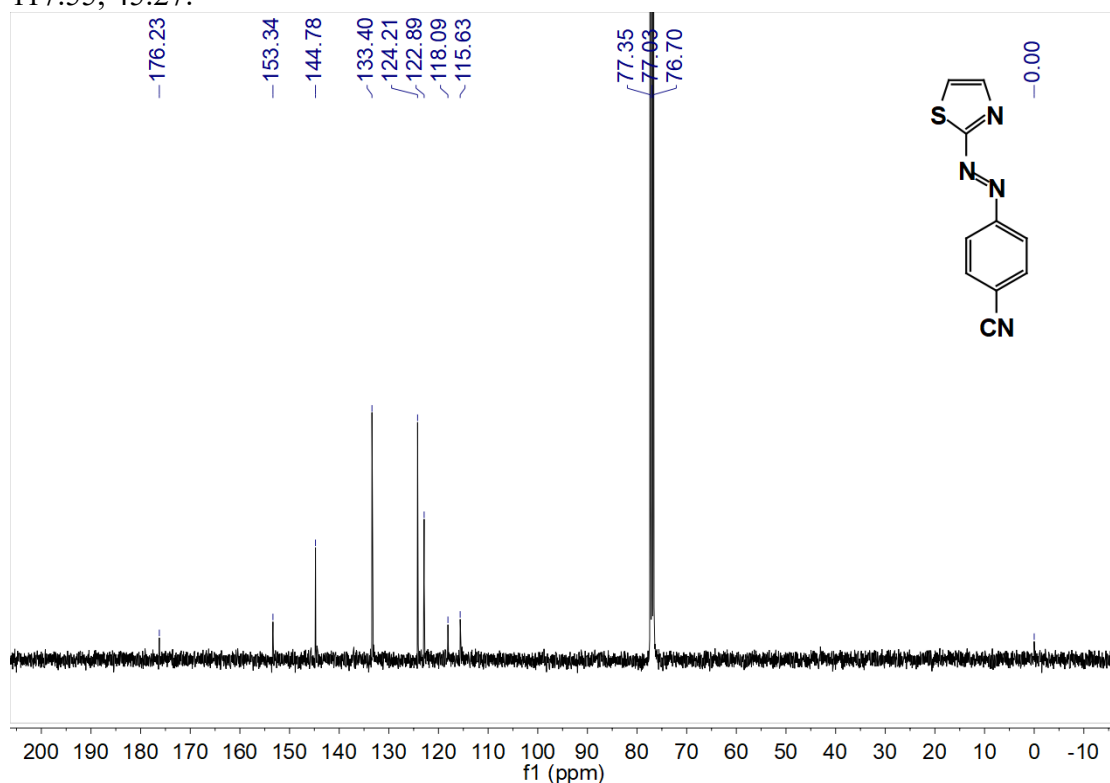


Figure 25: ¹³C NMR of PAT 9 in CDCl₃. ¹³C NMR (400 MHz, CDCl₃) δ 176.23, 153.34, 144.78, 133.40, 124.21, 122.89, 118.09, 115.63.

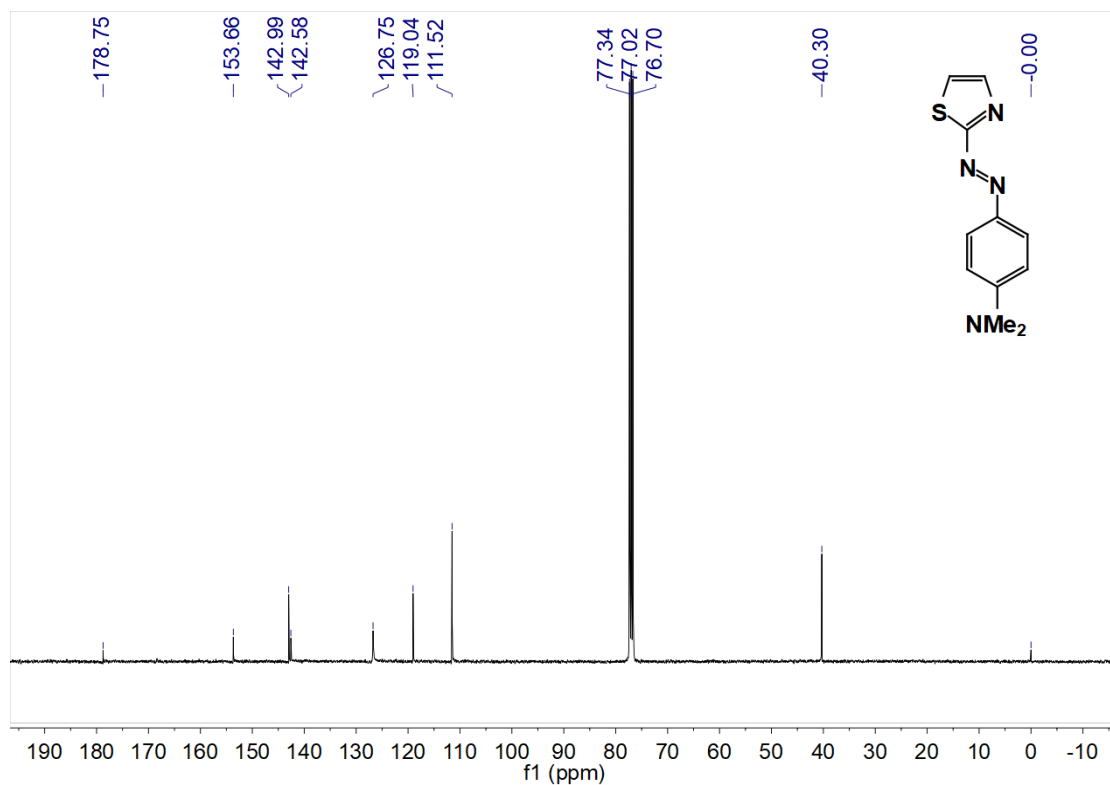


Figure 26: ¹³C NMR of PAT 10 in DMSO-*d*₆. ¹³C NMR (400 MHz, CDCl₃) δ 178.75, 153.66, 142.99, 142.58, 126.75, 119.04, 111.52, 40.30.

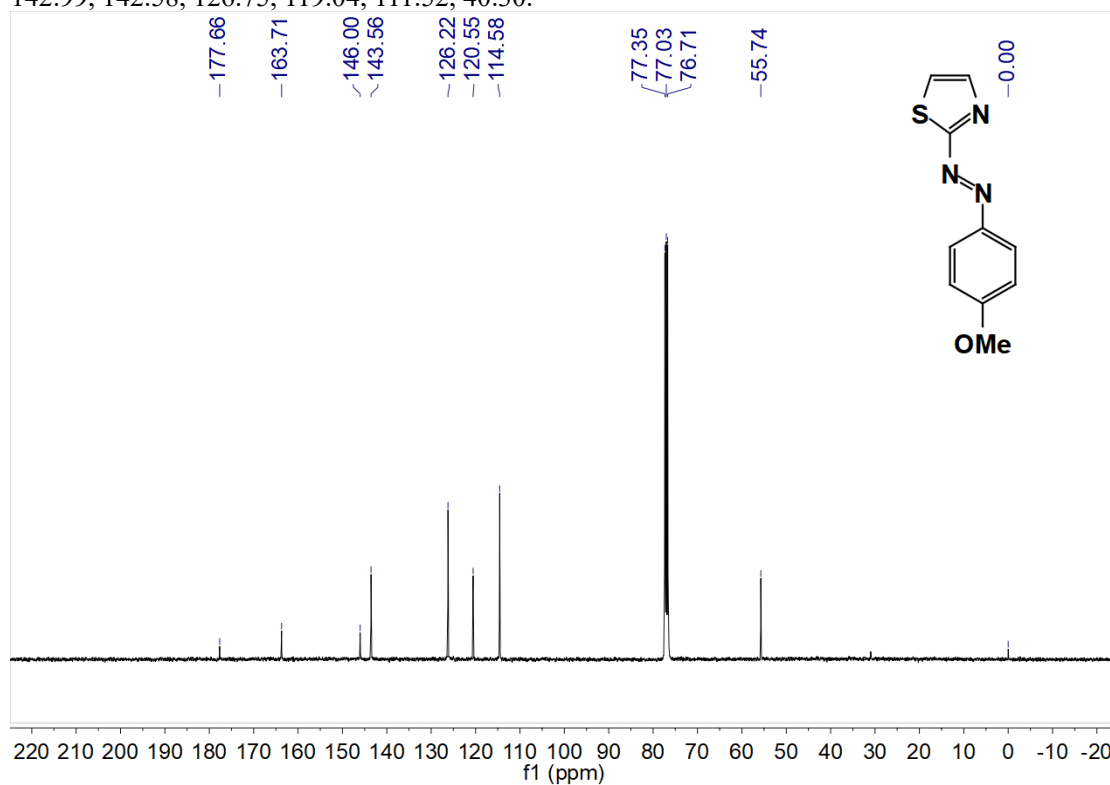


Figure 27: ¹³C NMR of PAT 11 in CDCl₃. ¹³C NMR (400 MHz, CDCl₃) δ 177.66, 163.71, 146.00, 143.56, 126.22, 120.55, 114.58, 55.74.

Mass spectra of **PAT 1-11**.

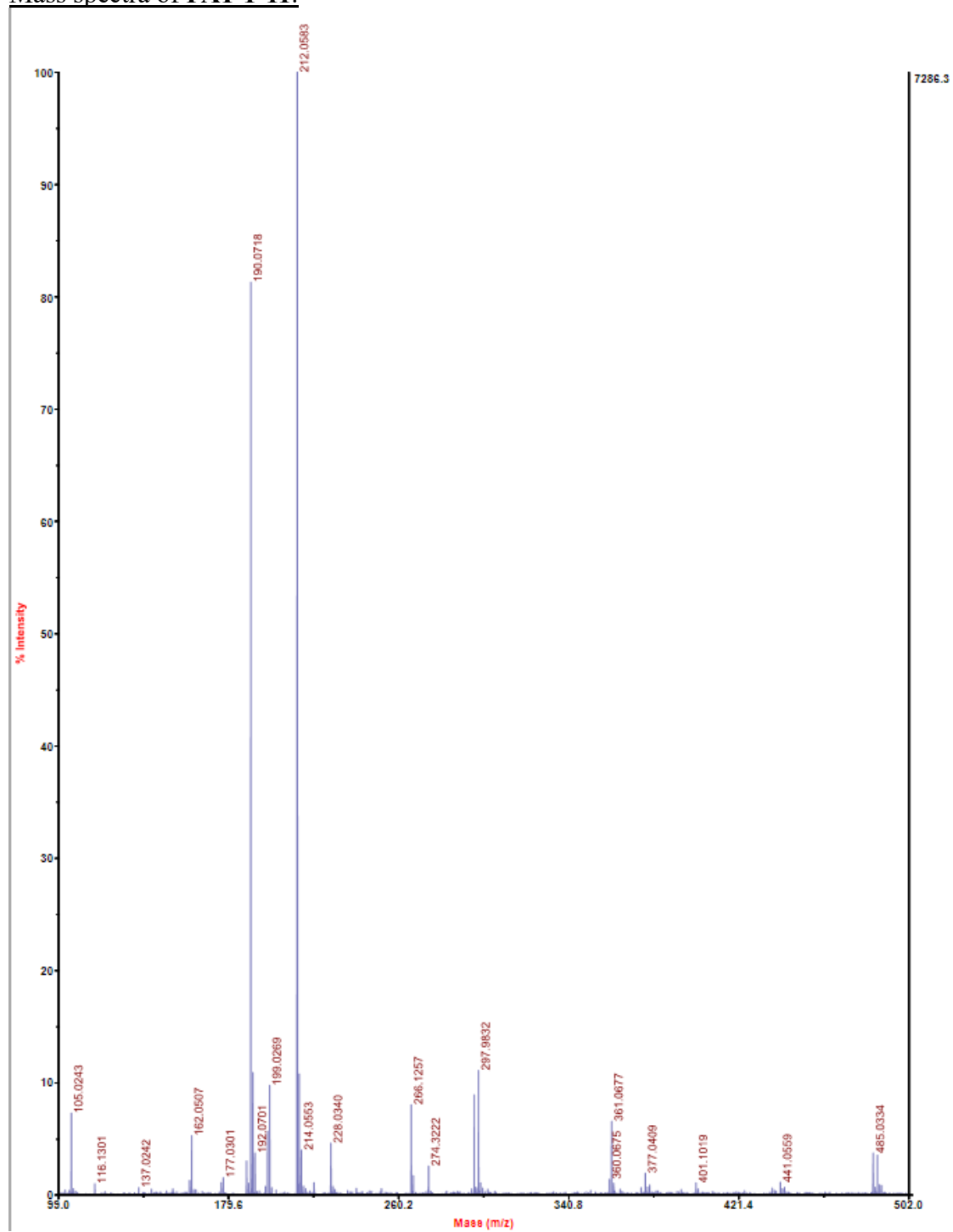


Figure 28: High-resolution mass spectra (MALDI-TOF) of **PAT 1**. m/z $[M+Na]^+$ calcd for $C_9H_7N_3S$: 212.03, found: 212.05.

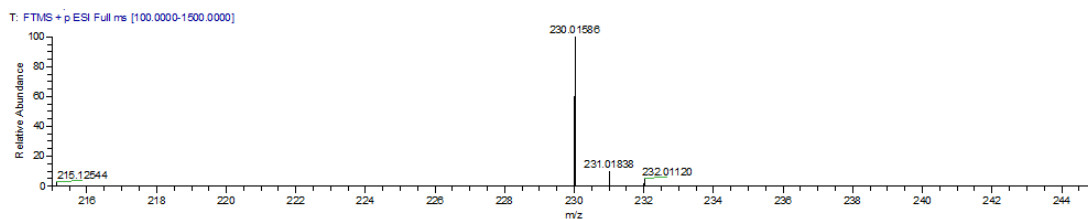


Figure 29: High-resolution mass spectra (ESI) of **PAT 2**. m/z $[M+Na]^+$ calcd for $C_9H_6FN_3S$: 230.02, found: 230.02.

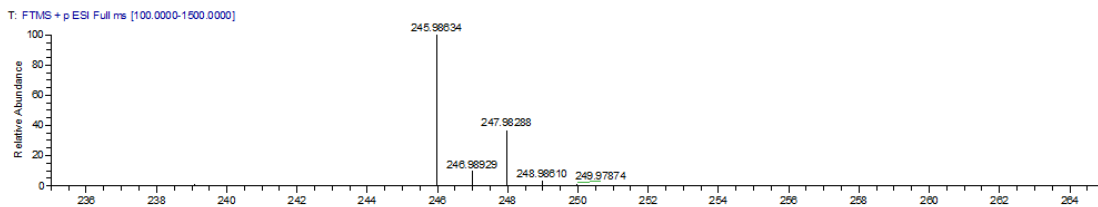


Figure 30: High-resolution mass spectra (ESI) of **PAT 3**. m/z $[M+Na]^+$ calcd for $C_9H_6ClN_3S$: 245.99, found: 245.99.

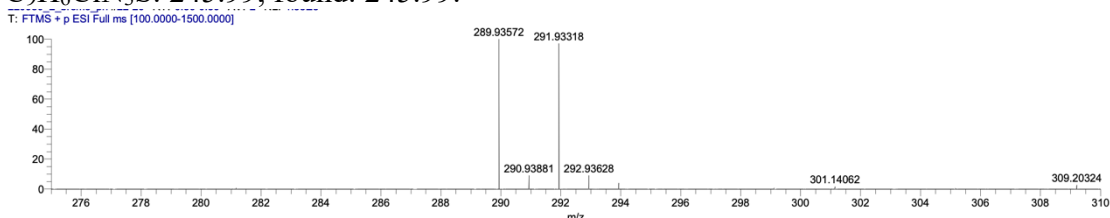


Figure 31: High-resolution mass spectra (ESI) of **PAT 4**. m/z $[M+Na]^+$ calcd for $C_9H_6BrN_3S$: 289.94, found: 289.93 and 291.93.

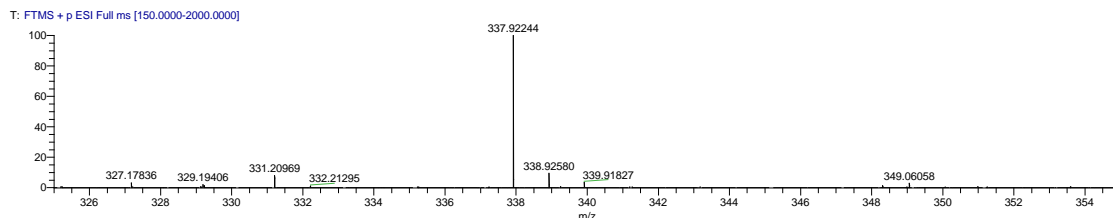


Figure 32: High-resolution mass spectra (ESI) of **PAT 5**. m/z $[M+Na]^+$ calcd for $C_9H_6IN_3S$: 337.92, found: 337.92.

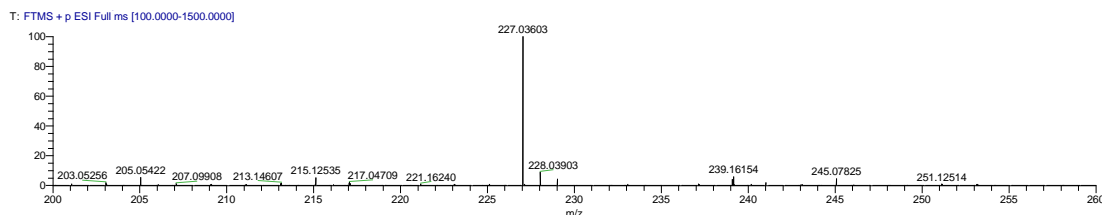


Figure 33: High-resolution mass spectra (ESI) of **PAT 6**. m/z $[M+Na]^+$ calcd for $C_9H_8N_4S$: 227.04, found: 227.04.

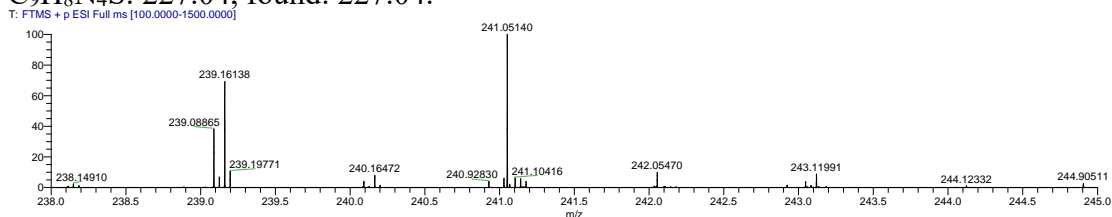


Figure 34: High-resolution mass spectra (ESI) of **PAT 7**. m/z $[M+Na]^+$ calcd for

C₁₀H₁₀N₄S: 241.05, found: 241.05.

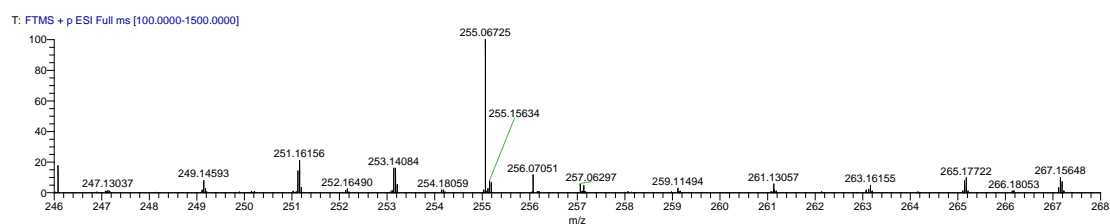


Figure 35: High-resolution mass spectra (ESI) of **PAT 8**. m/z [M+Na]⁺ calcd for C₁₁H₁₂N₄S: 255.07, found: 225.07.

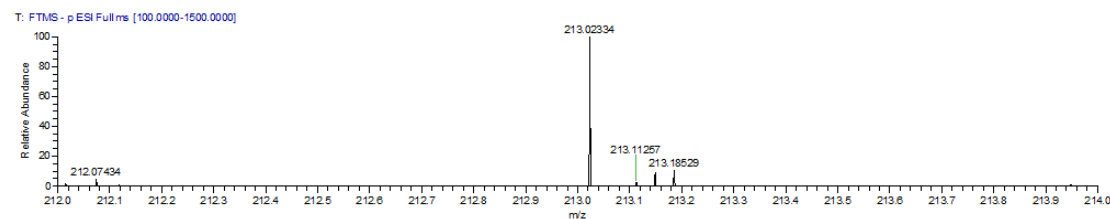


Figure 36: High-resolution mass spectra (ESI) of **PAT 9**. MS (ESI) m/z [M-H]⁺ calcd for C₁₀H₆N₄S: 213.03, found: 213.02.

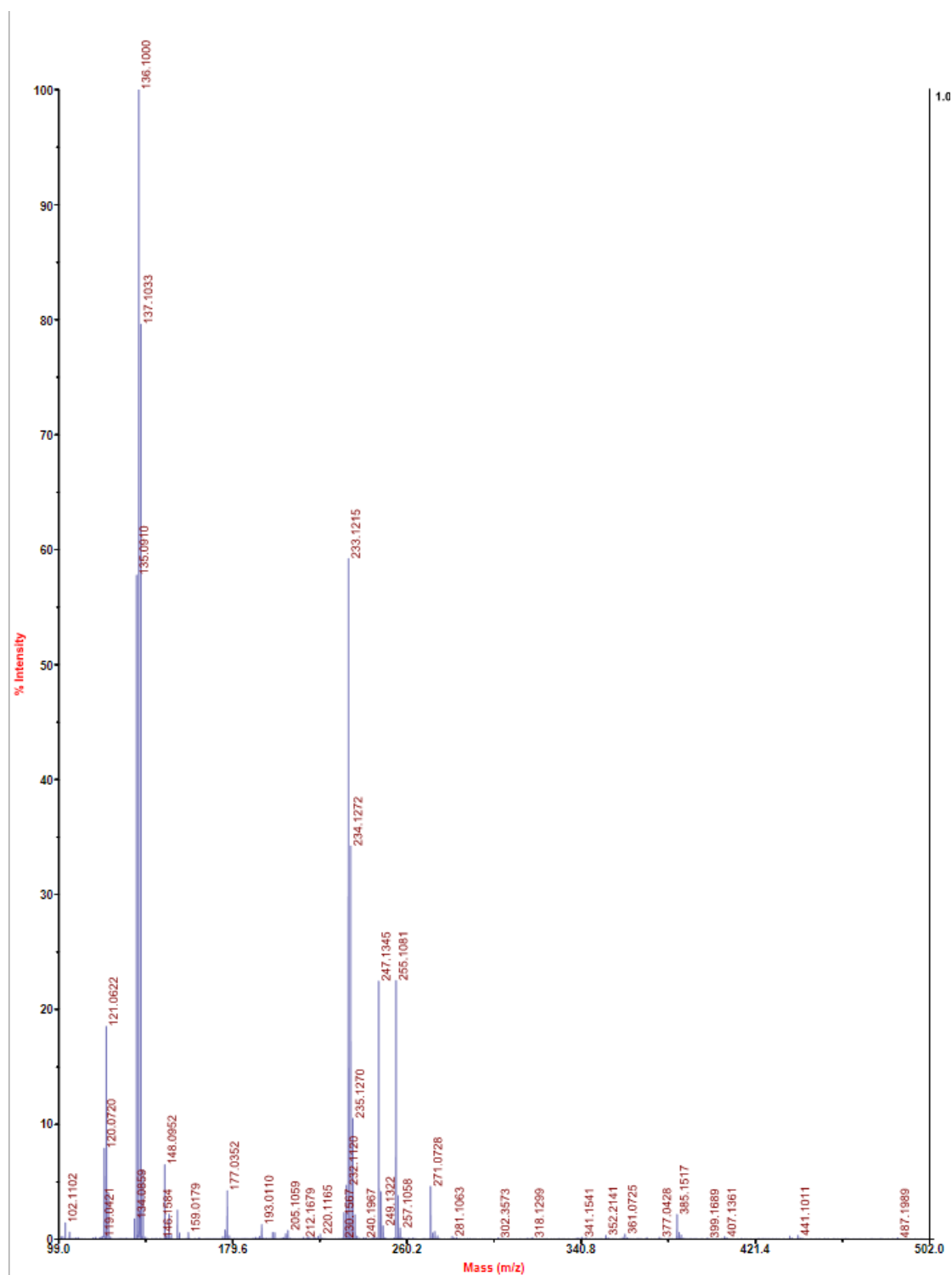


Figure 37: High-resolution mass spectra (MALDI-TOF) of **PAT 10**. m/z $[M+H]^+$ calcd for $C_{11}H_{12}N_4S$: 233.09, found: 233.12.

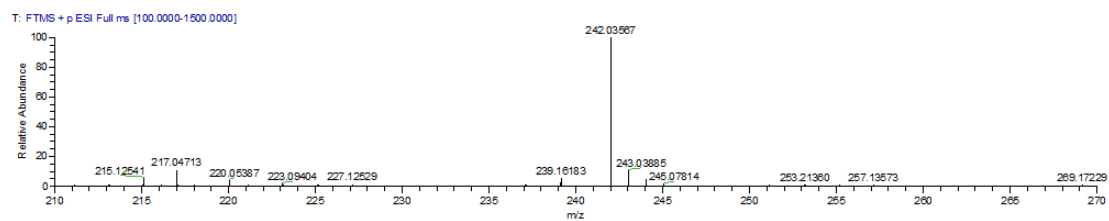


Figure 38: High-resolution mass spectra (ESI) of **PAT 11**. m/z $[M+Na]^+$ calcd for $C_{10}H_9N_3OS$: 242.04, found: 242.04.

2.2 Photoisomerization and photophysical properties of Phenylazothiazoles

I studied the photoswitching ability of **PAT** derivatives using absorption spectroscopy in acetonitrile solution at 25°C (Figures 35 and 45-51). As synthesized **1** exhibited two absorption bands ($\lambda_{\text{max}} = 364$ and 459 nm) assignable to the $\pi \rightarrow \pi^*$ and $n \rightarrow \pi^*$ electronic transitions, respectively. The λ_{max} value ($\pi \rightarrow \pi^*$) of the *E* isomer of **1** was redshifted by ~47 nm compared with the *E* isomer of azobenzene (Figure 40). Owing to the redshifted spectral features of **1**, I could induce photoisomerization using visible-light irradiation. Under 405 nm light irradiation, the absorption band intensities were considerably altered to reach the PSS (405_{PSS}) with 83% *Z* isomers (determined using ¹H NMR; Figure 41 and Table 1). The *E*→*Z* isomerization also occurred under 430 nm light irradiation, although with a reduced *Z* isomer composition (~52%) at the PSS (Figure 49). Under 525 nm light irradiation (525_{PSS}), an opposite trend was observed for the change in the absorption bands, resulting in an *E* isomer composition of 81% (Figure 39a). I then studied the effect of substituents at the *ortho* or *para* positions on the phenyl component of **PAT**. Electron-withdrawing F, Cl, Br, I, and CN substituents marginally affected the absorption spectra of **2–5**, and **9**, respectively, with a slight red-shift in the λ_{max} values compared with **1** (Table 1), and the compounds underwent reversible photoisomerization similar to that of parent **1** (Figures 39b–e, 42–46, and Table 1). Interestingly, **3** and **4** with bulky Cl and Br at the phenyl *ortho* positions, respectively, presented highly efficient *E*→*Z* photoisomerization compared with **1**, resulting in 96% *Z* isomers at 405_{PSS} (Figures 39c). However, the $n \rightarrow \pi^*$ spectral band of the *Z* isomers partially overlapped with that of the *E* isomers, causing less efficient *Z*→*E* photoisomerization and providing only 65% *E* isomers at 525_{PSS} (Figure 39c and Table 1). The electron-donating NH₂ (**6**), NHMe (**7**), NMe₂ (**8** and **10**), and OMe (**11**) substituents considerably affected the absorption spectra, with a 20–161 nm

red-shift in the λ_{max} values compared with **1** (Figure 39i). Importantly the $E \rightarrow Z$ and $Z \rightarrow E$ photoisomerizations occurred under longer wavelengths of 470 or 525 nm and 625 nm light irradiation, respectively, for **6**, **7**, and **10** (Figures 39d, 53 and 54). Because of the fast thermal relaxation kinetics of **7** and **10**, I also conducted laser flash photolysis, which showed a sudden decrease in absorbance at 508 nm (for **7**) and 476 nm (for **10**) and an increase in absorbance at 550 nm (for **10**) followed by a slow recovery of the original absorbance (Figures 39g, 39h, and 56). To my surprise, **11** showed the best forward $E \rightarrow Z$ (92%) and reverse $Z \rightarrow E$ (88%) photoisomerization abilities, which is probably attributable to the optimum spectral separation of the $\pi \rightarrow \pi^*$ ($\Delta\lambda_{\text{max}} = 53$ nm) and $n \rightarrow \pi^*$ ($\Delta\lambda_{\text{max}} \cong 5$ nm) transition bands of the E and Z isomers, respectively (Figure 52 and Table 1). Compounds **1–6**, **9**, and **11** underwent reversible $E \rightarrow Z$ photoisomerization for many cycles with no degradation, indicating high fatigue resistance (Figures 39a–f insets), which is required for photopharmacological applications. However, **8** with NMe₂ substituents at the phenyl *ortho* position decomposed after light irradiation (Figure 55). I measured the quantum yields (Φ) of **1–5**, **9**, and **11** at 405 nm for the $E \rightarrow Z$ photoisomerization using ferrioxalate actinometry. For the $Z \rightarrow E$ photoisomerization, the Φ values were calculated to be in the ranges of 0.17–0.45 ($E \rightarrow Z$) and 0.31–0.78 ($Z \rightarrow E$) (Table 1-8 and Figures 57-63). The half-lives of the Z isomers and the $Z \rightarrow E$ thermal isomerization kinetics were studied using absorption spectroscopy or laser flash photolysis in acetonitrile solution at 25°C (Table 1). Compounds **1–6**, **9**, and **11** followed first-order thermal isomerization kinetics, and their half-lives ($t_{1/2}$) were calculated from the rate constants (Table 1 and Figures 64–119). I observed a reasonably stable Z isomer of parent **1** ($t_{1/2} = 2.8$ h) and a destabilization effect when the electron-donating OMe substituent was present, as in the case of **11** ($t_{1/2} = 14.8$ min). In contrast, electron-withdrawing halogen substituents

at the phenyl *ortho* position further stabilized the *Z* isomers. Compound **4** with a Br substituent showed the longest half-life ($t_{1/2} = 7.2$ h) among all the **PAT** photoswitches studied (Table 1). Interestingly, despite its strong electron-withdrawing character, the *Z* isomer of **9** with CN substituents at the phenyl *para* position destabilized ($t_{1/2} = 1.7$ h) compared with parent **1** (Table 1). Importantly, the $t_{1/2}$ values for the *Z* isomers of **6**, **7**, and **10** were 45, 6, and 2 s, respectively, which were much longer than those of green-light switchable azobenzene derivatives. For instance, the $t_{1/2}$ value of the *Z* isomer of 4-dimethylamino-4'-nitroazobenzene, which isomerizes when exposed to >470 nm irradiation, is in the order of milliseconds.⁵⁹ Compounds **6**, **7**, and **10** underwent *E*→*Z* photoisomerization when exposed to 525 nm irradiation, but their $t_{1/2}$ values were in the order of seconds. To maintain a *Z*-rich state in photopharmacological applications, no light irradiation or less frequent flashes are enough for compounds with *Z* isomers showing $t_{1/2}$ values in the order of hours or tens of minutes, whereas continuous irradiation of an active light is necessary for those showing $t_{1/2}$ values in the order of seconds. The activation energy (E_a), enthalpy (ΔH^\ddagger), entropy (ΔS^\ddagger), and Gibbs free energy (ΔG^\ddagger) were determined using the Arrhenius and Eyring plots of the *Z*→*E* thermal isomerization kinetics in acetonitrile solution at five different temperatures (5°C–35°C) (Table 1 and Figures 64-119).

The effect of water in the solvent on the photophysical and thermal isomerization properties was also studied for **1**, **6**, **7**, and **11**. Although the water in the media had little effect on **1** and **11**, the $t_{1/2}$ values of **6** and **7** with amino substituents decreased after changing the solvent from acetonitrile to an acetonitrile/water (50/50, v/v) mixture (Figure 120 and Table 10).

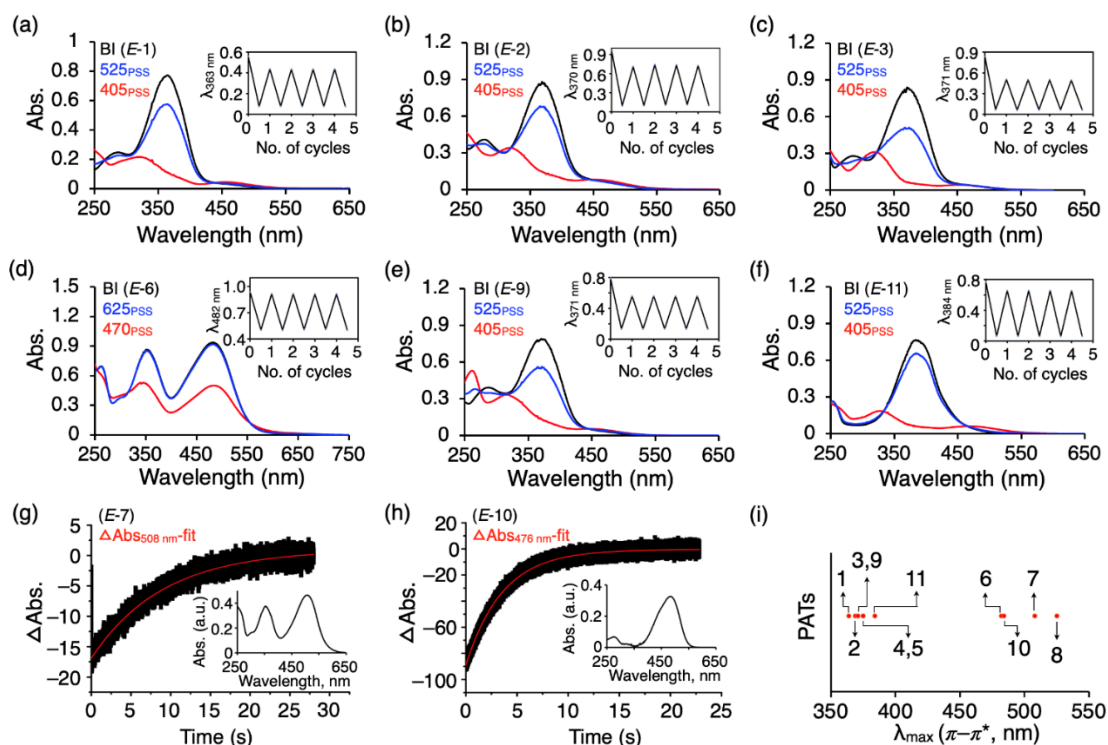
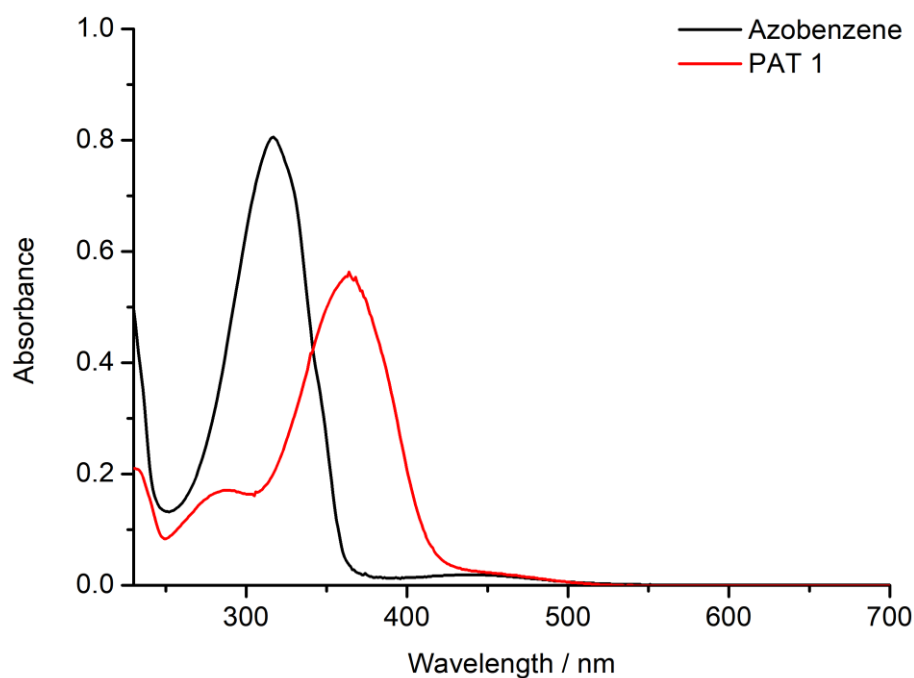


Figure 39. (a–f) UV–visible absorption spectra of **1–3**, **6**, **9**, and **11** in acetonitrile at 25°C before irradiation (BI, black lines), the PSS of 405 nm or 470 nm (405_{PSS}, 470_{PSS}, red lines) and 525 nm or 625 nm irradiation (525_{PSS}, 625_{PSS}, blue lines). Absorbance changes at λ_{max} obtained by repeated irradiation at the PSS (insets). (g, h) Absorbance changes of **7** and **10** at 508 nm and 476 nm, respectively, obtained using laser flash photolysis (fit, red curve). (i) Graph of λ_{max} values of **1–11** showing the shift of their λ_{max} to longer wavelengths.

Table 1. Spectral and kinetic data for 1–11.

PAT	$\pi\text{-}\pi^*$ (E)		$n\text{-}\pi^*$ (E)		Conversion (%)		$t_{1/2}$ (25 °C) h	E_a kJ mol ⁻¹	ΔH^\ddagger kJ mol ⁻¹	ΔS^\ddagger J mol ⁻¹ K ⁻¹	ΔG^\ddagger (25 °C) kJ/mol	ϕ E→Z	ϕ Z→E
	λ_{\max} nm	ϵ M ⁻¹ cm ⁻¹	λ_{\max} nm	ϵ M ⁻¹ cm ⁻¹	E→Z (405 nm)	Z→E (525 nm)							
1	364	19723	459	769	85	81	2.8	87.9	85.4	-38.4	96.8	0.24	0.78
2	369	18592	458	969	90	77	5.5	94.2	91.7	-20.8	97.9	0.31	0.43
3	371	12738	471	692	96	62	6.6	94.5	92.0	-23.0	98.8	0.45	0.31
4	375	14903	477	666	96	62	7.2	90.5	88.0	-37.7	99.3	0.27	0.44
5	375	12521	498	389	91	72	3.6	86.8	84.4	-43.8	97.4	0.17	0.61
6	351 482	9788 10895	—	—	>58* (470 nm) >48* (525 nm)	>97* (625 nm)	45 s	76.1	73.1	-32.7	83.4	—	—
7	353 508	11262 14591	—	—	>37* (470 nm) >41* (525 nm)	>89* (625 nm)	6 s	—	—	—	—	—	—
8	365 525	3675 3278	—	—	—	—	—	—	—	—	—	—	—
9	371	23049	468	653	88	76	1.7	74.6	72.2	-78.6	95.6	0.21	0.71
10	484	28830	—	—	>68* (470 nm) >52* (525 nm)	>99* (625 nm)	2 s	—	—	—	—	—	—
11	384	25944	—	—	>92	86	0.25	80.8	78.3	-41.6	90.7	0.34	—

* Conversion at the PSS was estimated based on the NMR results except for **6**, **7**, **10**, and **11**, for which the absorbance spectra were used. Half-life was calculated from the absorbance changes at thermal Z–E isomerization except for **7** and **10**, for which laser flash photolysis was used.

**Figure 40:** Absorption spectra of **PAT 1** (red) showing a redshift compared to the absorption spectra of azobenzene (black) in CH₃CN at 25 °C.

2.2.1 Measurement of isomer conversion at PSS by NMR (PAT 1–5, 9 and 11).

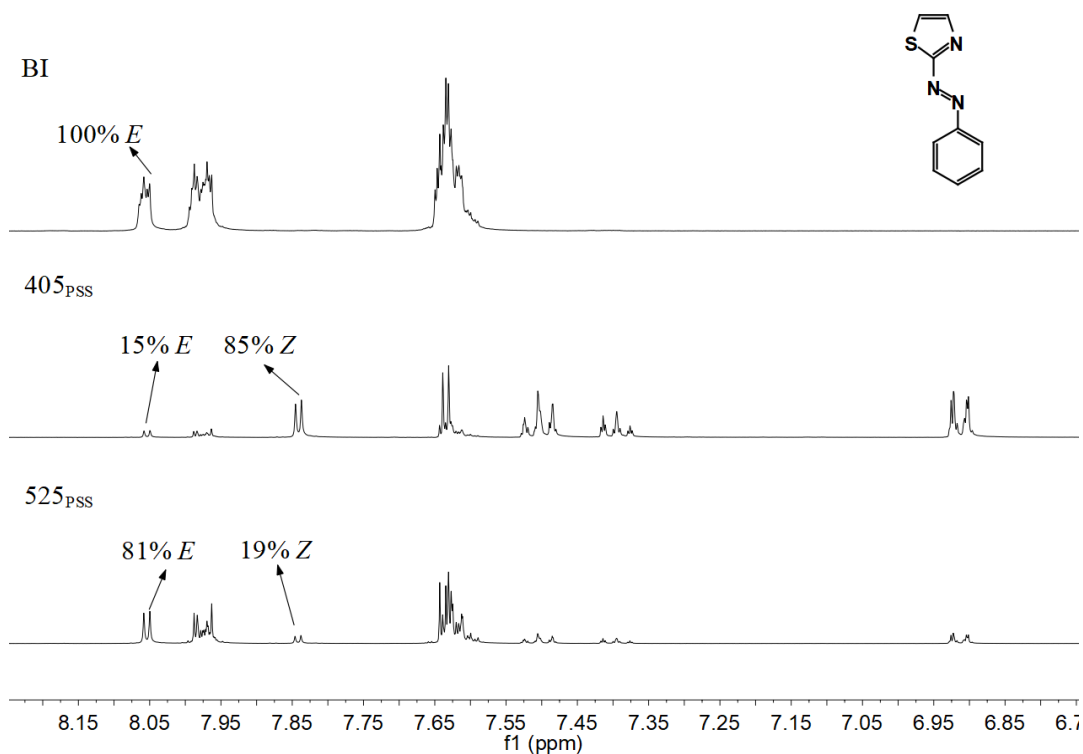


Figure 41: ^1H NMR spectra (400 MHz, CD_3CN) of **PAT 1** obtained before irradiation (BI) and after irradiations at PSS of 405 nm (405_{PSS}) and 525 nm (525_{PSS}) at room temperature.

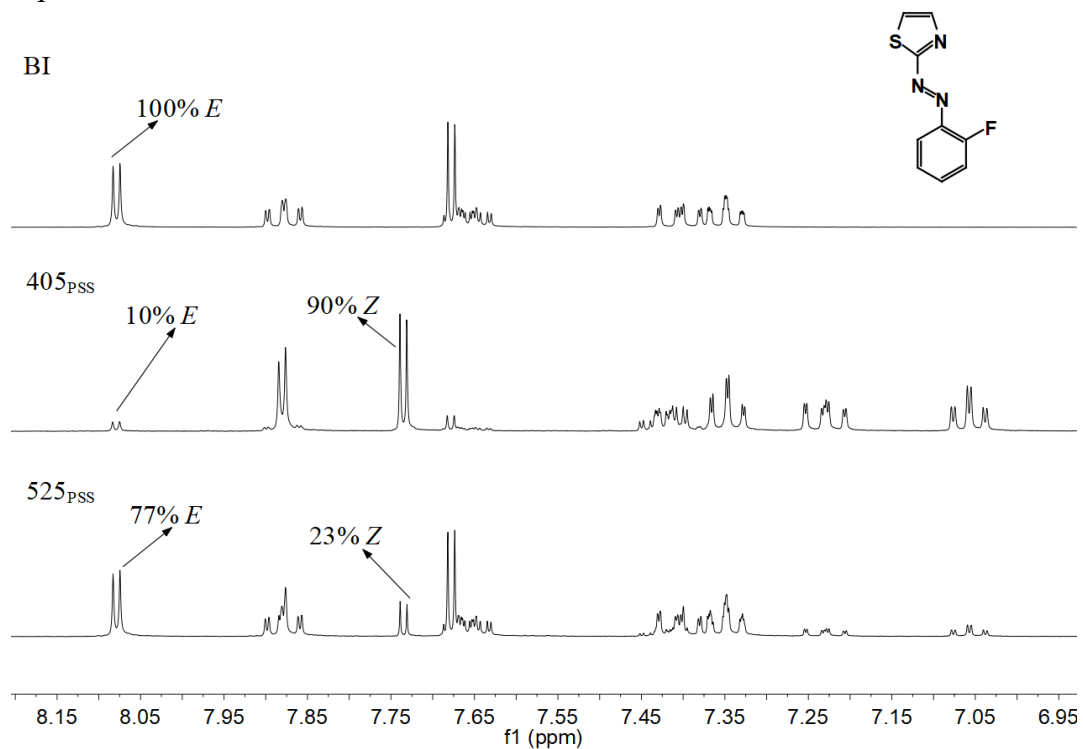


Figure 42: ^1H NMR spectra (400 MHz, CD_3CN) of **PAT 2** obtained before irradiation (BI) and after irradiations at PSS of 405 nm (405_{PSS}) and 525 nm (525_{PSS}) at room temperature.

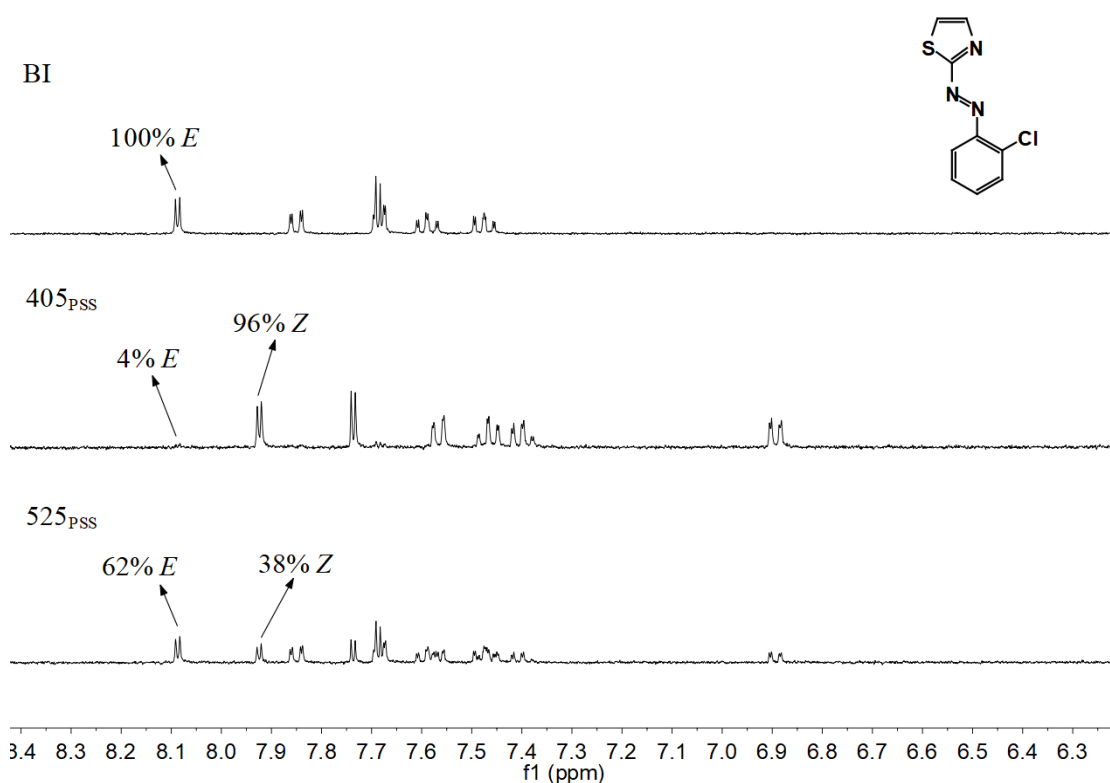


Figure 43: ^1H NMR spectra (400 MHz, CD_3CN) of **PAT 3** obtained before irradiation (BI) and after irradiations at PSS of 405 nm (405_{PSS}) and 525 nm (525_{PSS}) at room temperature.

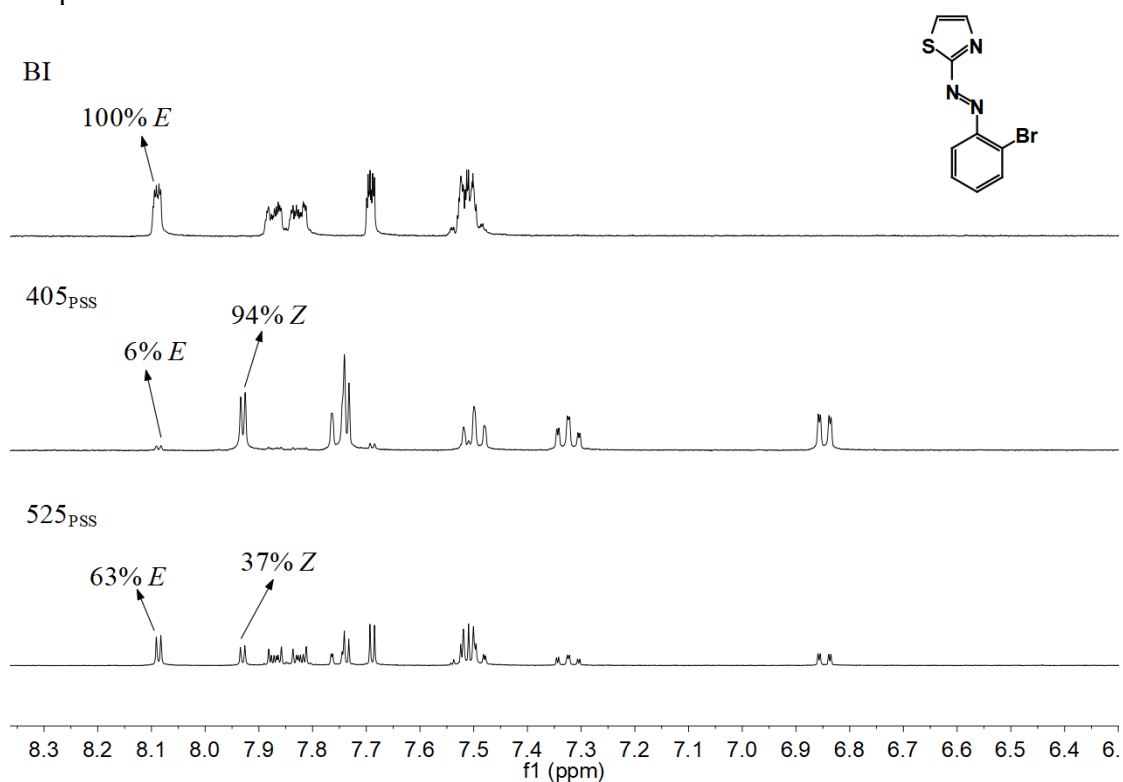


Figure 44: ^1H NMR spectra (400 MHz, CD_3CN) of **PAT 4** obtained before irradiation (BI) and after irradiations at PSS of 405 nm (405_{PSS}) and 525 nm (525_{PSS}) at room temperature.

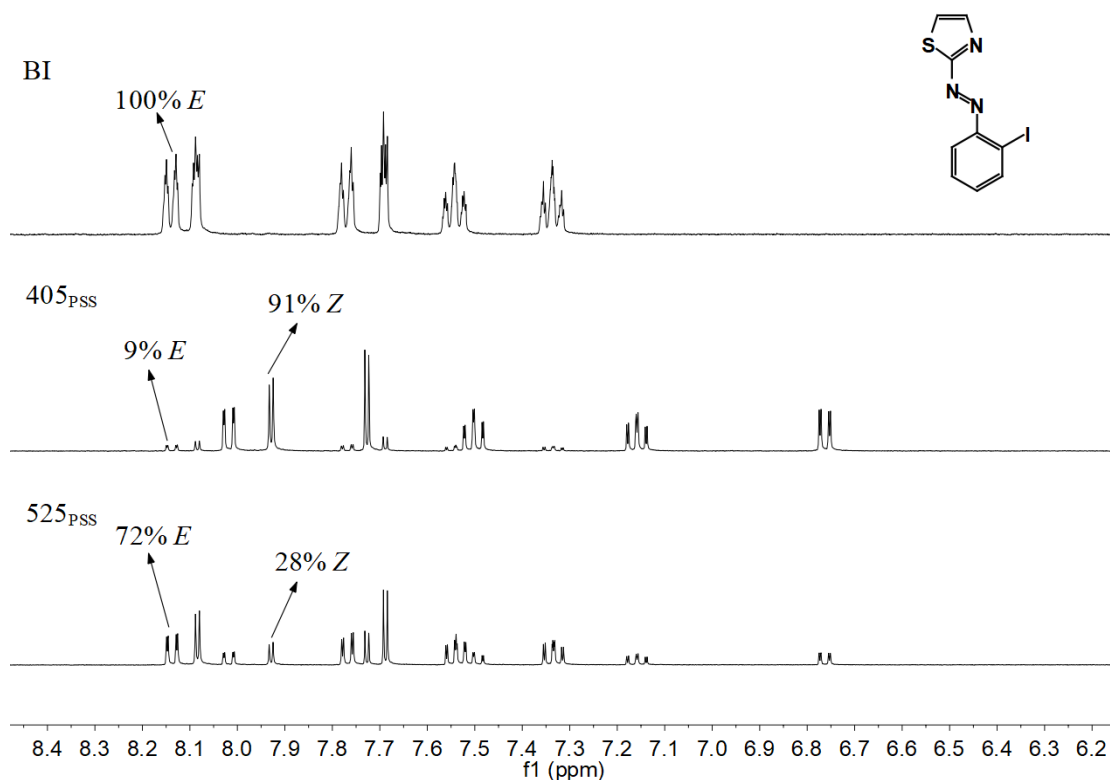


Figure 45: ^1H NMR spectra (400 MHz, CD_3CN) of **PAT 5** obtained before irradiation (BI) and after irradiations at PSS of 405 nm (405_{PSS}) and 525 nm (525_{PSS}) at room temperature.

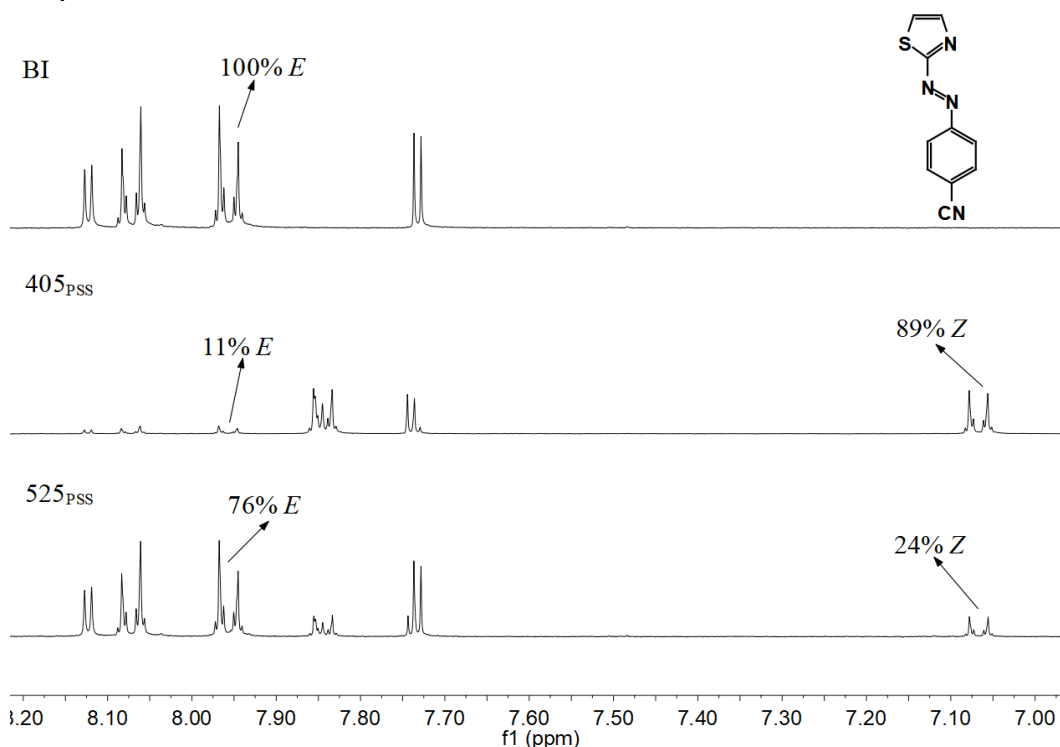


Figure 46: ^1H NMR spectra (400 MHz, CD_3CN) of **PAT 9** obtained before irradiation (BI) and after irradiations at PSS of 405 nm (405_{PSS}) and 525 nm (525_{PSS}) at room temperature.

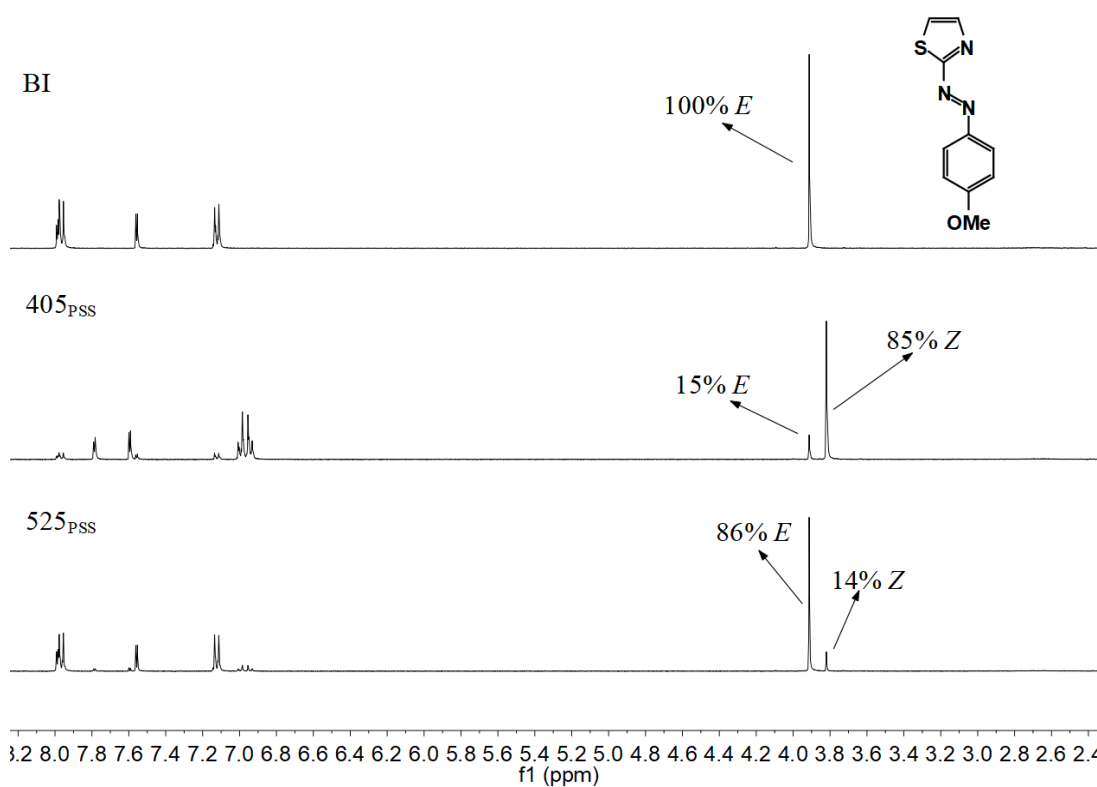


Figure 47: ^1H NMR spectra (400 MHz, CD_3CN) of **PAT 11** obtained before irradiation (BI) and after irradiations at PSS of 405 nm (405_{PSS}) and 525 nm (525_{PSS}) at room temperature.

2.2.2 Measurement of isomer conversion at PSS by absorption spectra (PAT 11)

Due to short half-life of **PAT 11** (14 min at 25 °C), the isomer ratios at PSS obtained by NMR analysis were inaccurate and hence used the absorption spectroscopy for isomer ratios calculation at PSS. When the extinction coefficient of Z isomer of PAT 11 (ϵ_Z) at λ_{\max} (384 nm) was zero, then the isomer ratios at PSS was calculated using the equation:

$$\chi_E = \frac{A_0}{A_{PSS}}$$

χ_E E isomer ratio at PSS

A_0 Absorbance at initial state at λ_{\max}

A_{PSS} Absorbance at PSS at λ_{\max}

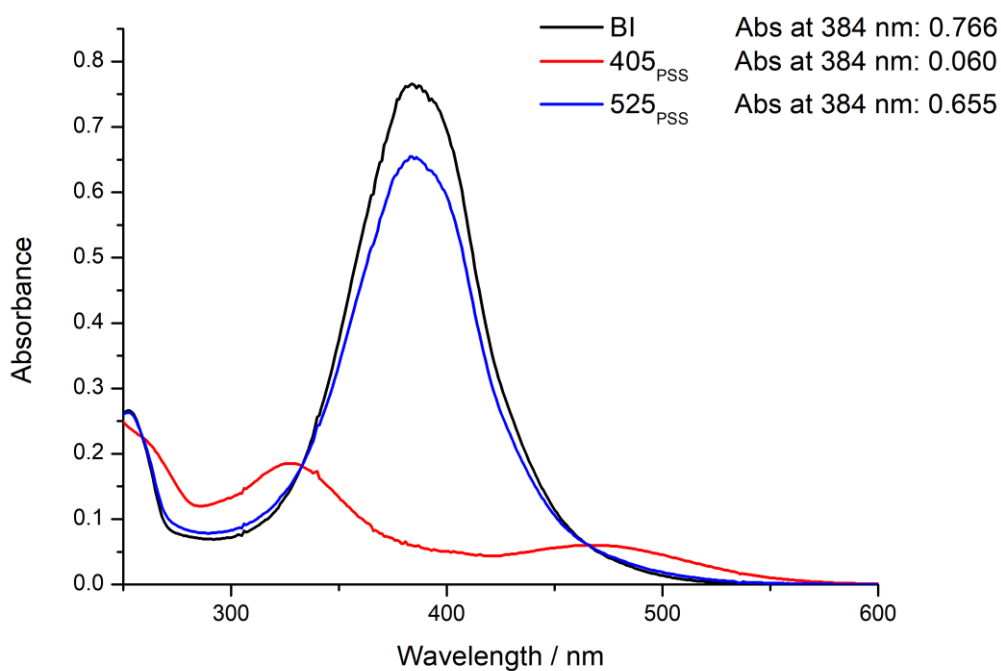


Figure 48: Absorption spectra of **PAT 11** in CH₃CN before (BI) and after irradiations at PSS of 405 nm (405_{PSS}) and 525 nm (525_{PSS}) at room temperature. Calculated isomer ratios were 8:92 ($E:Z$) at 405_{PSS} and 86:14 ($E:Z$) at 525_{PSS}.

2.2.3 Absorption spectra of PAT derivatives

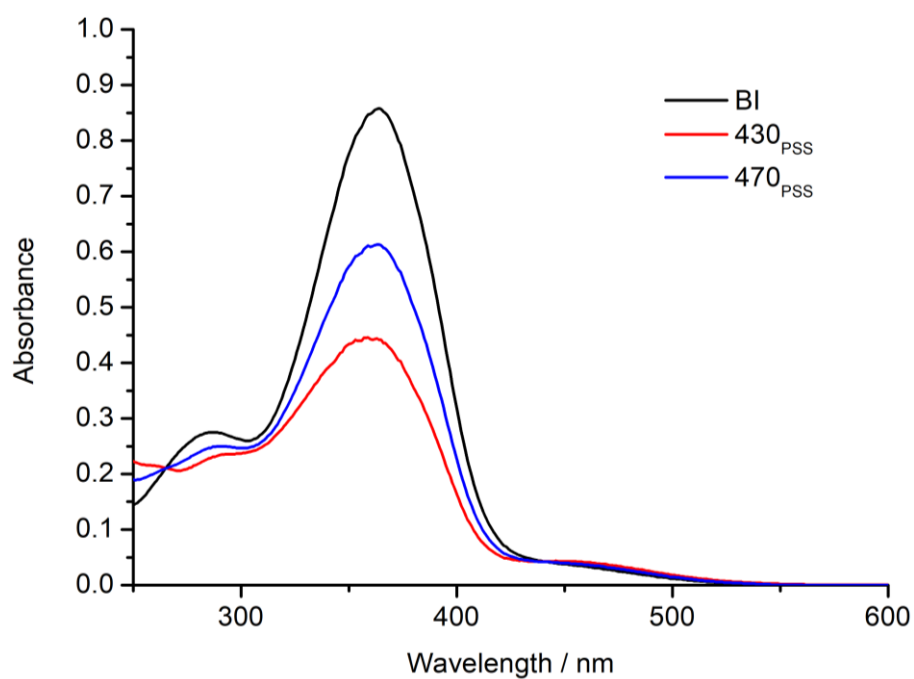


Figure 49: Absorption spectra of **PAT 1** in CH₃CN before (BI) and after irradiations at PSS of 430 nm (430_{PSS}) and 470 nm (470_{PSS}) at room temperature.

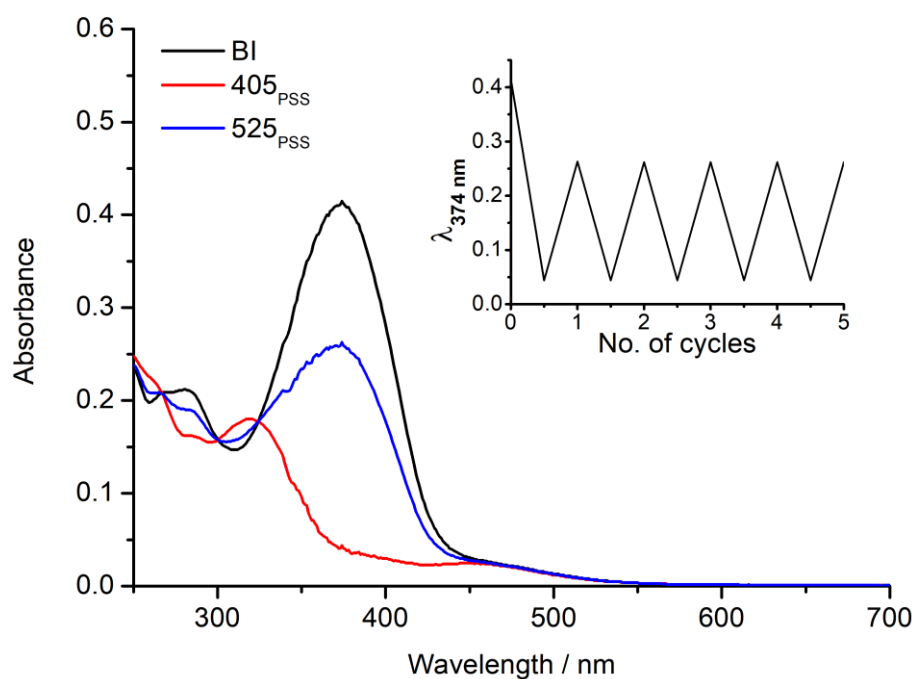


Figure 50: Absorption spectra of **PAT 4** in CH₃CN before (BI) and after irradiations at PSS of 405 nm (405_{PSS}) and 525 nm (525_{PSS}) at room temperature. Absorbance changes at λ_{max} obtained by repeated irradiations (inset)

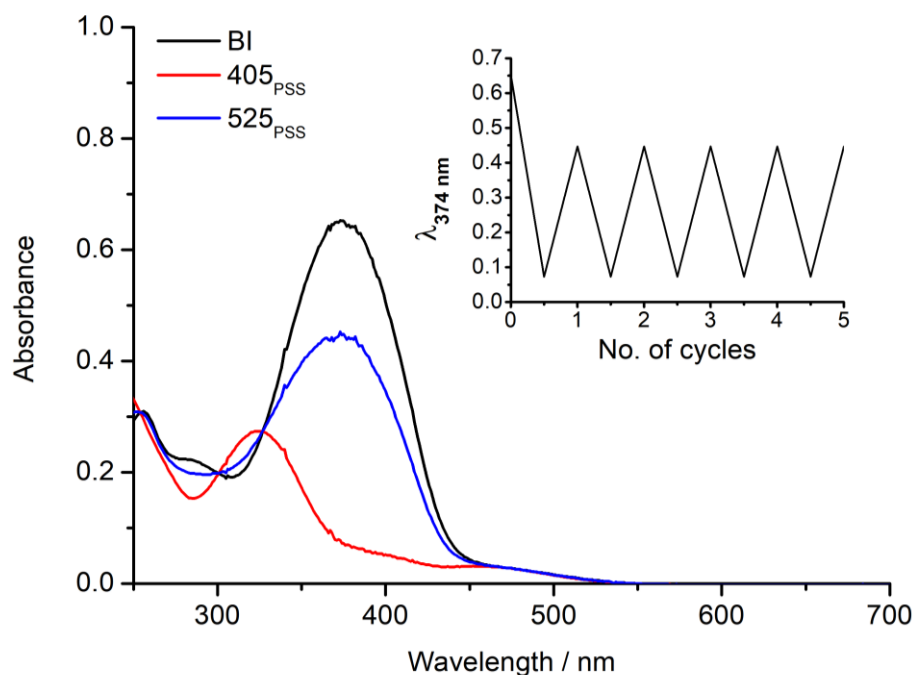


Figure 51: Absorption spectra of **PAT 5** in CH_3CN before (BI) and after irradiations at PSS of 405 nm (405_{PSS}) and 525 nm (525_{PSS}) at room temperature. Absorbance changes at λ_{max} obtained by repeated irradiations (inset)

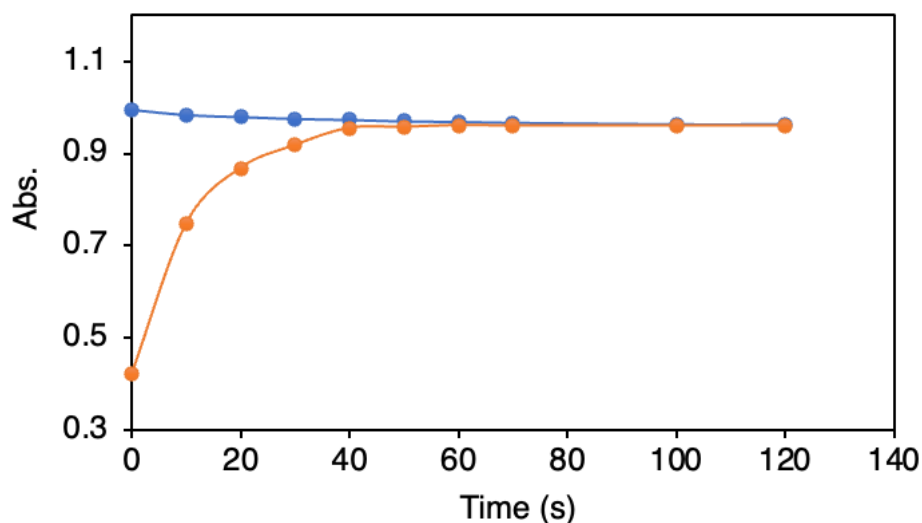


Figure 52: Graph showing the change in absorbance at λ_{max} of **PAT 6** over time. Blue curve represents the change in absorbance at λ_{max} observed after irradiation of 625 nm to the non-irradiated solution. Orange curve represents change in absorbance at λ_{max} observed after irradiation of 625 nm to the pre-irradiated solution at PSS of 470 nm (470_{PSS}). This experiment was conducted to ensure the accuracy of *trans* and *cis* isomers composition at 625 nm PSS minimizing the artifacts from *Z-E* thermal back isomerization.

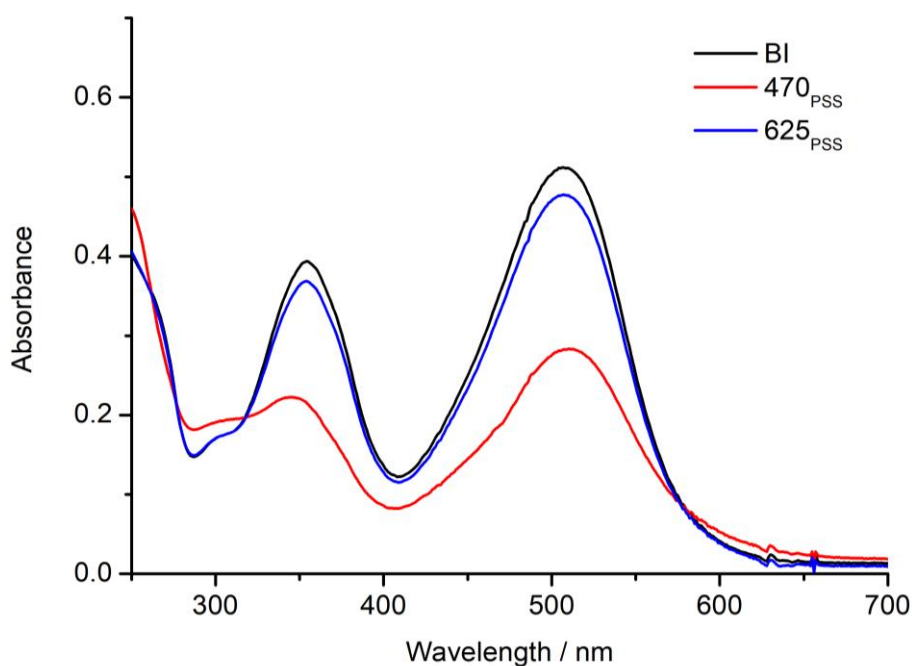


Figure 53: Absorption spectra of **PAT 7** before irradiation (BI, black), while *in situ* irradiation with 470 nm (470_{PSS}, red) followed by 625 nm (625_{PSS}, blue). The change in absorption spectra indicates the photoconversion between *cis* and *trans* isomers of **PAT 7**.

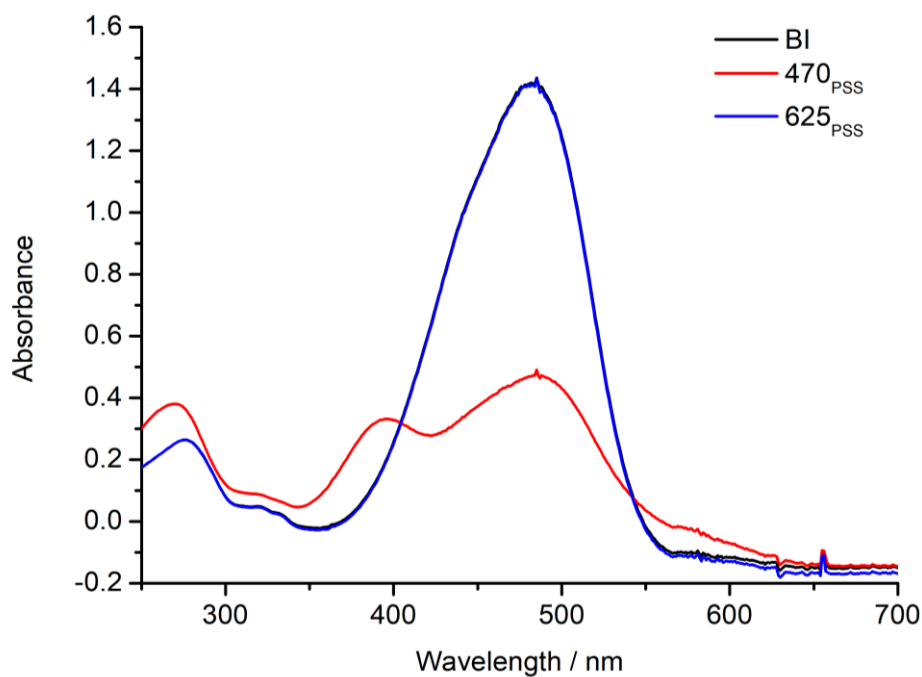


Figure 54: Absorption spectra of **PAT 10** before irradiation (BI, black), while *in situ* irradiation with 470 nm (470_{PSS}, red) followed by 625 nm (625_{PSS}, blue). The change in absorption spectra indicates the photoconversion between *cis* and *trans* isomers of **PAT 10**.

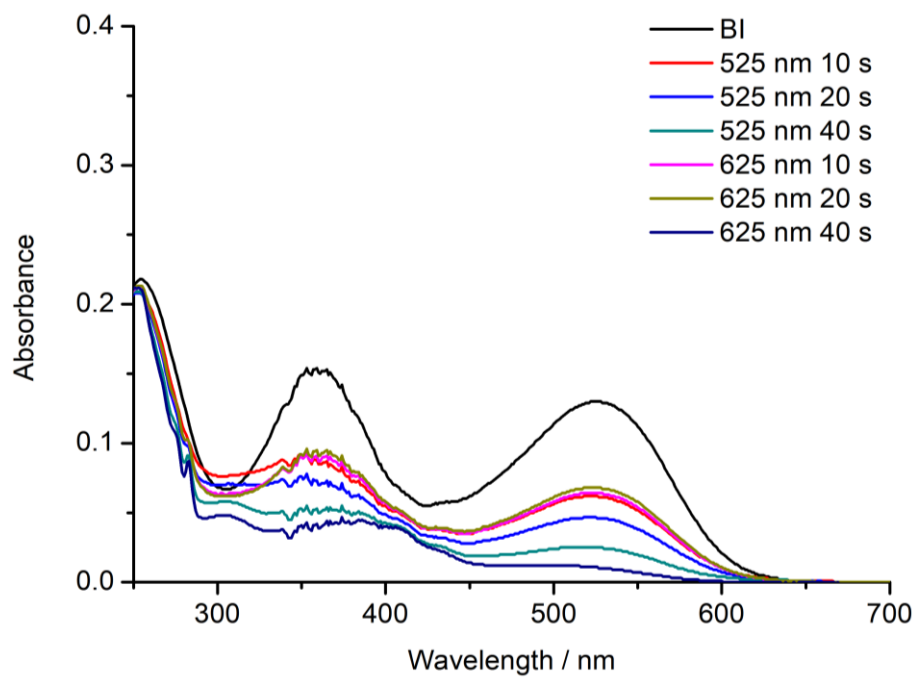


Figure 55: Absorption spectra of **PAT 8** in CH_3CN before (BI) and after irradiations at PSS of 525 nm (405_{PSS}) and 625 nm (525_{PSS}) at room temperature. A decrease of absorbance was observed after irradiation and the irradiated solution became colorless indicating the photodecomposition.

2.2.4 Laser flash photolysis

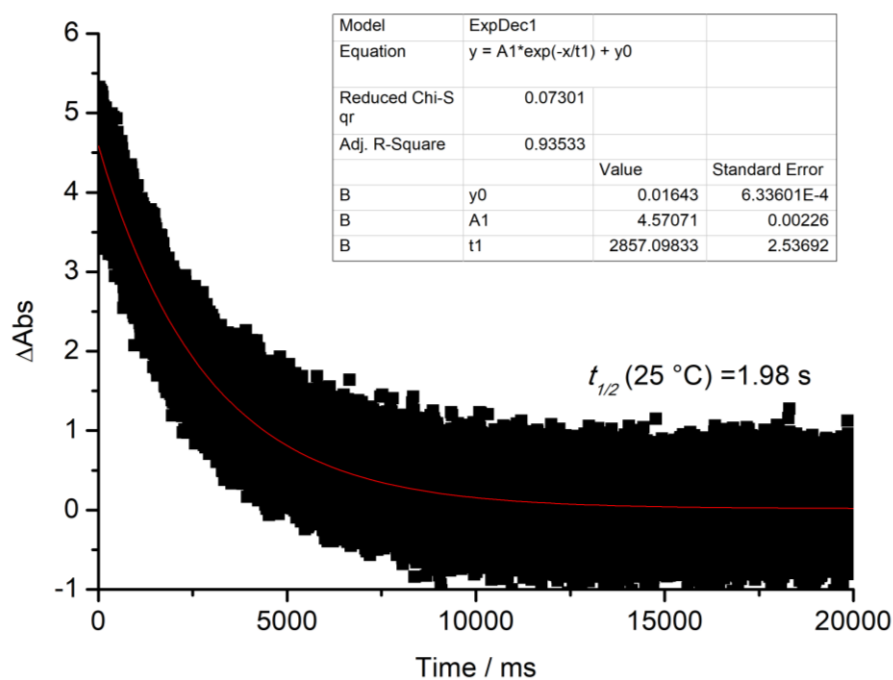


Figure 56: Flash photolysis experiment of **PAT 10** at monitoring wavelength of 550 nm (25.0 °C). Black and red curves represent experimental flash photolysis curve and exponential fitting curve, respectively.

2.2.5 Isomerization quantum yields

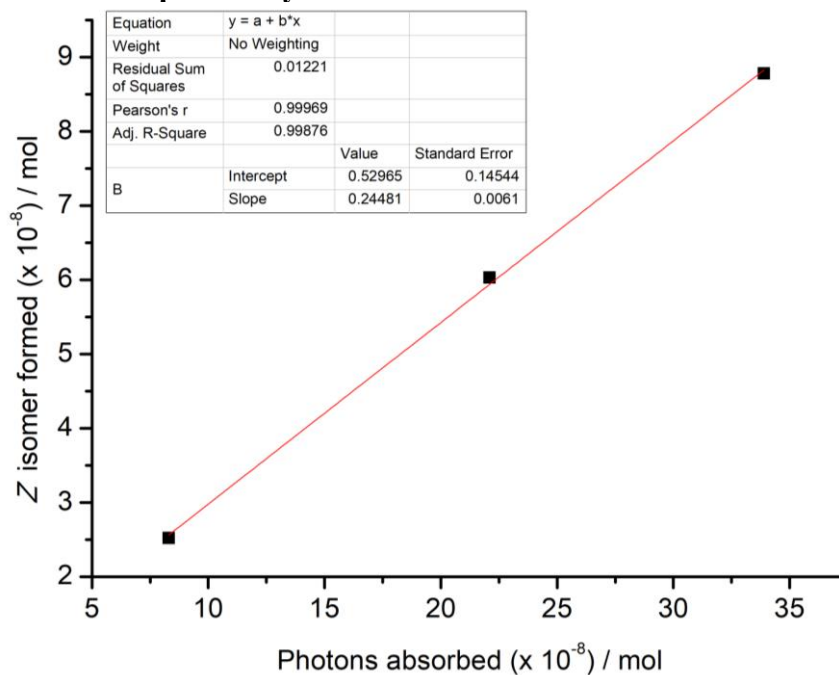


Figure 57: Graph showing the amount of Z-isomer of **PAT 1** formed for the different light intensity (0.15–0.56 W/cm²). Photons absorbed by **PAT 1** were calculated and the slope of the graph gives the quantum yield for the *E*–*Z* isomerization of **PAT 1**.

χ_E	χ_Z	ε_E	ε_Z	ε'_E	ε'_Z	ϕ_{E-Z}	ϕ_{Z-E}
0.15	0.85	19723	59	5138	279	0.24	0.78

Table 2: Table showing the calculated values and *E*–*Z* and *Z*–*E* isomerization quantum yields of **PAT 1** at 405 nm light irradiation.

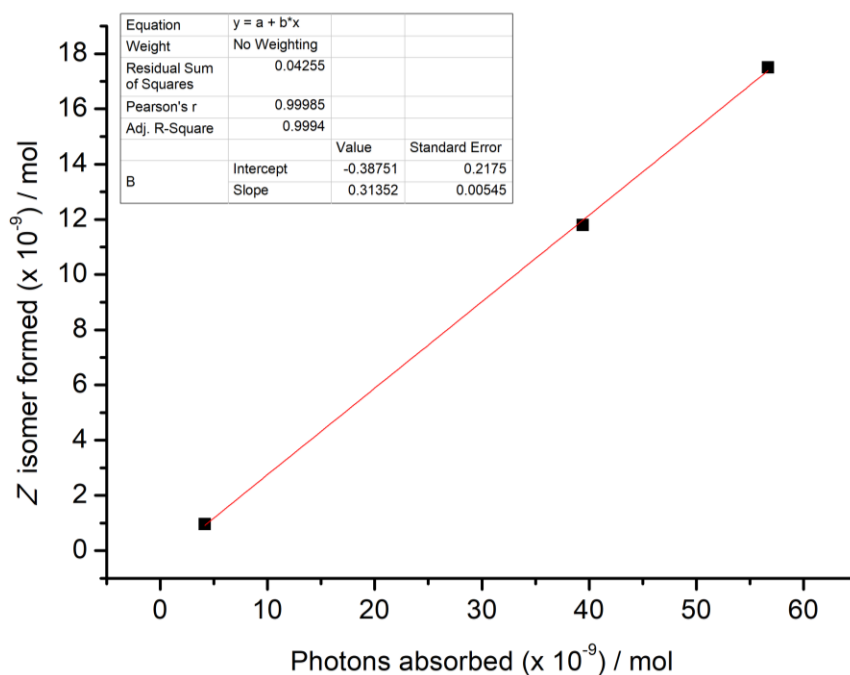


Figure 58: Graph showing the amount of Z-isomer of **PAT 2** formed for the different light intensity. Photons absorbed by **PAT 2** were calculated and the slope of the graph gives the quantum yield for the *E*–*Z* isomerization of **PAT 2**.

χ_E	χ_Z	ϵ_E	ϵ_Z	ϵ'_E	ϵ'_Z	ϕ_{E-Z}	ϕ_{Z-E}
0.1	0.9	18592	247	7492	598	0.31	0.43

Table 3: Table showing the calculated values and *E*–*Z* and *Z*–*E* isomerization quantum yields of **PAT 2** at 405 nm light irradiation.

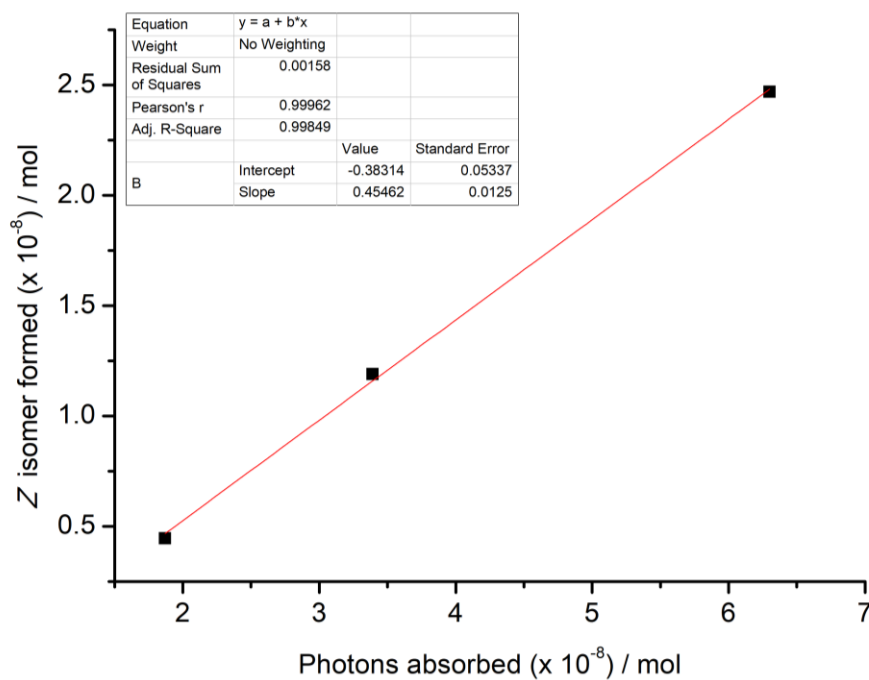


Figure 59: Graph showing the amount of Z-isomer of **PAT 3** formed for the different light intensity. Photons absorbed by **PAT 3** were calculated and the slope of the graph gives the quantum yield for the *E*–*Z* isomerization of **PAT 3**.

χ_E	χ_Z	ε_E	ε_Z	ε'_E	ε'_Z	ϕ_{E-Z}	ϕ_{Z-E}
0.04	0.96	12738	617	6738	407	0.45	0.31

Table 4: Table showing the calculated values and *E*–*Z* and *Z*–*E* isomerization quantum yields of **PAT 3** at 405 nm light irradiation.

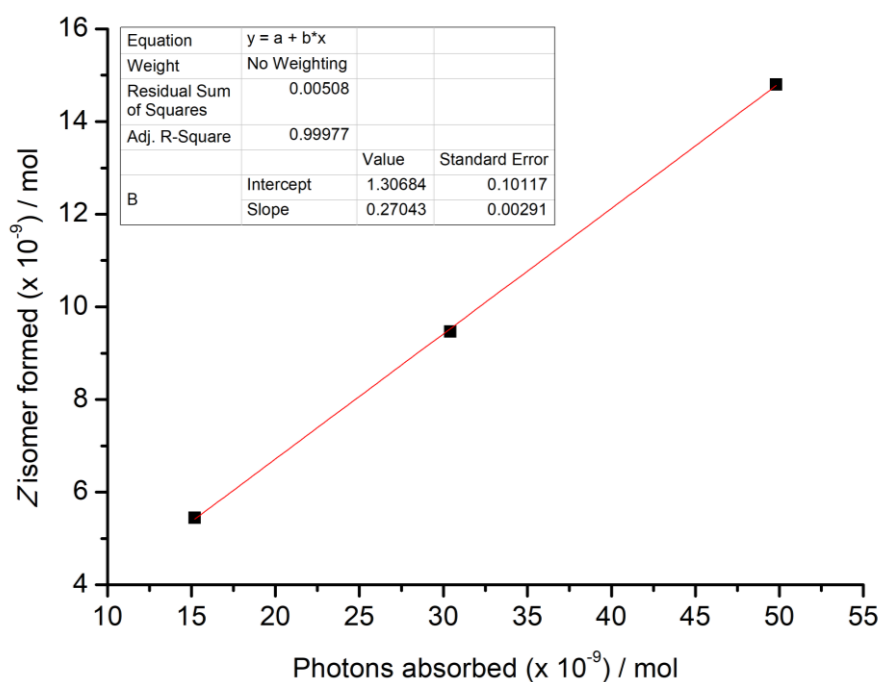


Figure 60: Graph showing the amount of Z-isomer of **PAT 4** formed for the different light intensity. Photons absorbed by **PAT 4** were calculated and the slope of the graph gives the quantum yield for the *E*–*Z* isomerization of **PAT 4**.

χ_E	χ_Z	ε_E	ε_Z	ε'_E	ε'_Z	ϕ_{E-Z}	ϕ_{Z-E}
0.06	0.94	14903	326	8521	333	0.27	0.44

Table 5: Table showing the calculated values and *E*–*Z* and *Z*–*E* isomerization quantum yields of **PAT 4** at 405 nm light irradiation.

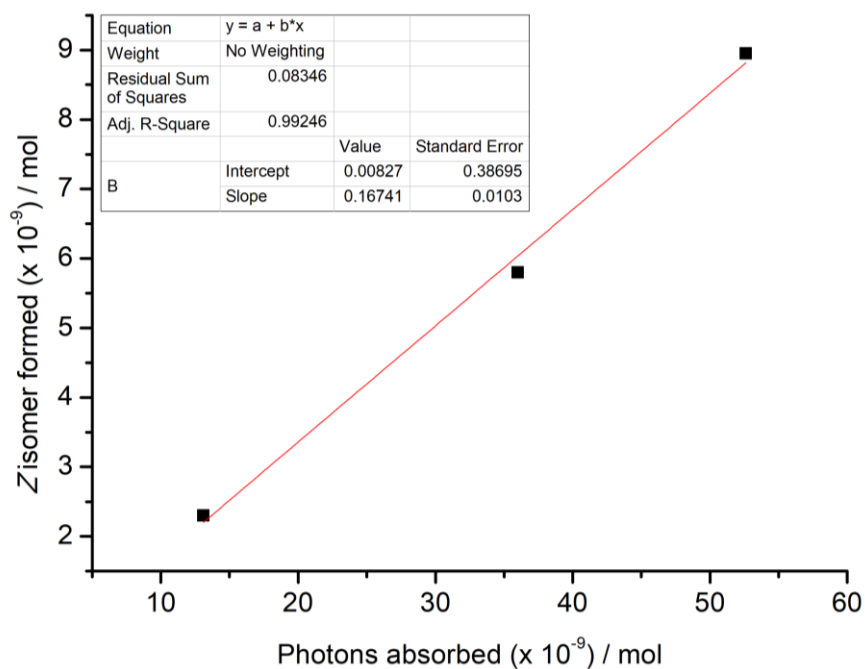


Figure 61: Graph showing the amount of Z-isomer of **PAT 5** formed for the different light intensity. Photons absorbed by **PAT 5** were calculated and the slope of the graph gives the quantum yield for the *E*–*Z* isomerization of **PAT 5**.

χ_E	χ_Z	ϵ_E	ϵ_Z	ϵ'_E	ϵ'_Z	ϕ_{E-Z}	ϕ_{Z-E}
0.09	0.91	12521	386	8637	239	0.17	0.61

Table 6: Table showing the calculated values and *E*–*Z* and *Z*–*E* isomerization quantum yields of **PAT 5** at 405 nm light irradiation.

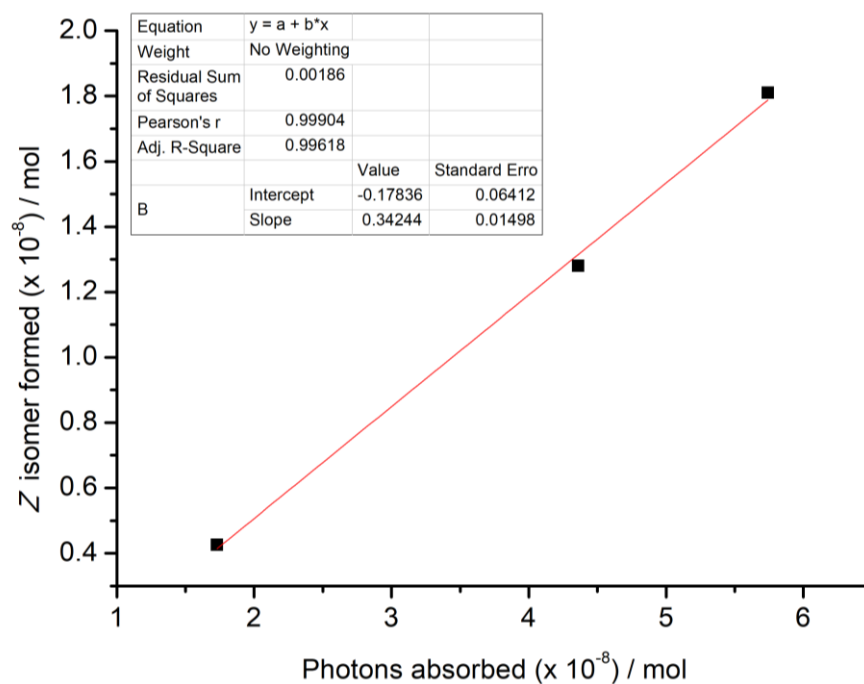


Figure 62: Graph showing the amount of Z-isomer of **PAT 9** formed for the different light intensity. Photons absorbed by **PAT 9** were calculated and the slope of the graph gives the quantum yield for the *E*–*Z* isomerization of **PAT 9**.

χ_E	χ_Z	ϵ_E	ϵ_Z	ϵ'_E	ϵ'_Z	ϕ_{E-Z}	ϕ_{Z-E}
0.12	0.88	14632	361	7234	356	0.34	0.94

Table 7: Table showing the calculated values and *E*–*Z* and *Z*–*E* isomerization quantum yields of **PAT 9** at 405 nm light irradiation.

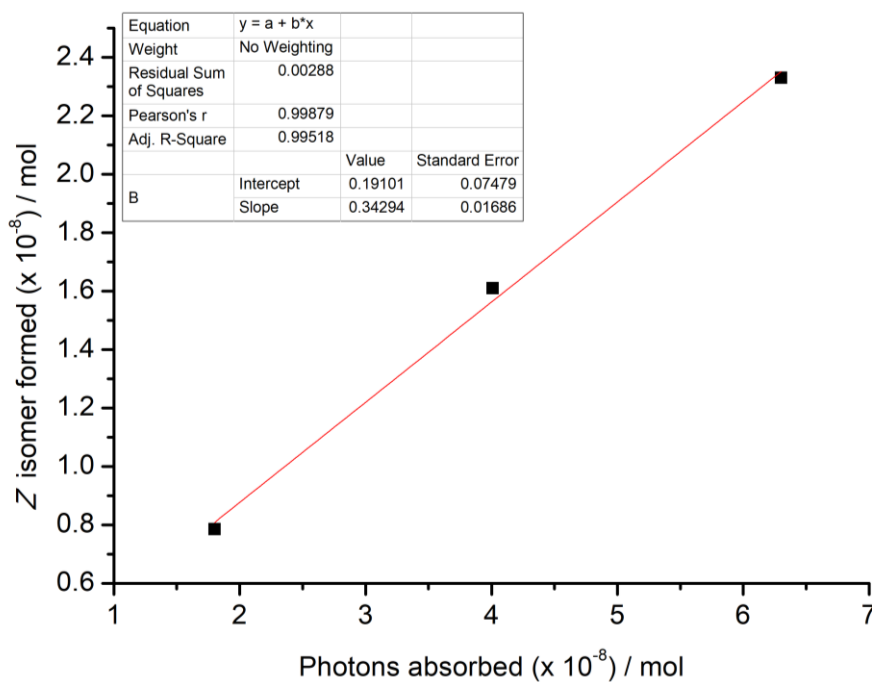


Figure 63: Graph showing the amount of Z-isomer of **PAT 11** formed for the different light intensity. Photons absorbed by **PAT 11** were calculated and the slope of the graph gives the quantum yield for the *E*–*Z* isomerization of **PAT 11**.

χ_E	χ_Z	ϵ_E	ϵ_Z	ϵ'_E	ϵ'_Z	ϕ_{E-Z}	ϕ_{Z-E}
<0.08	>0.92	25944	-	21000	-	0.34	-

Table 8: Table showing the calculated values and *E*–*Z* isomerization quantum yield of **PAT 11** at 405 nm light irradiation. *Z*–*E* isomerization quantum yield was difficult to estimate due to the effect of thermal back isomerization.

2.2.6 Kinetics for half-lives, Arrhenius plots and Eyring Plots.

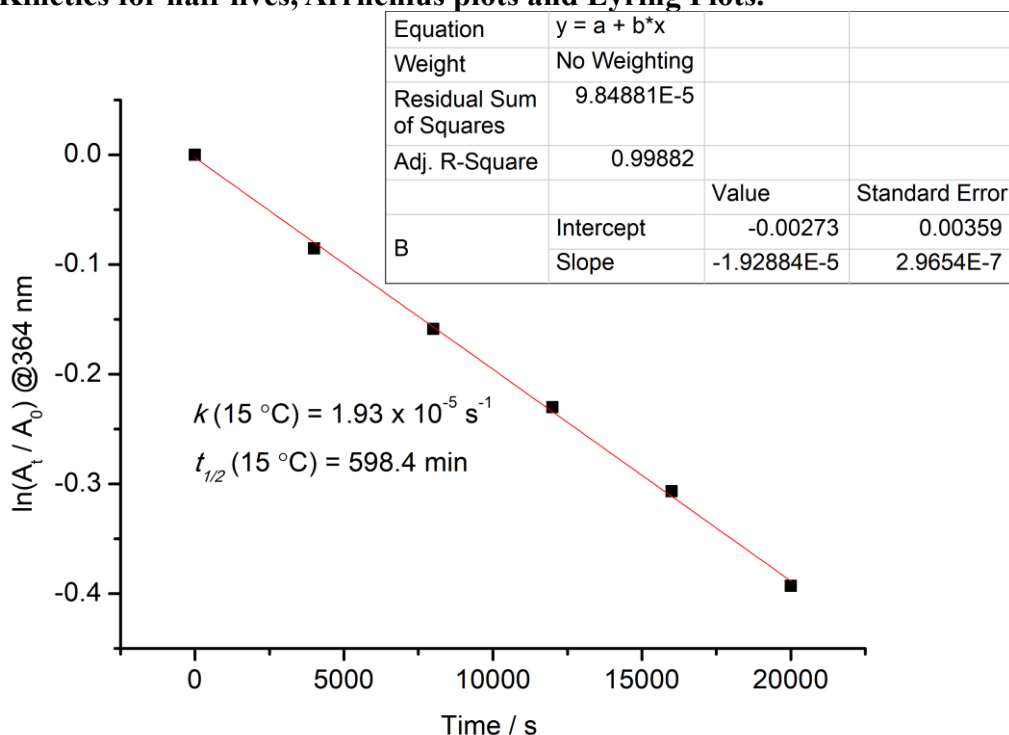


Figure 64: Graph showing the linear fit of the change in absorbance at 364 nm over time at 15 °C (PAT 1). Rate constant k (= slope) and calculated $t_{1/2}$ are mentioned.

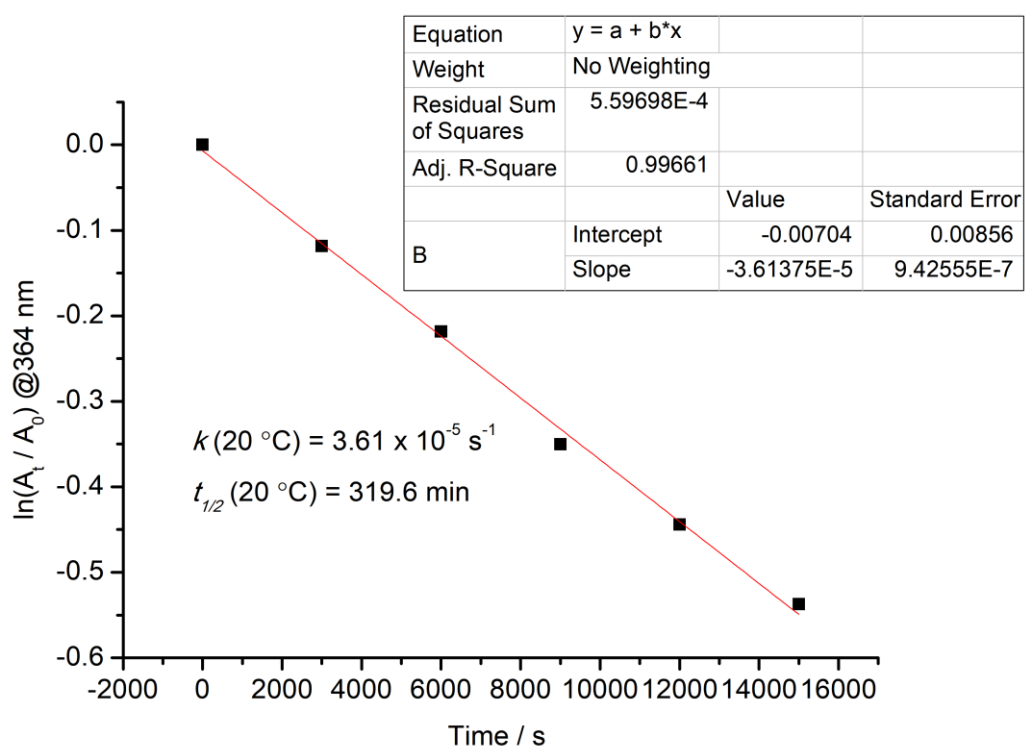


Figure 65: Graph showing the linear fit of the change in absorbance at 364 nm over time at 20 °C (PAT 1). Rate constant k (= slope) and calculated $t_{1/2}$ are mentioned.

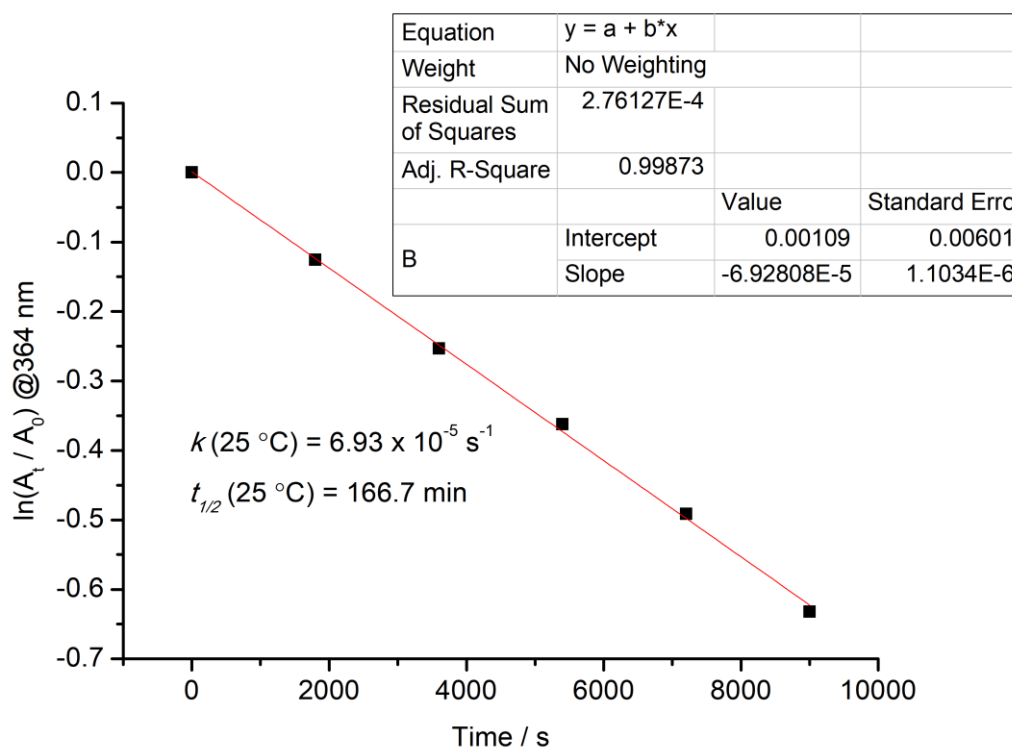


Figure 66: Graph showing the linear fit of the change in absorbance at 364 nm over time at 25 °C (PAT 1). Rate constant k (= slope) and calculated $t_{1/2}$ are mentioned.

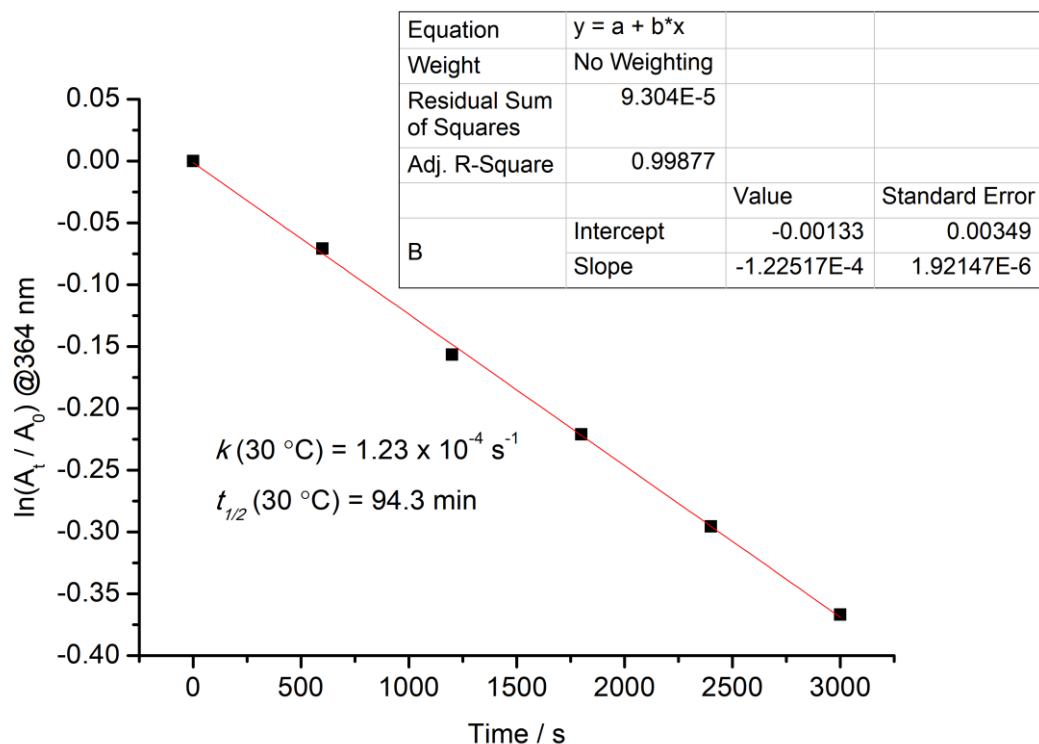


Figure 67: Graph showing the linear fit of the change in absorbance at 364 nm over time at 30 °C (PAT 1). Rate constant k (= slope) and calculated $t_{1/2}$ are mentioned.

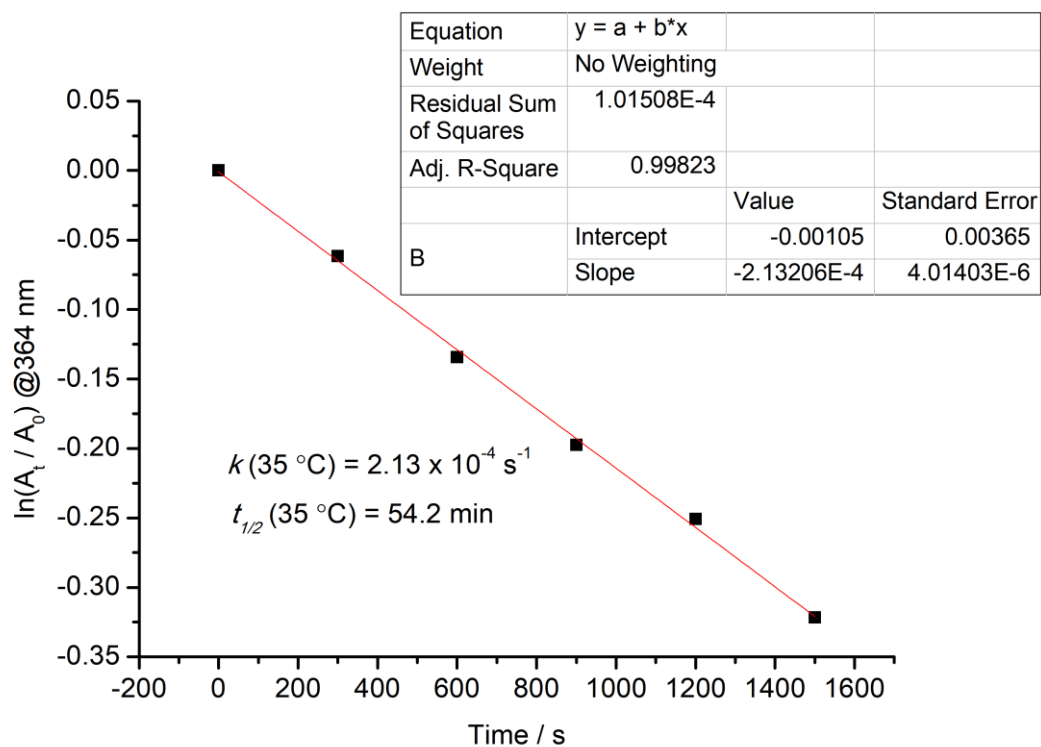


Figure 68: Graph showing the linear fit of the change in absorbance at 364 nm over time at 35 °C (PAT 1). Rate constant k (= slope) and calculated $t_{1/2}$ are mentioned.

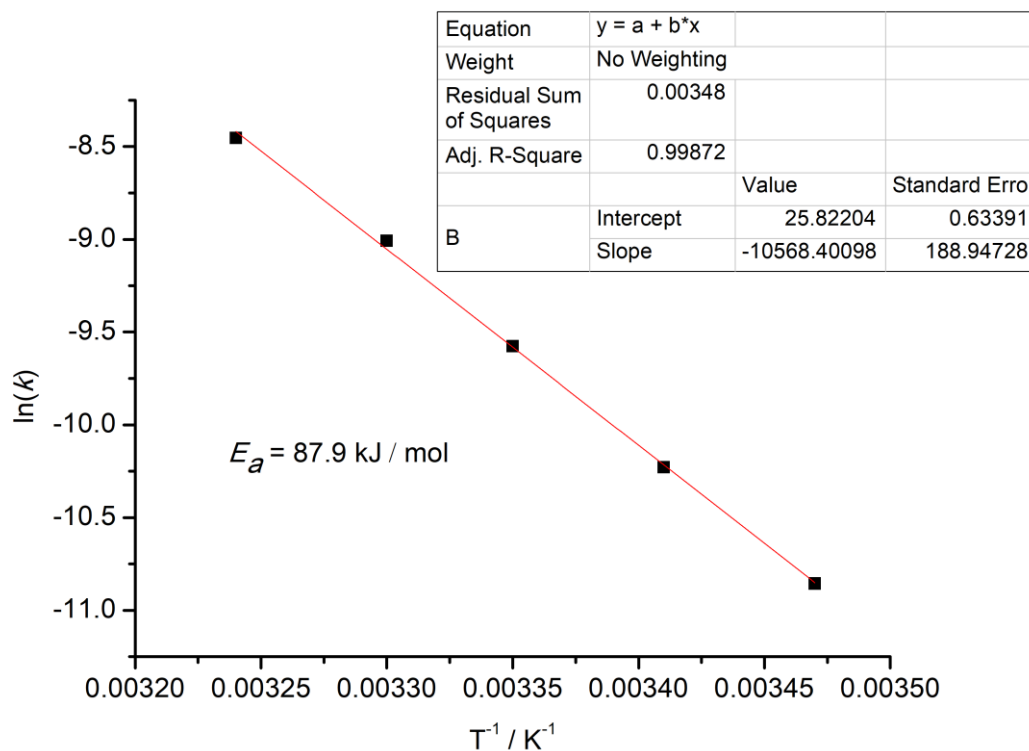


Figure 69: Arrhenius plot of PAT 1. Calculated activation energy (E_a) is mentioned.

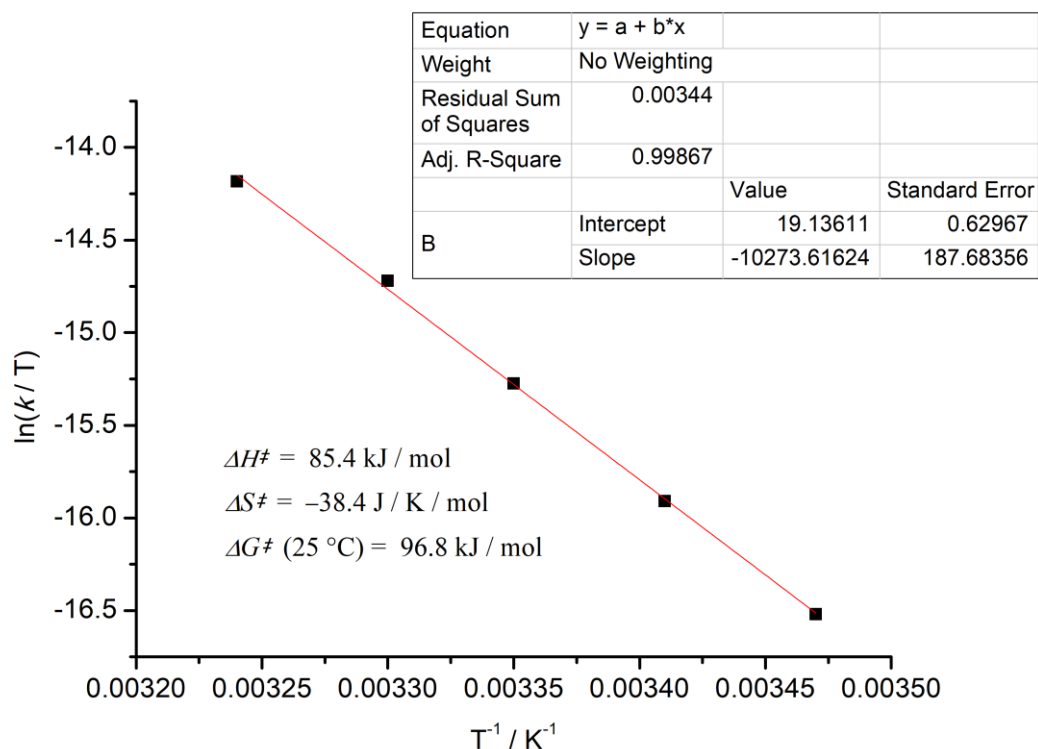


Figure 70: Eyring plot of **PAT 1**. Calculated entropy of activation (ΔS^\ddagger), enthalpy of activation (ΔH^\ddagger) and Gibbs free energy (ΔG^\ddagger) are mentioned.

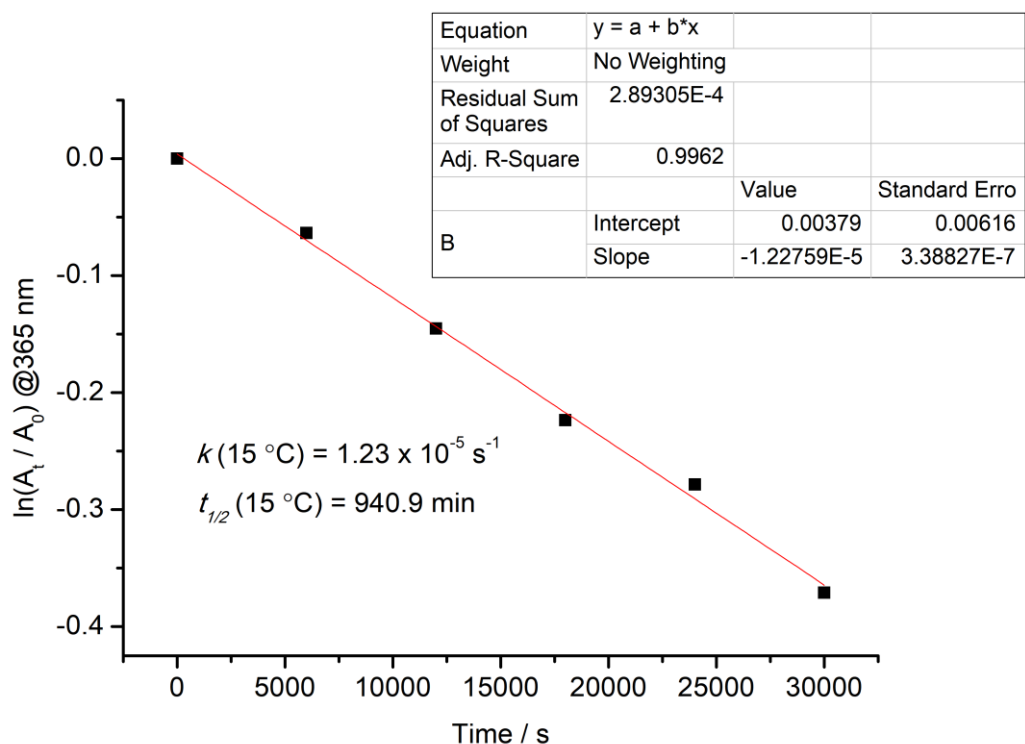


Figure 71: Graph showing the linear fit of the change in absorbance at 364 nm over time at 15 °C (**PAT 2**). Rate constant k (= slope) and calculated $t_{1/2}$ are mentioned.

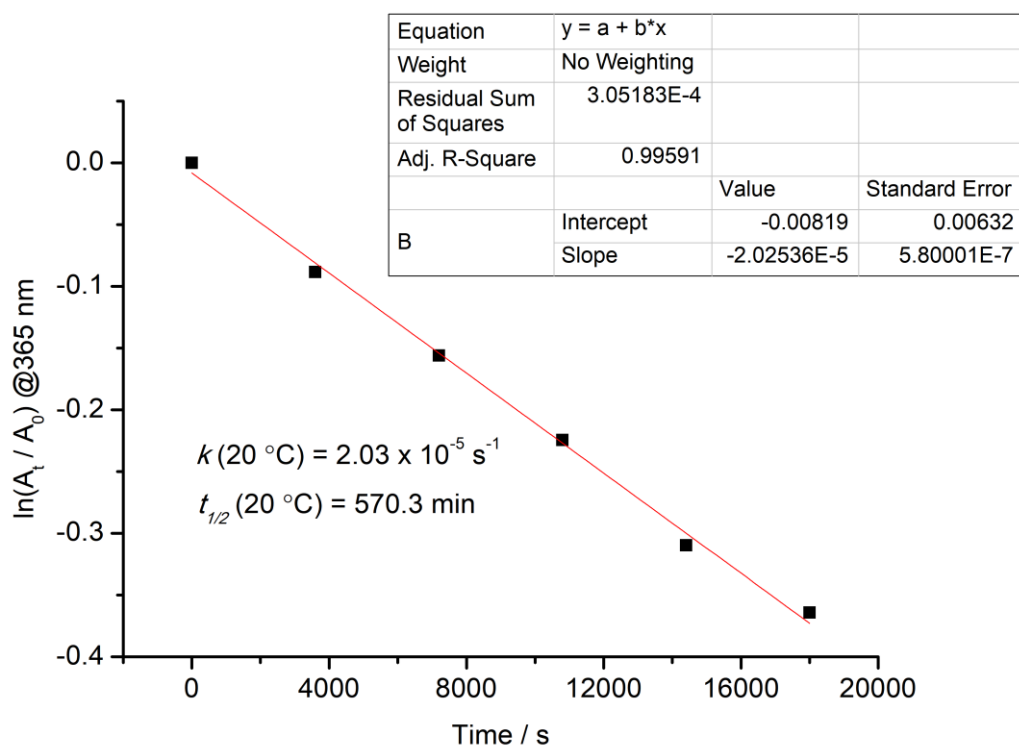


Figure 72: Graph showing the linear fit of the change in absorbance at 364 nm over time at 20 °C (PAT 2). Rate constant k (= slope) and calculated $t_{1/2}$ are mentioned.

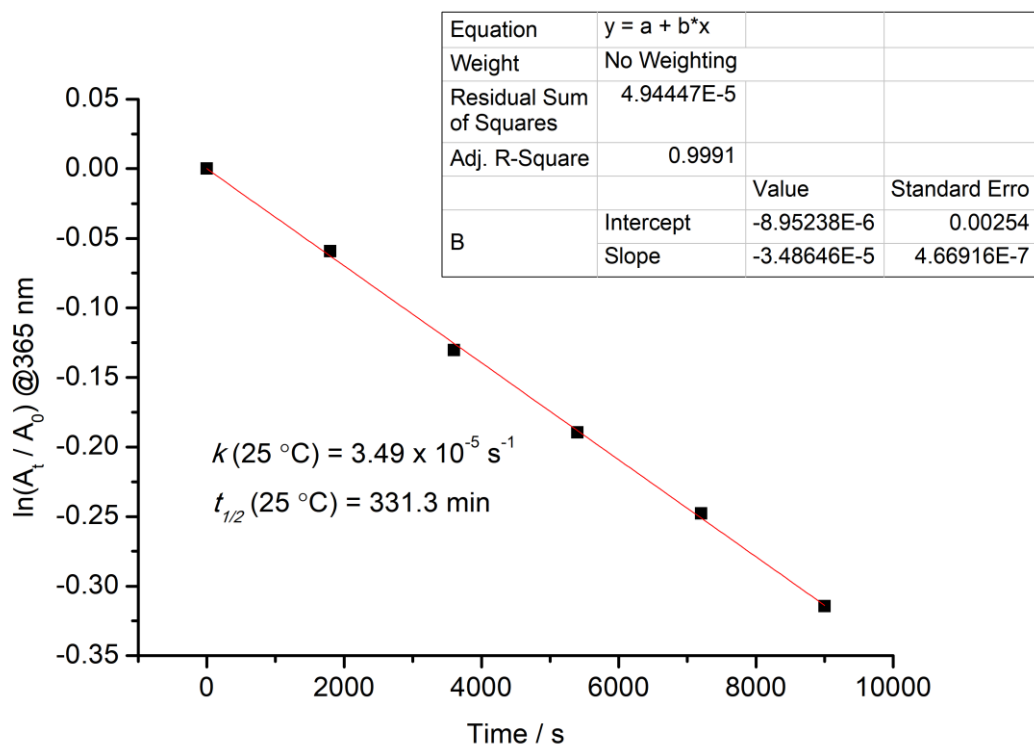


Figure 73: Graph showing the linear fit of the change in absorbance at 364 nm over time at 25 °C (PAT 2). Rate constant k (= slope) and calculated $t_{1/2}$ are mentioned.

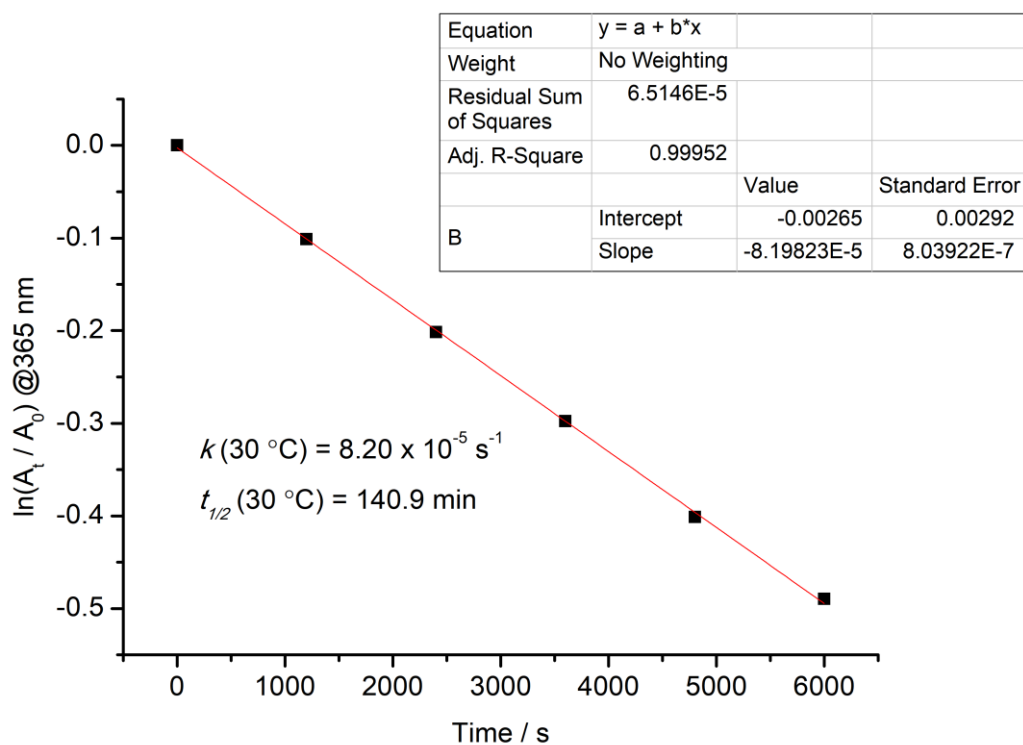


Figure 74: Graph showing the linear fit of the change in absorbance at 364 nm over time at 30 °C (PAT 2). Rate constant k (= slope) and calculated $t_{1/2}$ are mentioned.

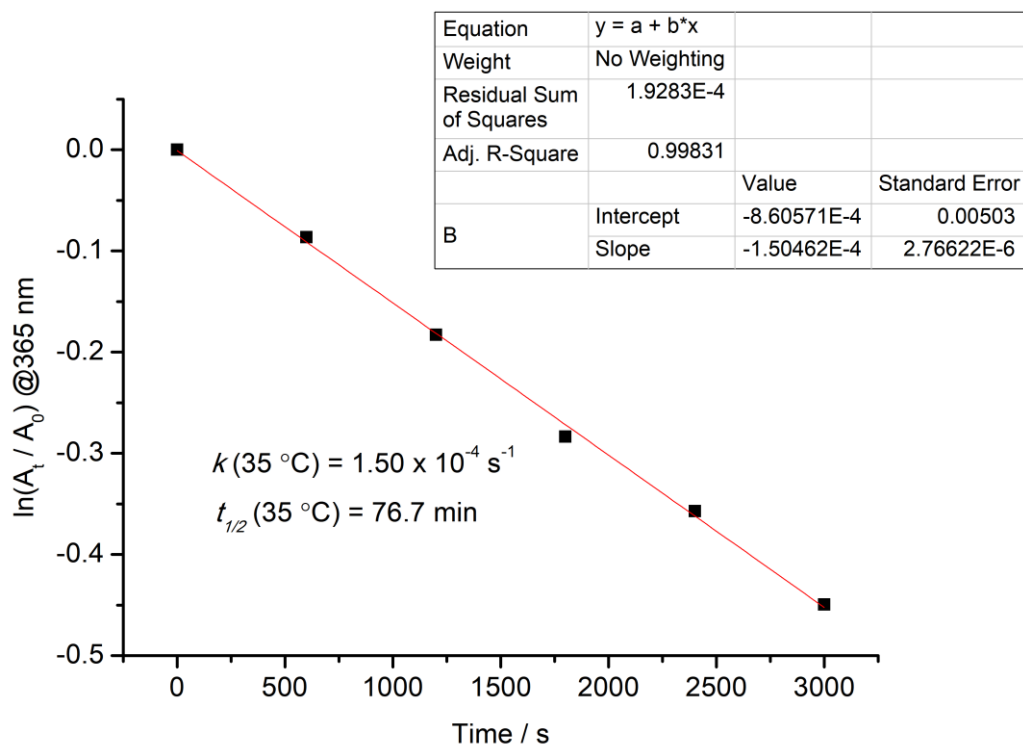


Figure 75: Graph showing the linear fit of the change in absorbance at 364 nm over time at 35 °C (PAT 2). Rate constant k (= slope) and calculated $t_{1/2}$ are mentioned.

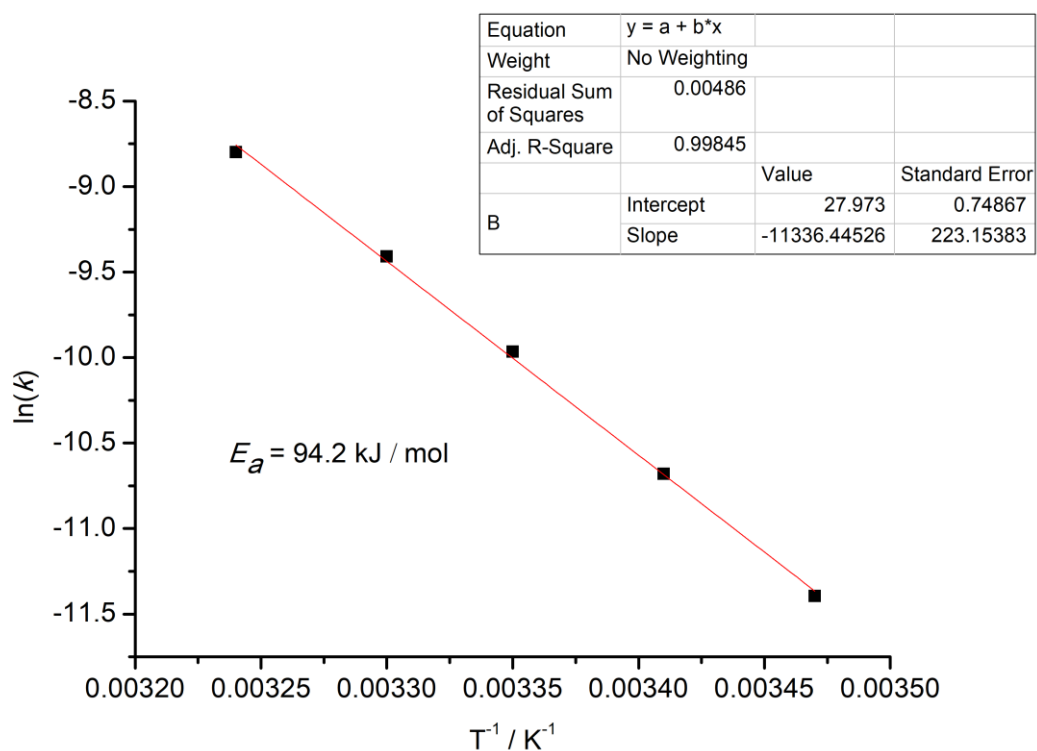


Figure 76: Arrhenius plot of PAT 2. Calculated activation energy (E_a) is mentioned.

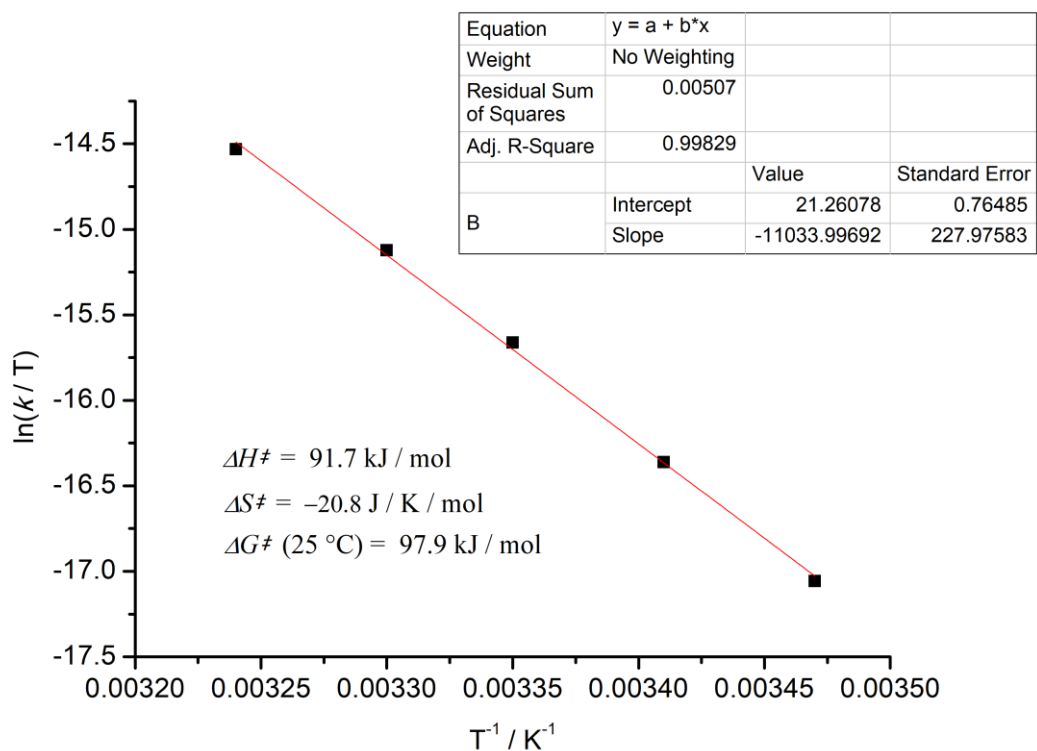


Figure 77: Eyring plot of PAT 2. Calculated entropy of activation (ΔS^\ddagger), enthalpy of activation (ΔH^\ddagger) and Gibbs free energy (ΔG^\ddagger) are mentioned.

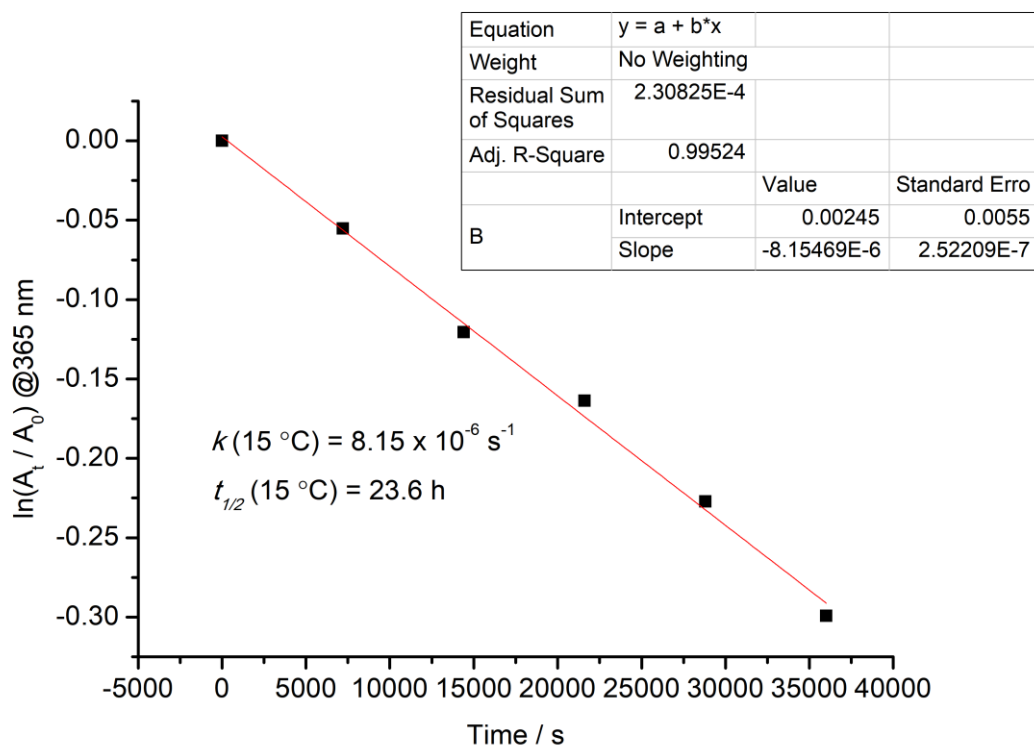


Figure 78: Graph showing the linear fit of the change in absorbance at 365 nm over time at 15 °C (PAT 3). Rate constant k (= slope) and calculated $t_{1/2}$ are mentioned.

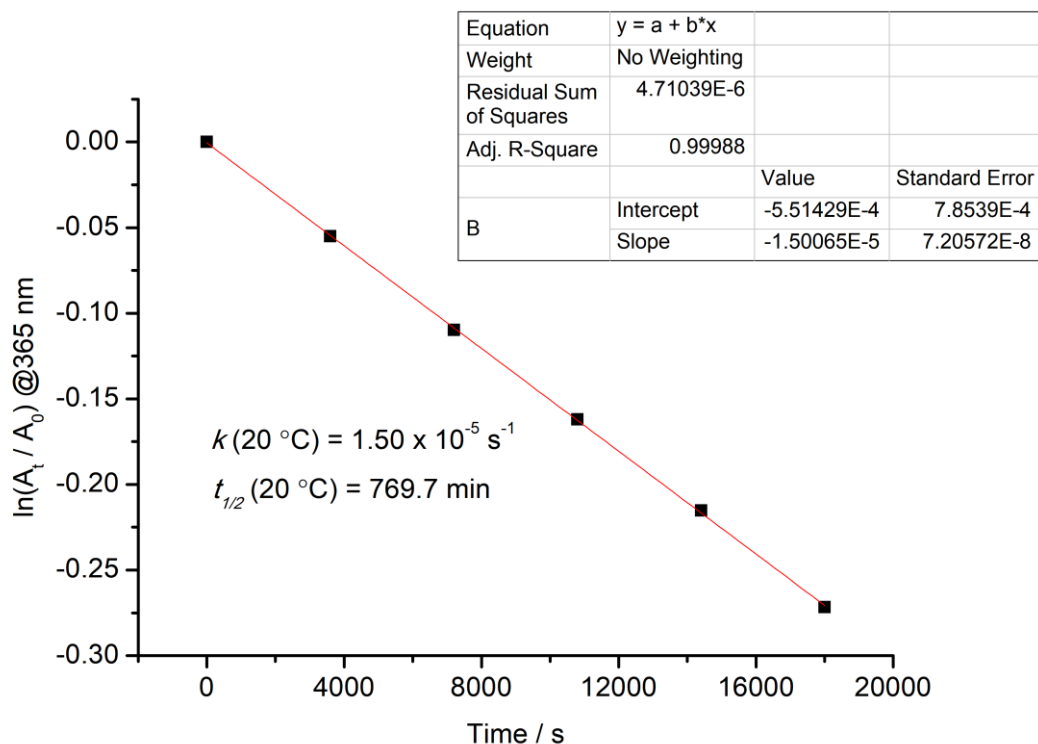


Figure 79: Graph showing the linear fit of the change in absorbance at 365 nm over time at 20 °C (PAT 3). Rate constant k (= slope) and calculated $t_{1/2}$ are mentioned.

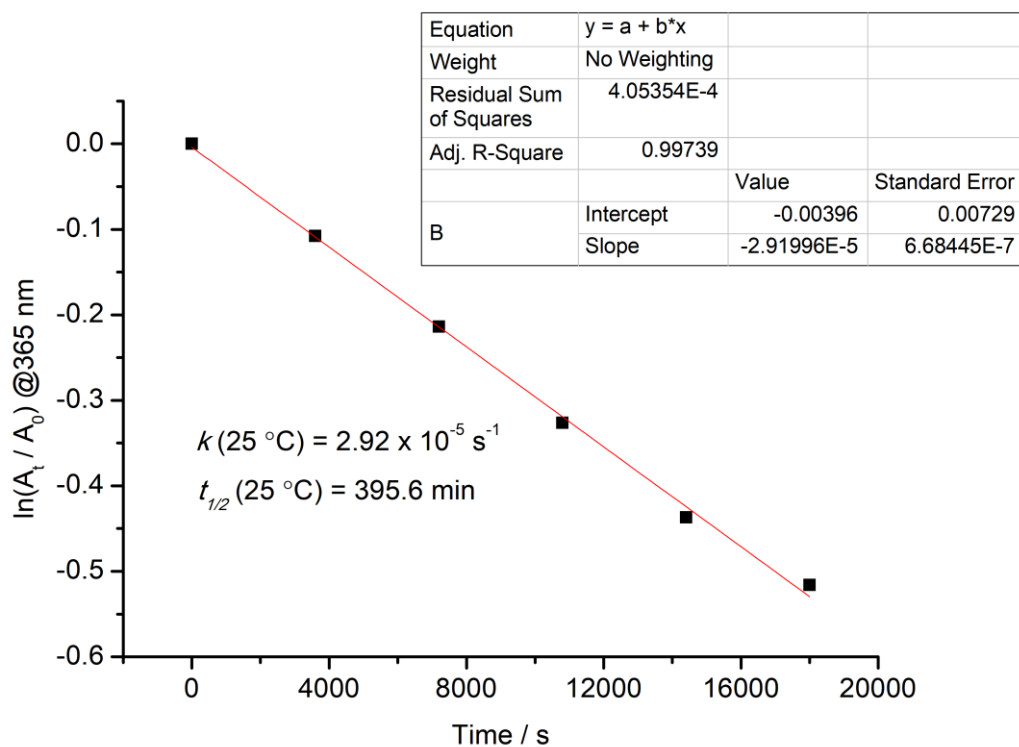


Figure 80: Graph showing the linear fit of the change in absorbance at 365 nm over time at 25 °C (PAT 3). Rate constant k (= slope) and calculated $t_{1/2}$ are mentioned.

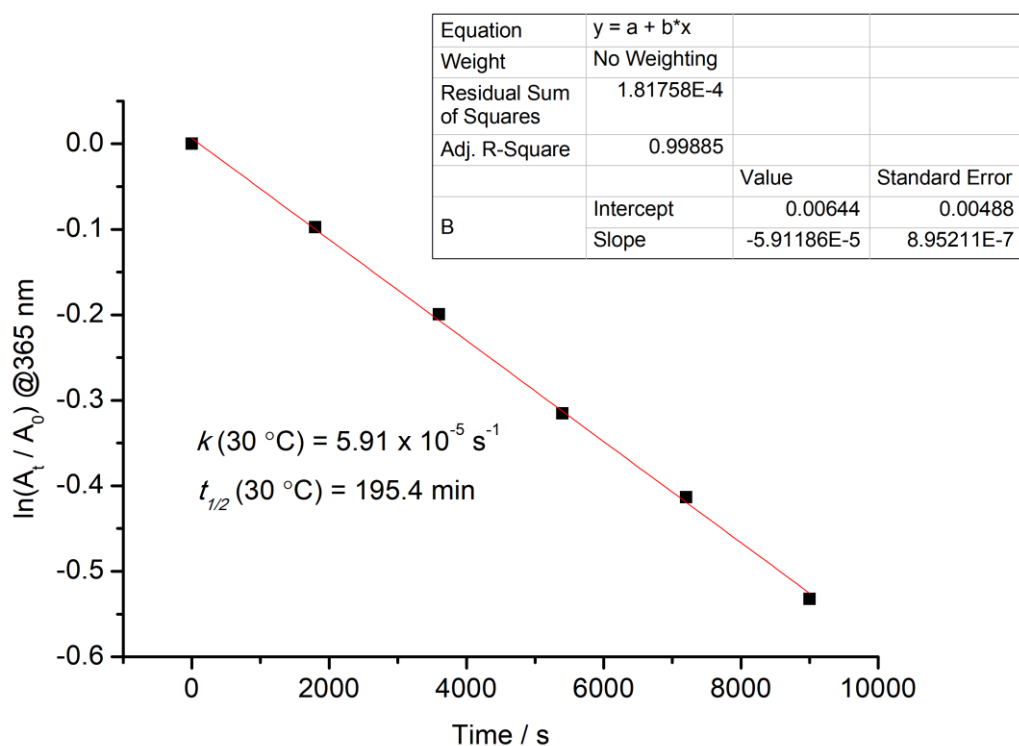


Figure 81: Graph showing the linear fit of the change in absorbance at 365 nm over time at 30 °C (PAT 3). Rate constant k (= slope) and calculated $t_{1/2}$ are mentioned.

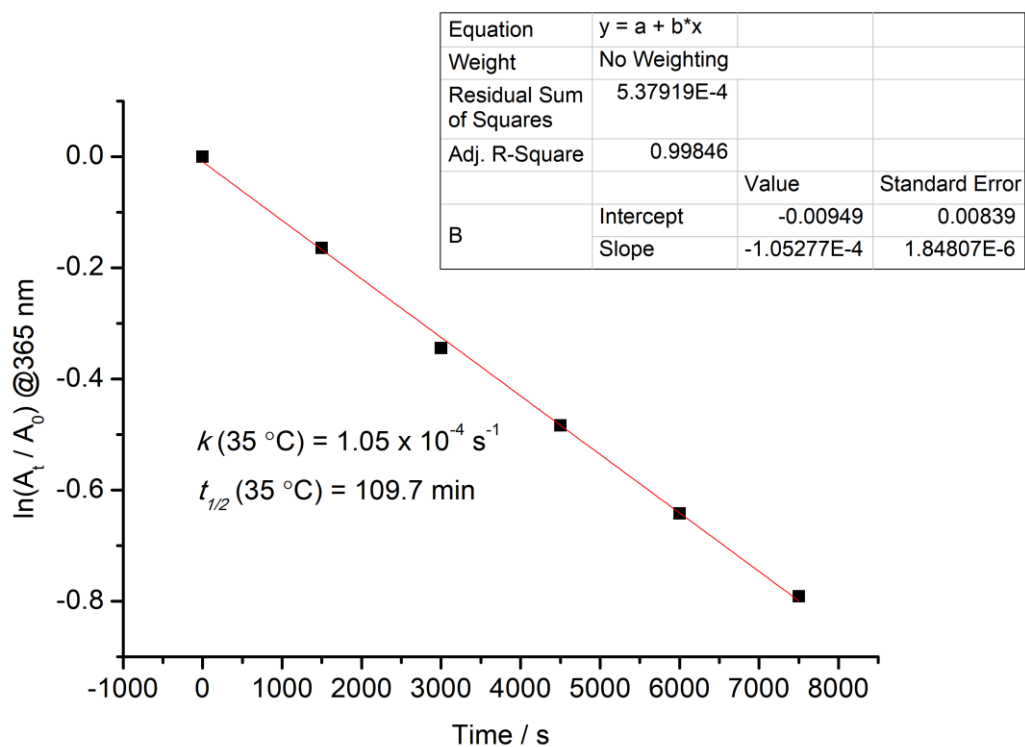


Figure 82: Graph showing the linear fit of the change in absorbance at 365 nm over time at 35 °C (PAT 3). Rate constant k (= slope) and calculated $t_{1/2}$ are mentioned.

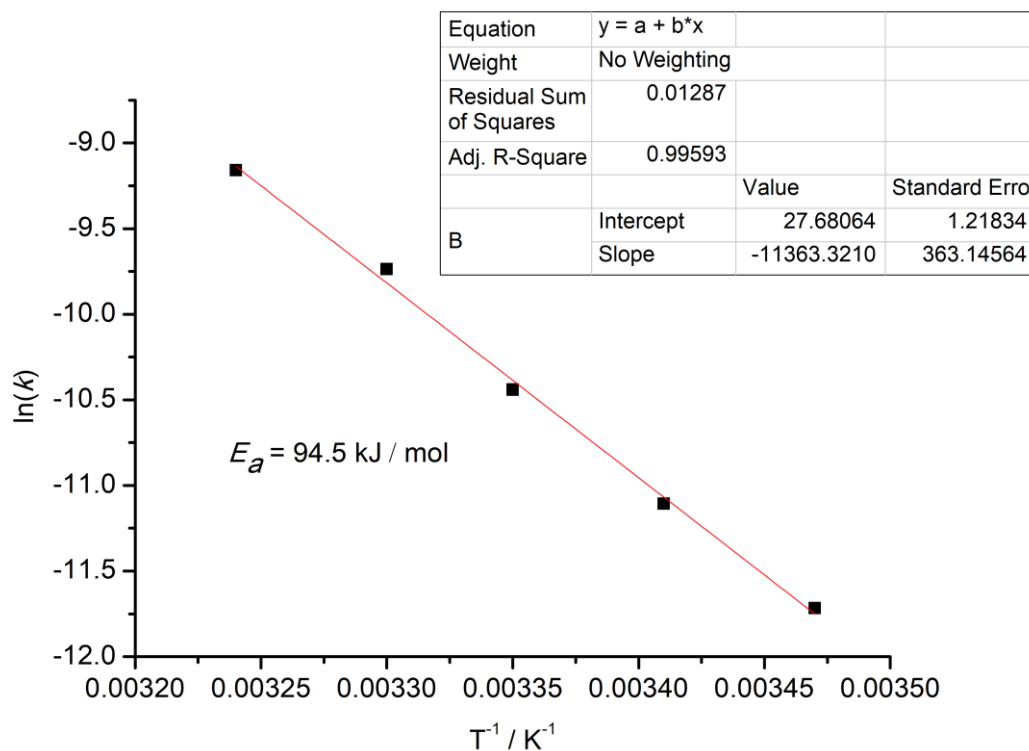


Figure 83: Arrhenius plot of PAT 3. Calculated activation energy (E_a) is mentioned.

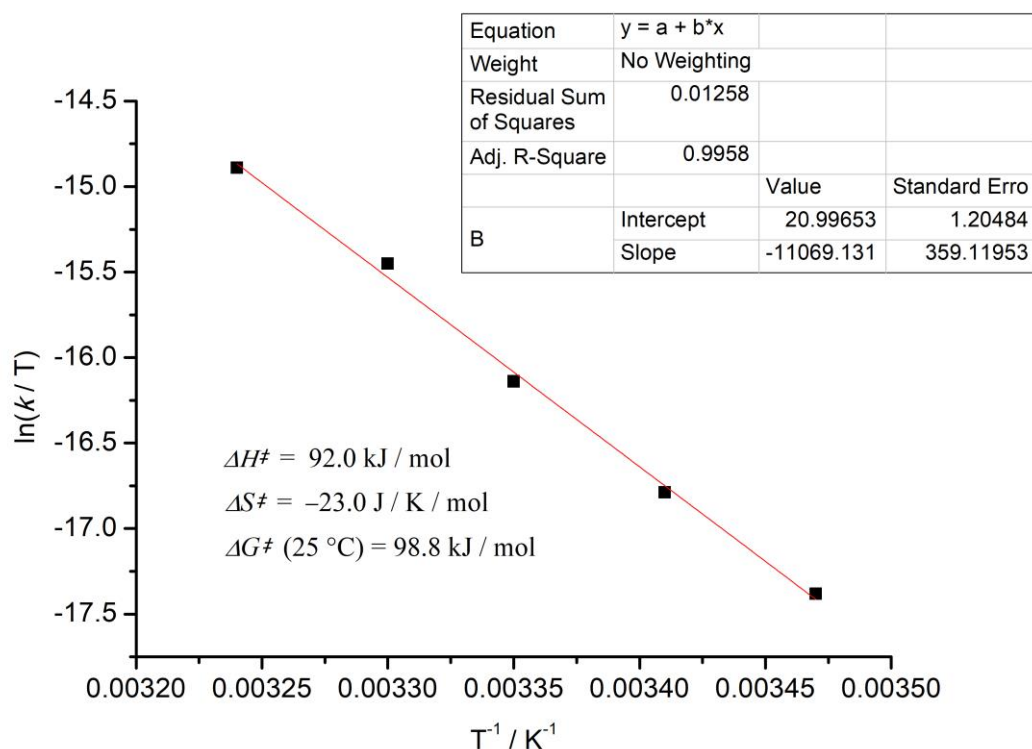


Figure 84: Eyring plot of **PAT 3**. Calculated entropy of activation (ΔS^\ddagger), enthalpy of activation (ΔH^\ddagger) and Gibbs free energy (ΔG^\ddagger) are mentioned.

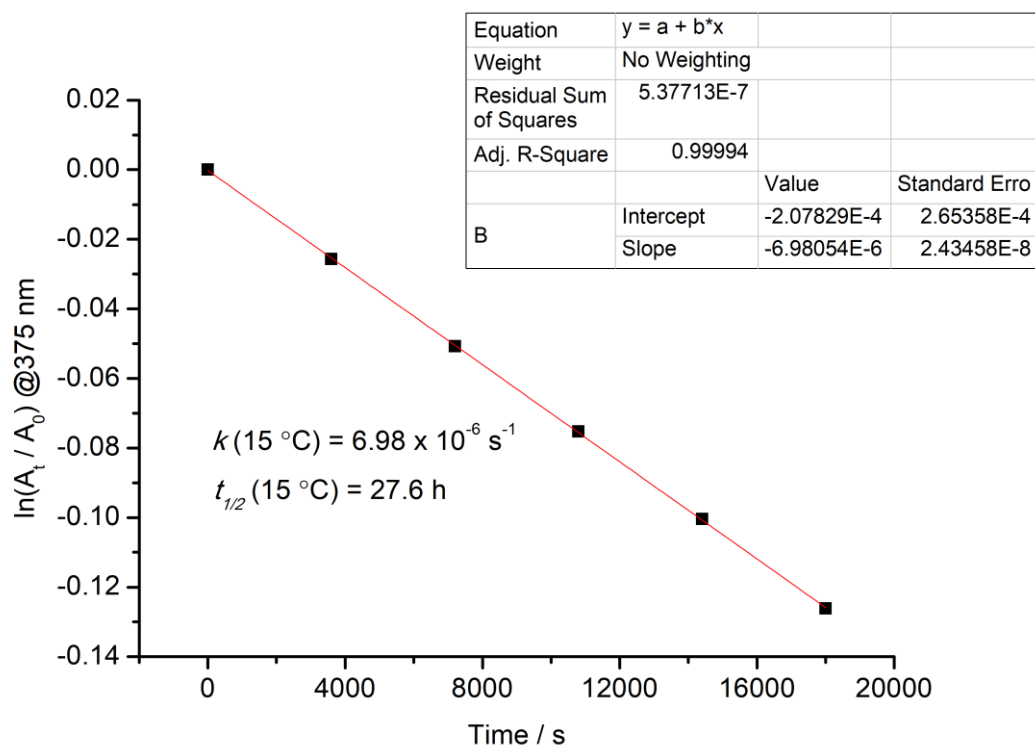


Figure 85: Graph showing the linear fit of the change in absorbance at 375 nm over time at 15 °C (**PAT 4**). Rate constant k (= slope) and calculated $t_{1/2}$ are mentioned.

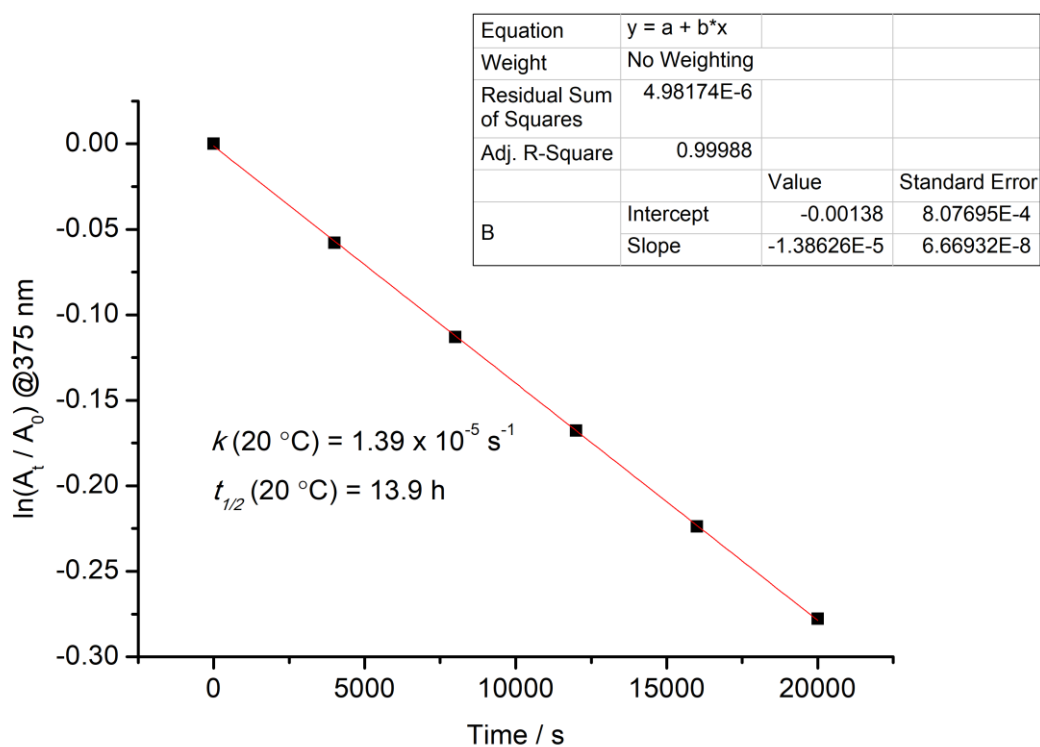


Figure 86: Graph showing the linear fit of the change in absorbance at 375 nm over time at 20 °C (PAT 4). Rate constant k (= slope) and calculated $t_{1/2}$ are mentioned.

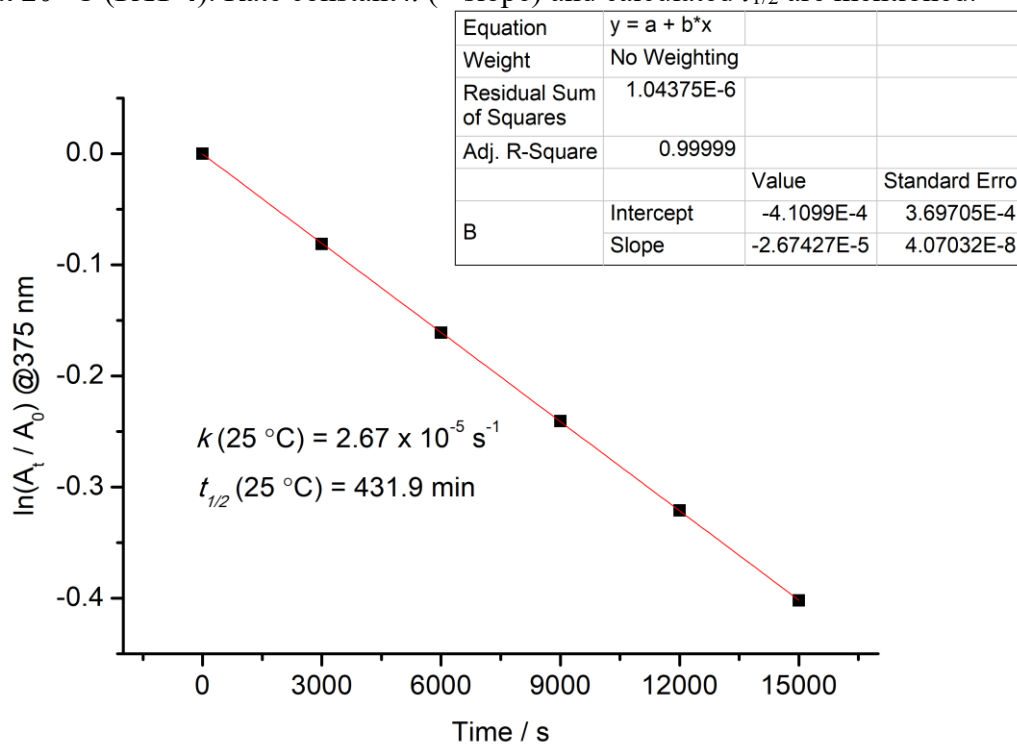


Figure 87: Graph showing the linear fit of the change in absorbance at 375 nm over time at 25 °C (PAT 4). Rate constant k (= slope) and calculated $t_{1/2}$ are mentioned.

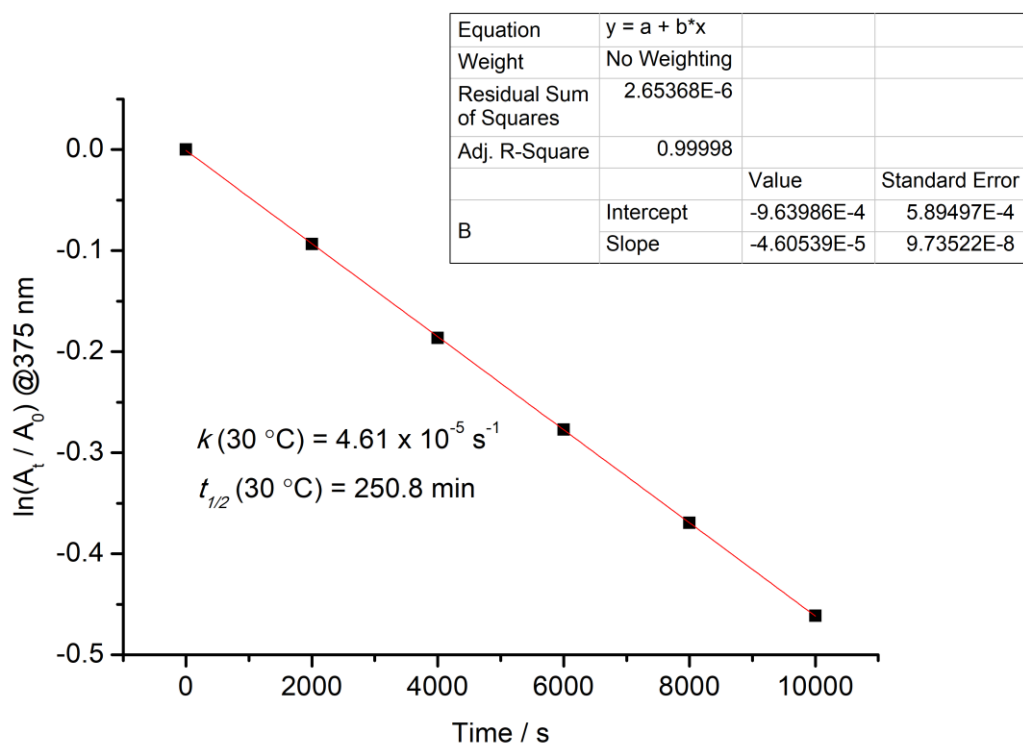


Figure 88: Graph showing the linear fit of the change in absorbance at 375 nm over time at 30 °C (PAT 4). Rate constant k (= slope) and calculated $t_{1/2}$ are mentioned.

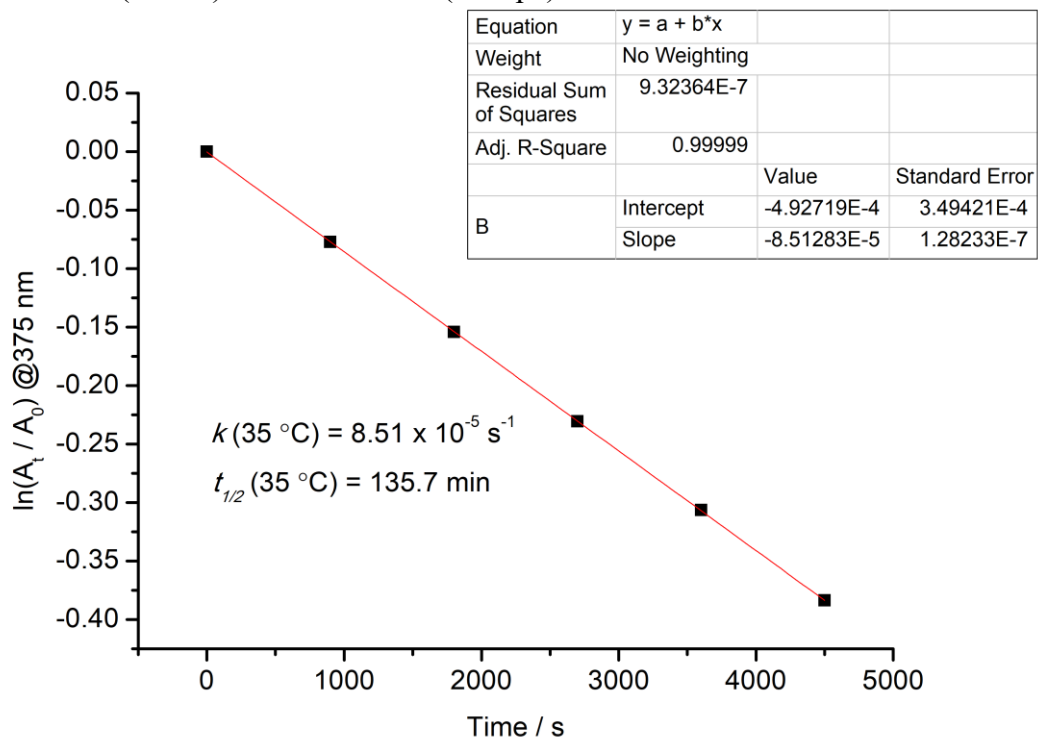


Figure 89: Graph showing the linear fit of the change in absorbance at 375 nm over time at 35 °C (PAT 4). Rate constant k (= slope) and calculated $t_{1/2}$ are mentioned.

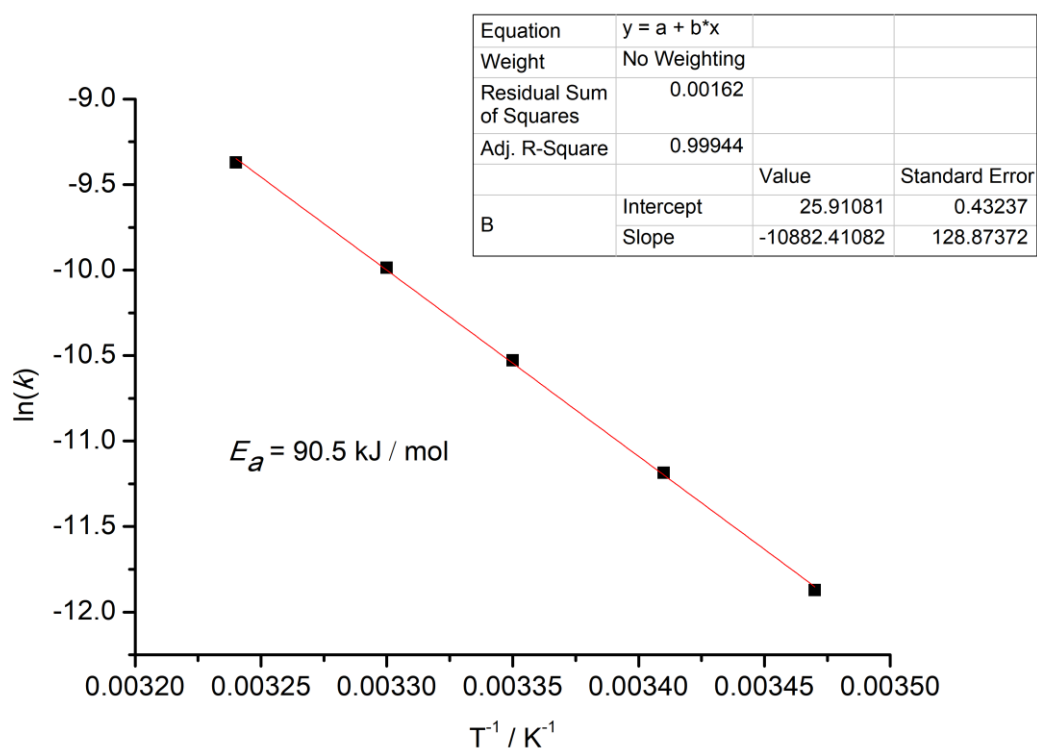


Figure 90: Arrhenius plot of PAT 4. Calculated activation energy (E_a) is mentioned.

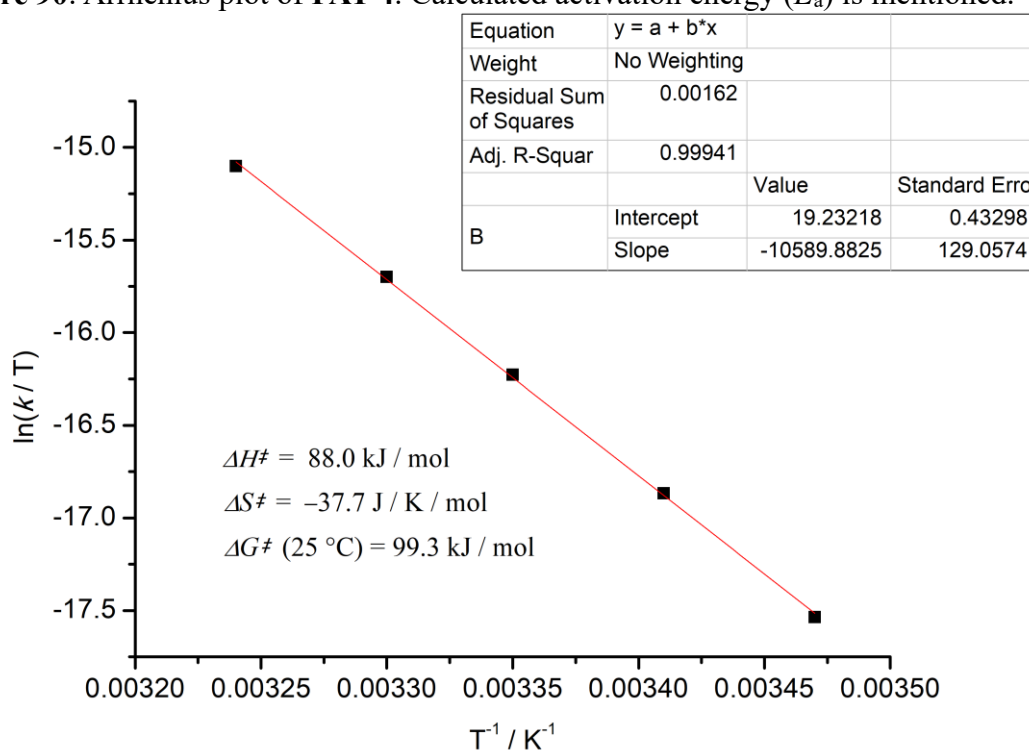


Figure 91: Eyring plot of PAT 4. Calculated entropy of activation (ΔS^\ddagger), enthalpy of activation (ΔH^\ddagger) and Gibbs free energy (ΔG^\ddagger) are mentioned.

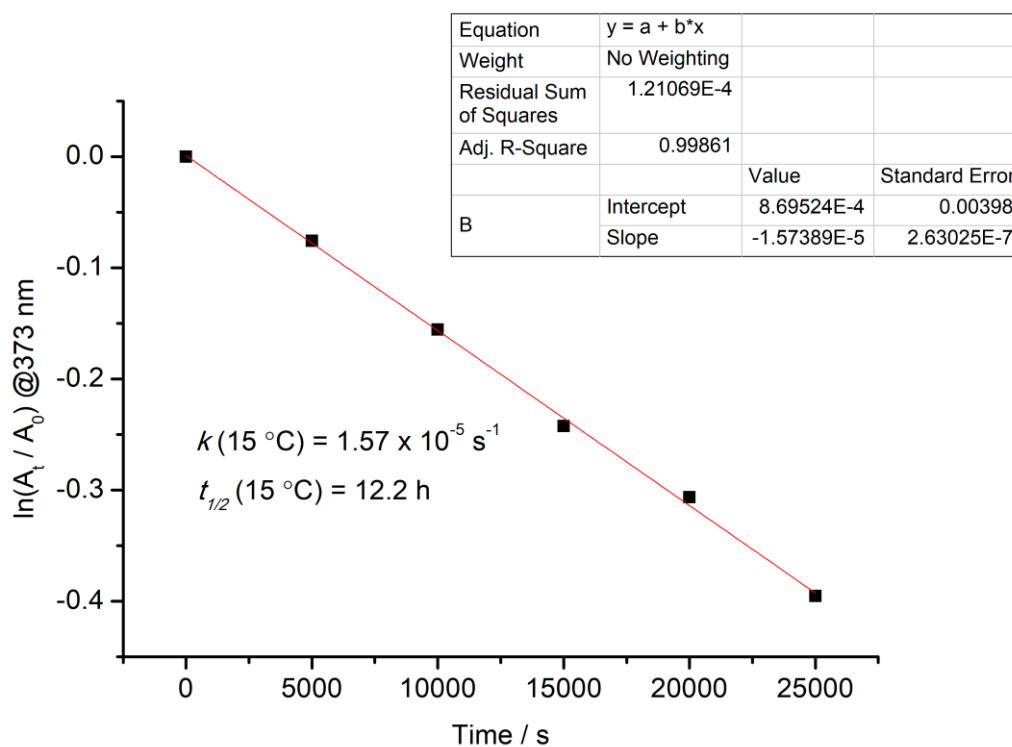


Figure 92: Graph showing the linear fit of the change in absorbance at 373 nm over time at 15 °C (PAT 5). Rate constant k (= slope) and calculated $t_{1/2}$ are mentioned.

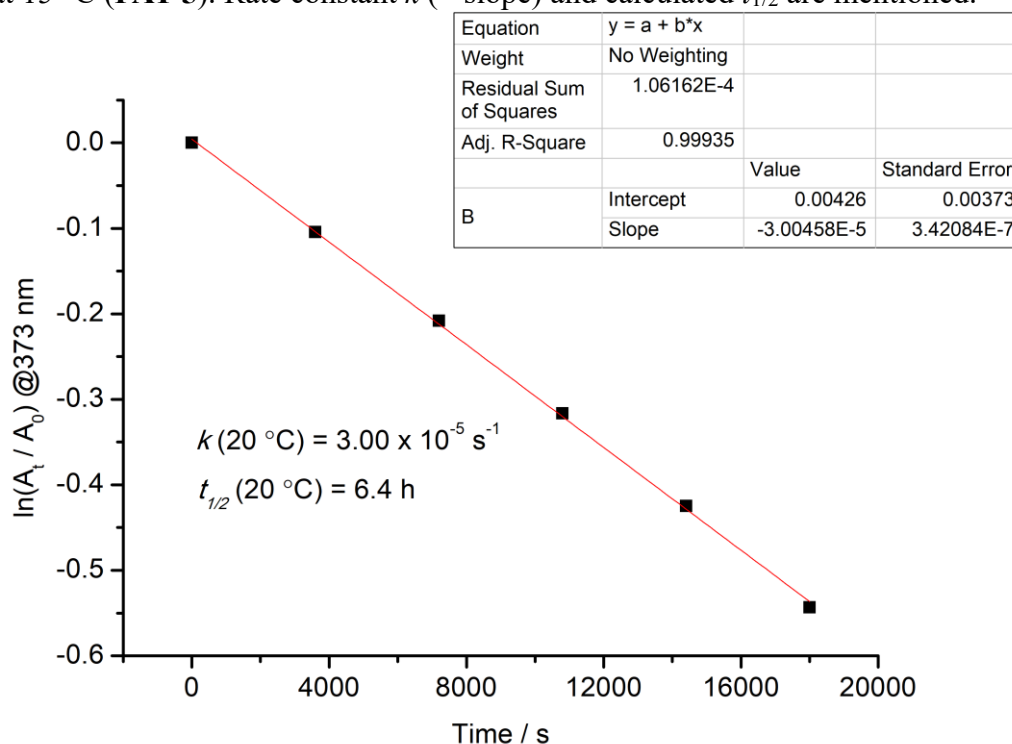


Figure 93: Graph showing the linear fit of the change in absorbance at 373 nm over time at 20 °C (PAT 5). Rate constant k (= slope) and calculated $t_{1/2}$ are mentioned.

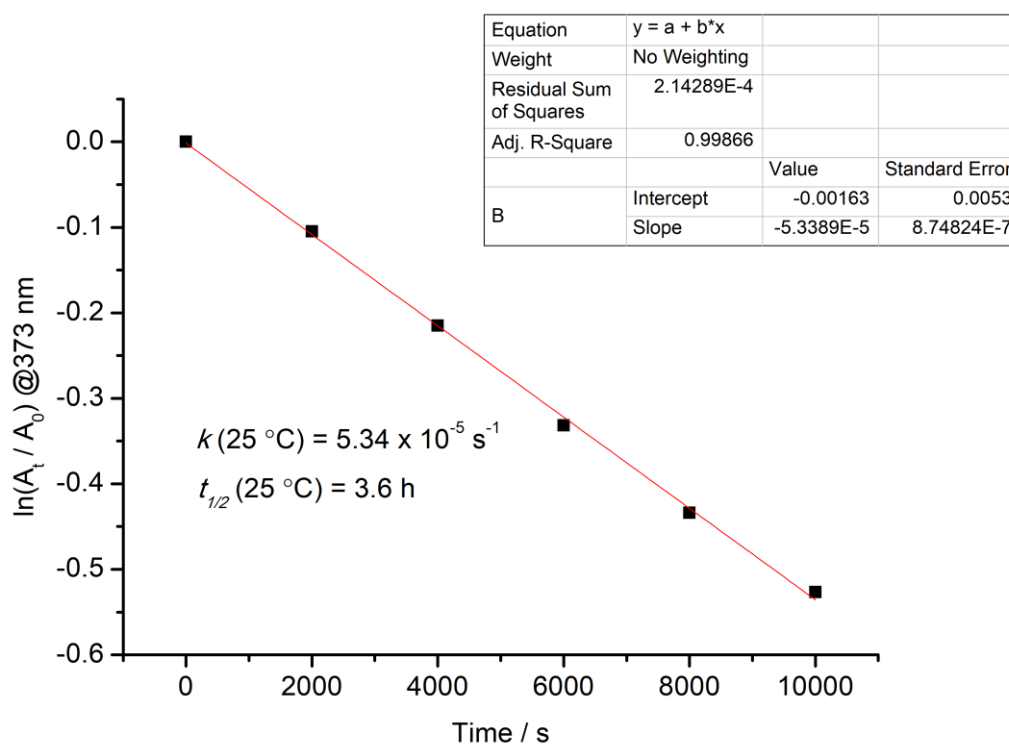


Figure 94: Graph showing the linear fit of the change in absorbance at 373 nm over time at 25 °C (PAT 5). Rate constant k (= slope) and calculated $t_{1/2}$ are mentioned.

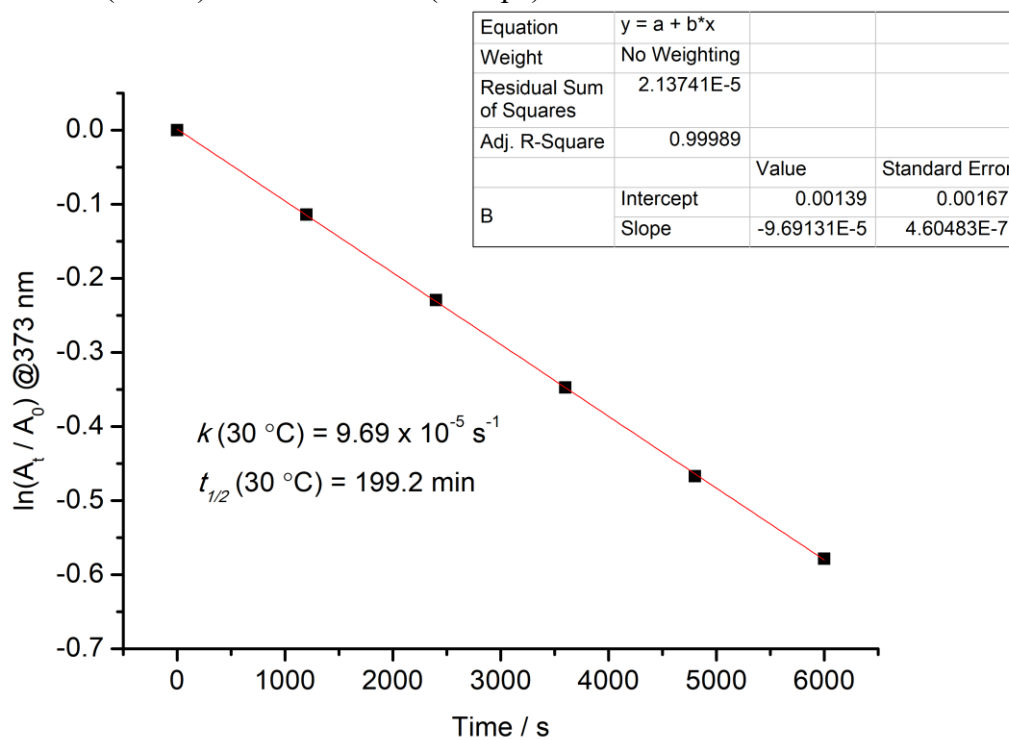


Figure 95: Graph showing the linear fit of the change in absorbance at 373 nm over time at 30 °C (PAT 5). Rate constant k (= slope) and calculated $t_{1/2}$ are mentioned.

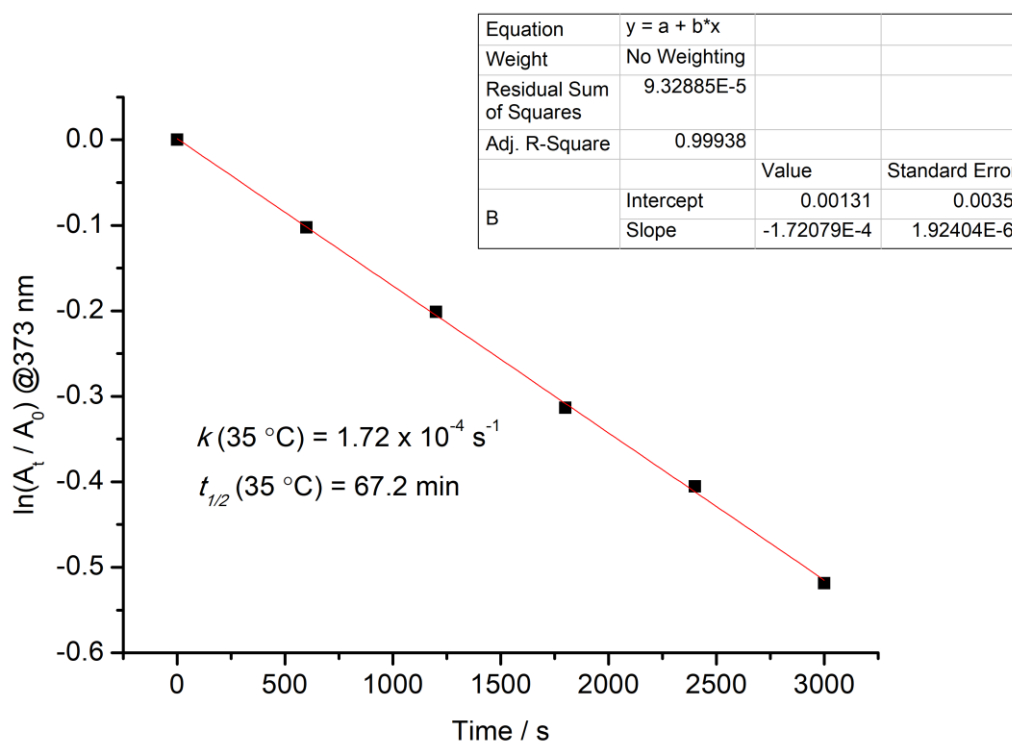


Figure 96: Graph showing the linear fit of the change in absorbance at 373 nm over time at 35 °C (PAT 5). Rate constant k (= slope) and calculated $t_{1/2}$ are mentioned.

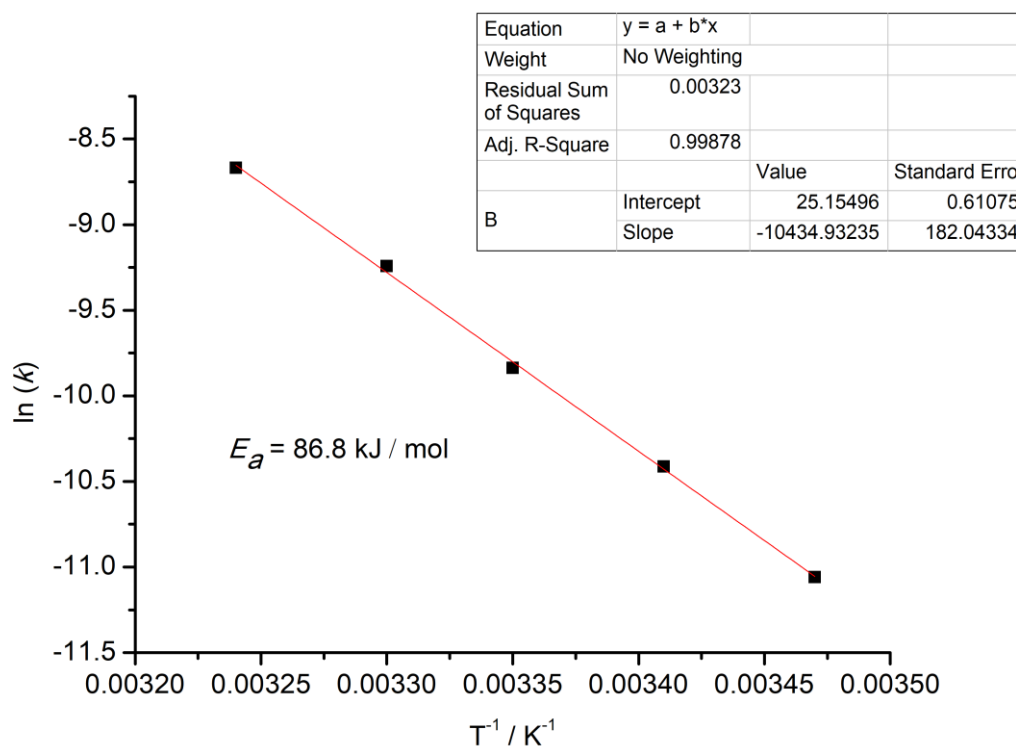


Figure 97: Arrhenius plot of PAT 5. Calculated activation energy (E_a) is mentioned.

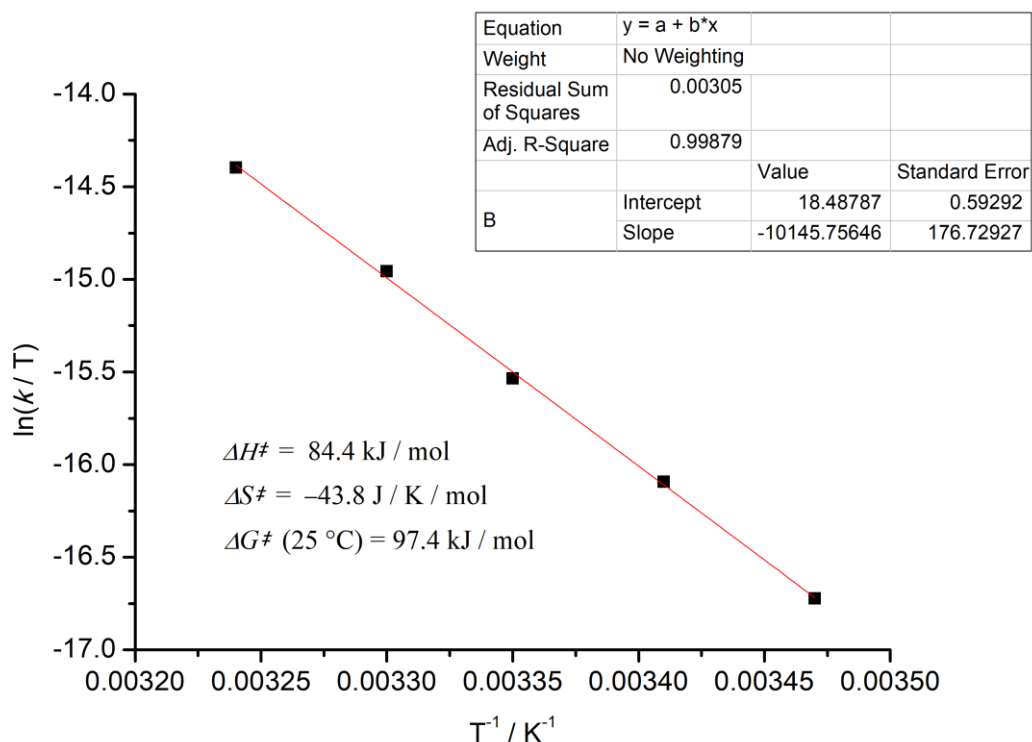


Figure 98: Eyring plot of **PAT 5**. Calculated entropy of activation (ΔS^\ddagger), enthalpy of activation (ΔH^\ddagger) and Gibbs free energy (ΔG^\ddagger) are mentioned.

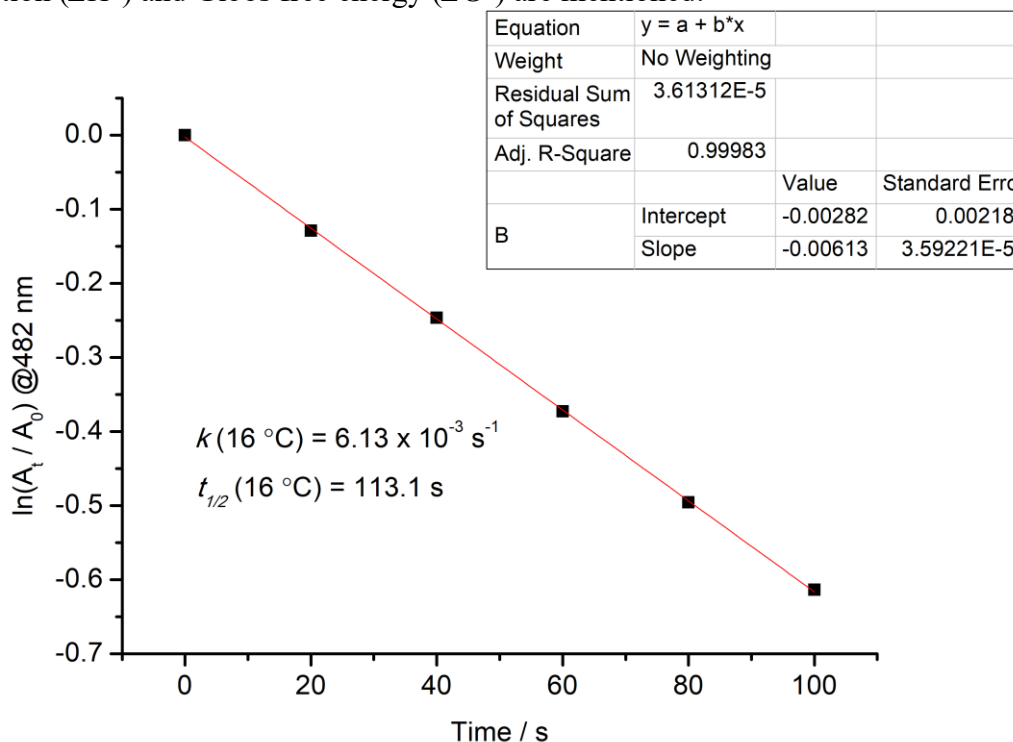


Figure 99: Graph showing the linear fit of the change in absorbance at 482 nm over time at 16 °C (**PAT 6**). Rate constant k (= slope) and calculated $t_{1/2}$ are mentioned.

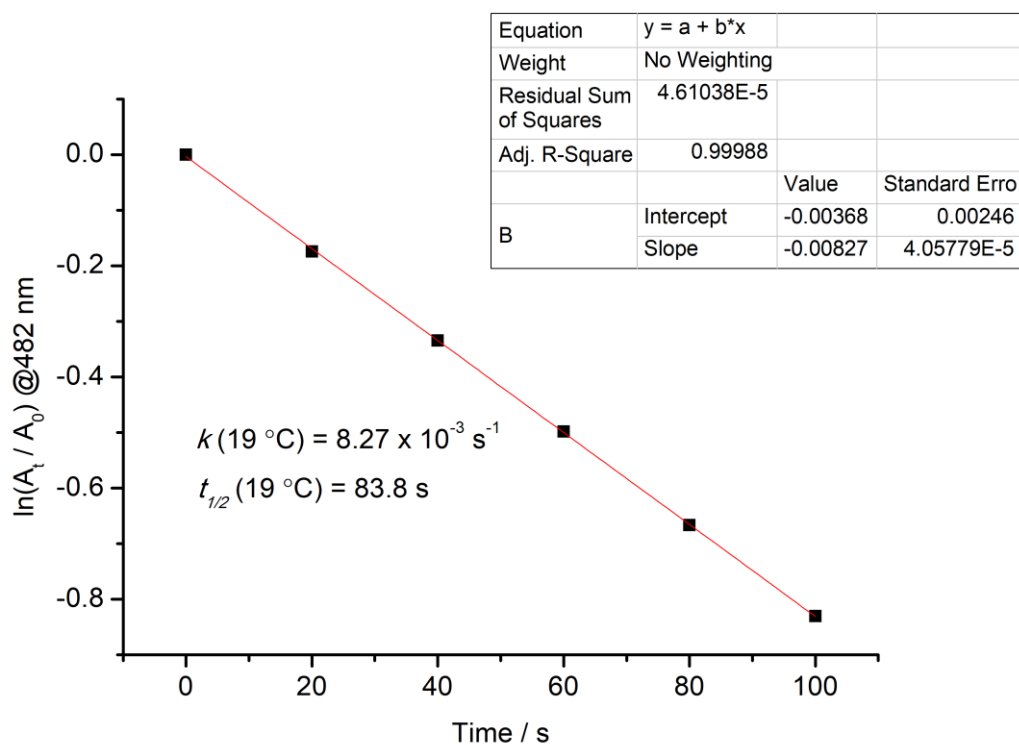


Figure 100: Graph showing the linear fit of the change in absorbance at 482 nm over time at 19 °C (PAT 6). Rate constant k (= slope) and calculated $t_{1/2}$ are mentioned.

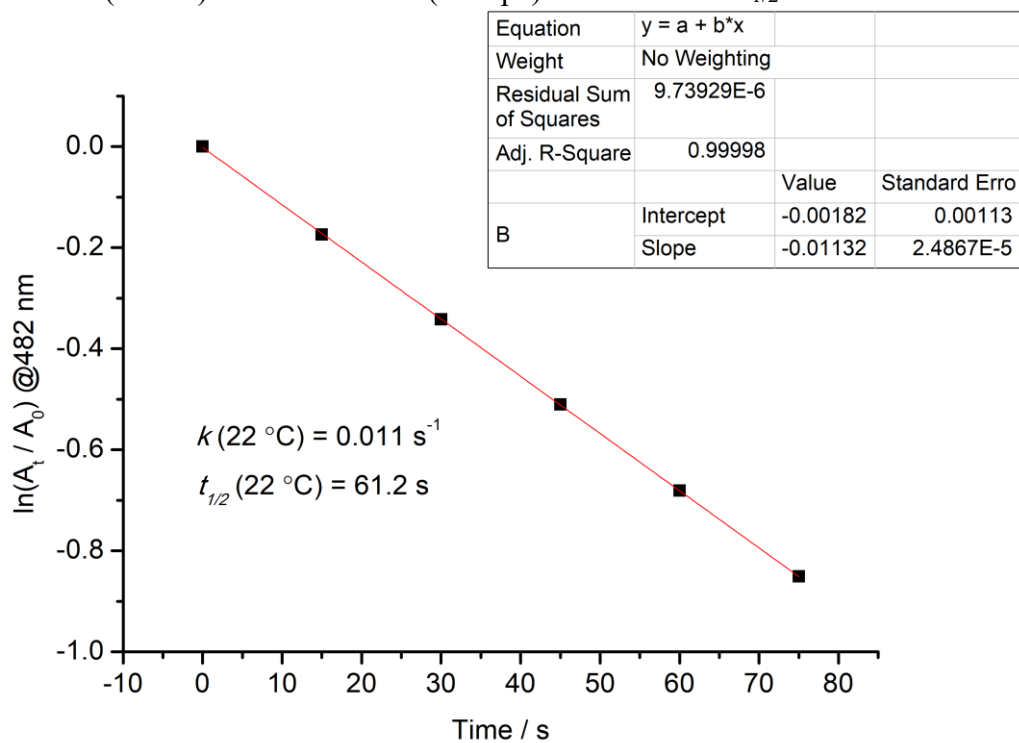


Figure 101: Graph showing the linear fit of the change in absorbance at 482 nm over time at 22 °C (PAT 6). Rate constant k (= slope) and calculated $t_{1/2}$ are mentioned.

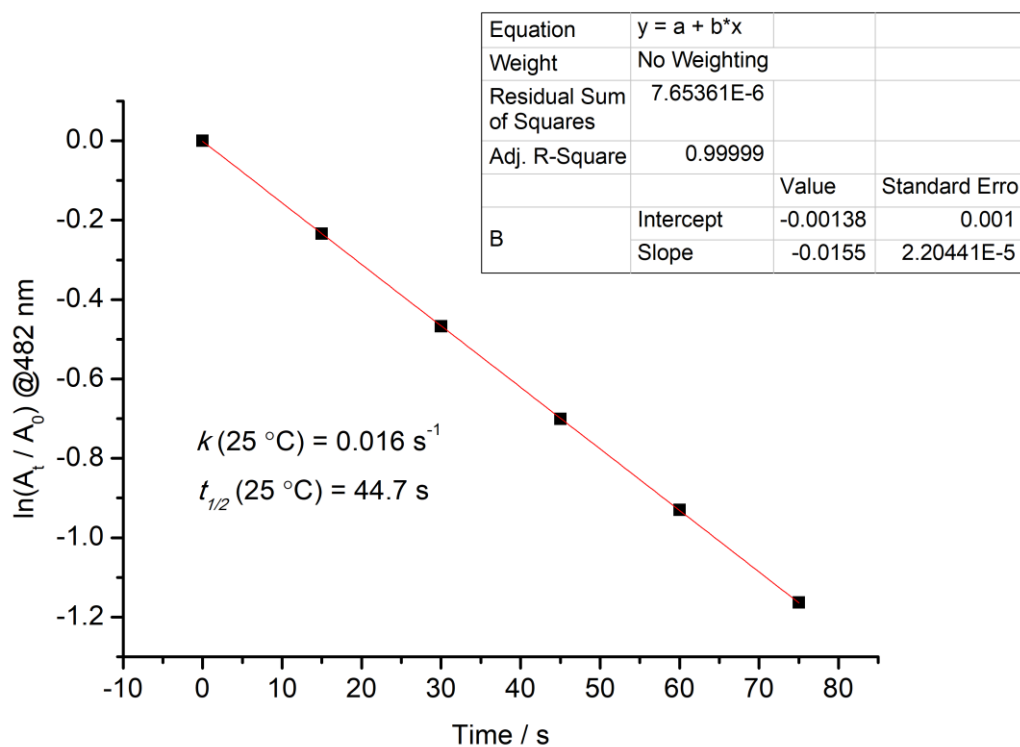


Figure 102: Graph showing the linear fit of the change in absorbance at 482 nm over time at 25 °C (PAT 6). Rate constant k (= slope) and calculated $t_{1/2}$ are mentioned.

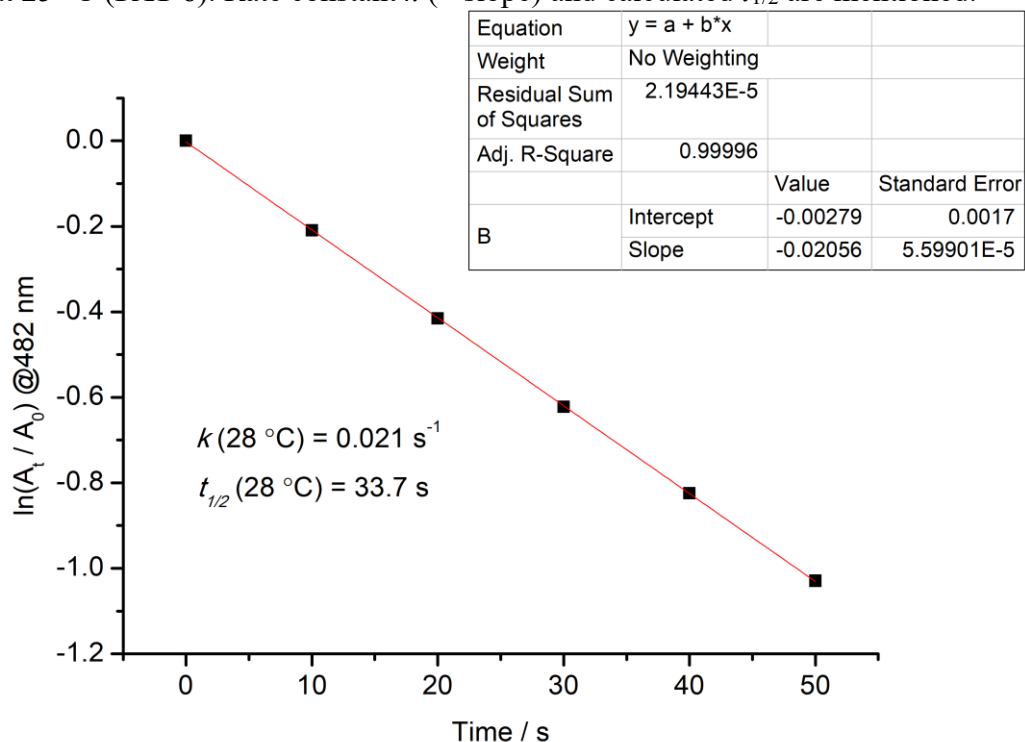


Figure 103: Graph showing the linear fit of the change in absorbance at 482 nm over time at 28 °C (PAT 6). Rate constant k (= slope) and calculated $t_{1/2}$ are mentioned.

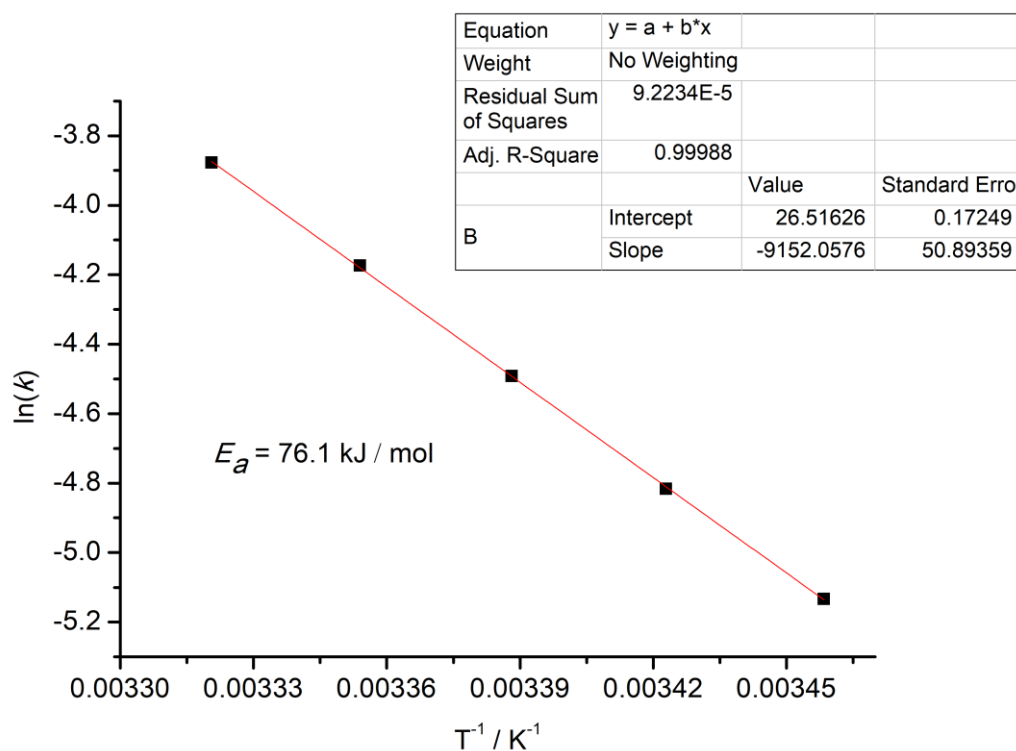


Figure 104: Arrhenius plot of PAT 6. Calculated activation energy (E_a) is mentioned.

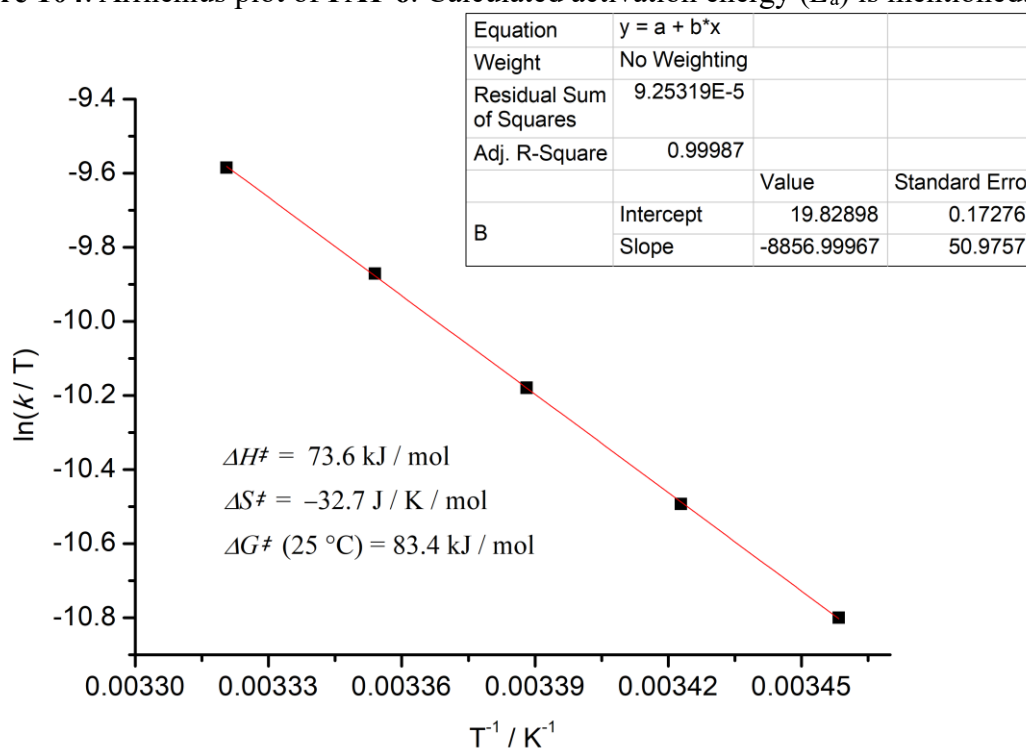


Figure 105: Eyring plot of PAT 6. Calculated entropy of activation (ΔS^\ddagger), enthalpy of activation (ΔH^\ddagger) and Gibbs free energy (ΔG^\ddagger) are mentioned.

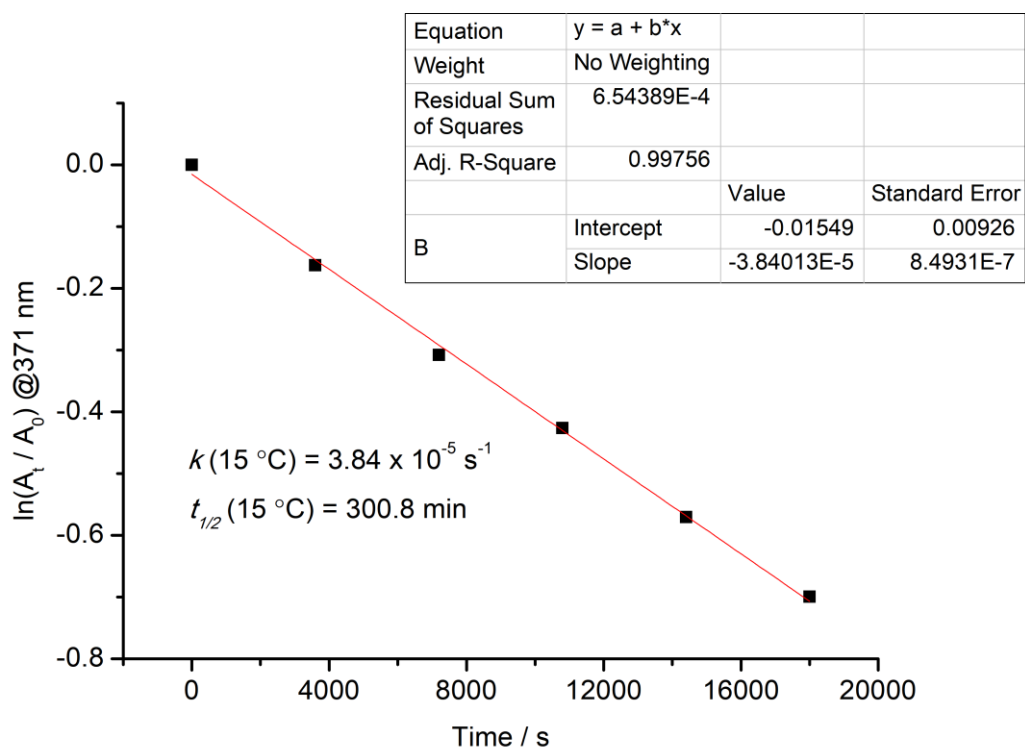


Figure 106: Graph showing the linear fit of the change in absorbance at 371 nm over time at 15 °C (PAT 9). Rate constant k (= slope) and calculated $t_{1/2}$ are mentioned.

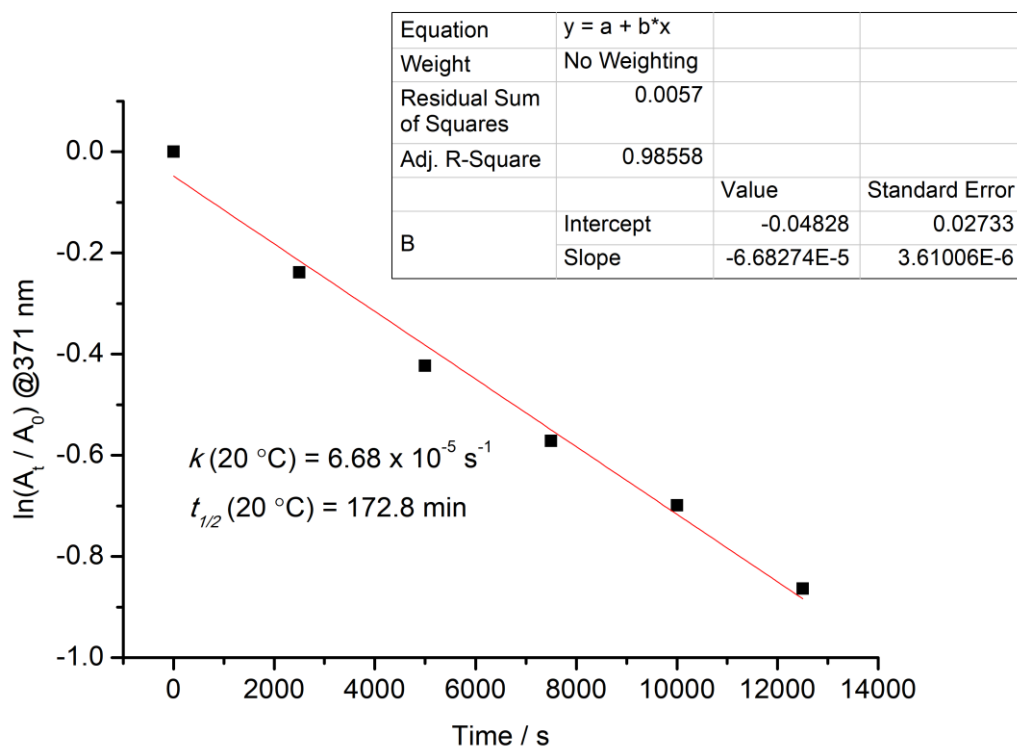


Figure 107: Graph showing the linear fit of the change in absorbance at 371 nm over time at 20 °C (PAT 9). Rate constant k (= slope) and calculated $t_{1/2}$ are mentioned.

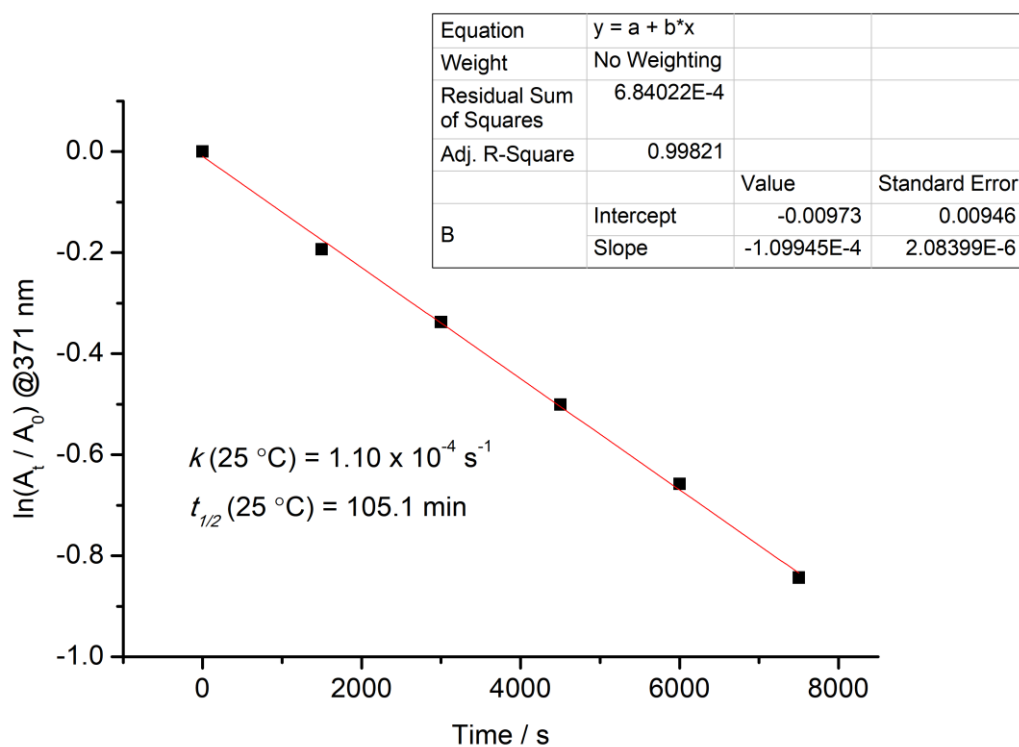


Figure 108: Graph showing the linear fit of the change in absorbance at 371 nm over time at 25 °C (PAT 9). Rate constant k (= slope) and calculated $t_{1/2}$ are mentioned.

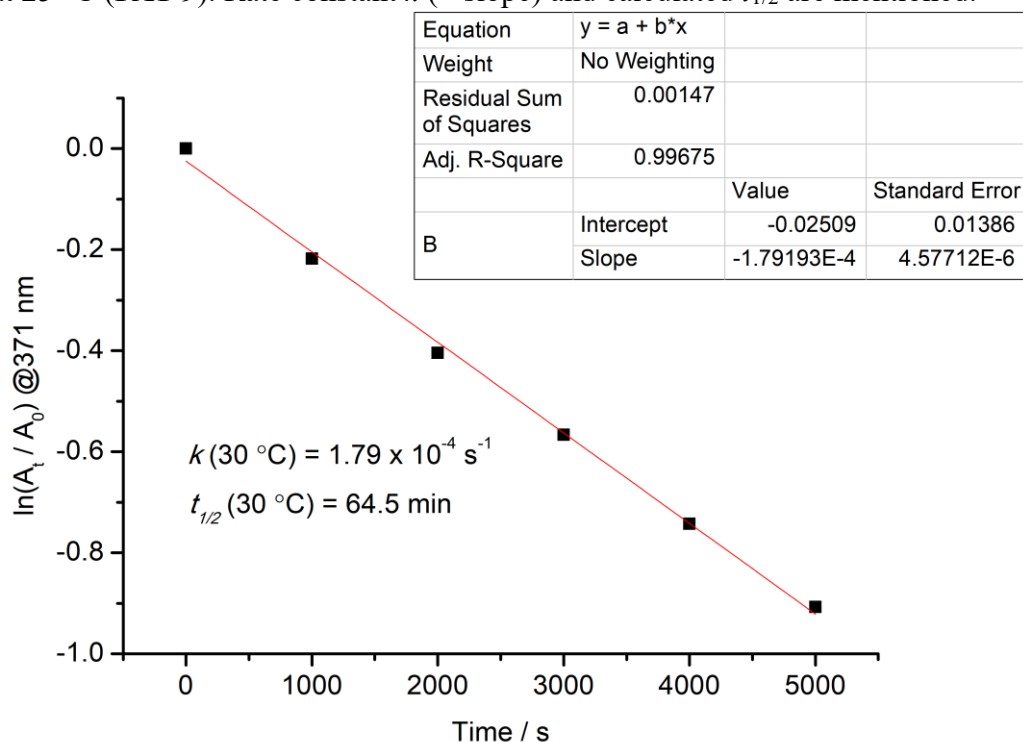


Figure 109: Graph showing the linear fit of the change in absorbance at 371 nm over time at 30 °C (PAT 9). Rate constant k (= slope) and calculated $t_{1/2}$ are mentioned.

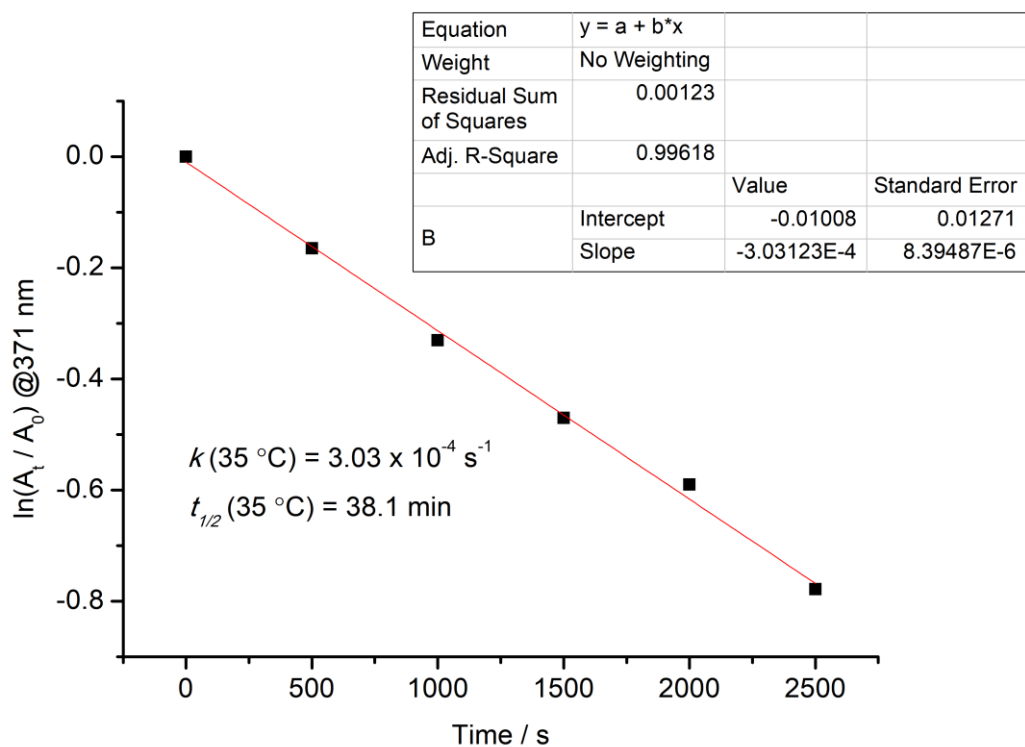


Figure 110: Graph showing the linear fit of the change in absorbance at 371 nm over time at 35 °C (PAT 9). Rate constant k (= slope) and calculated $t_{1/2}$ are mentioned.

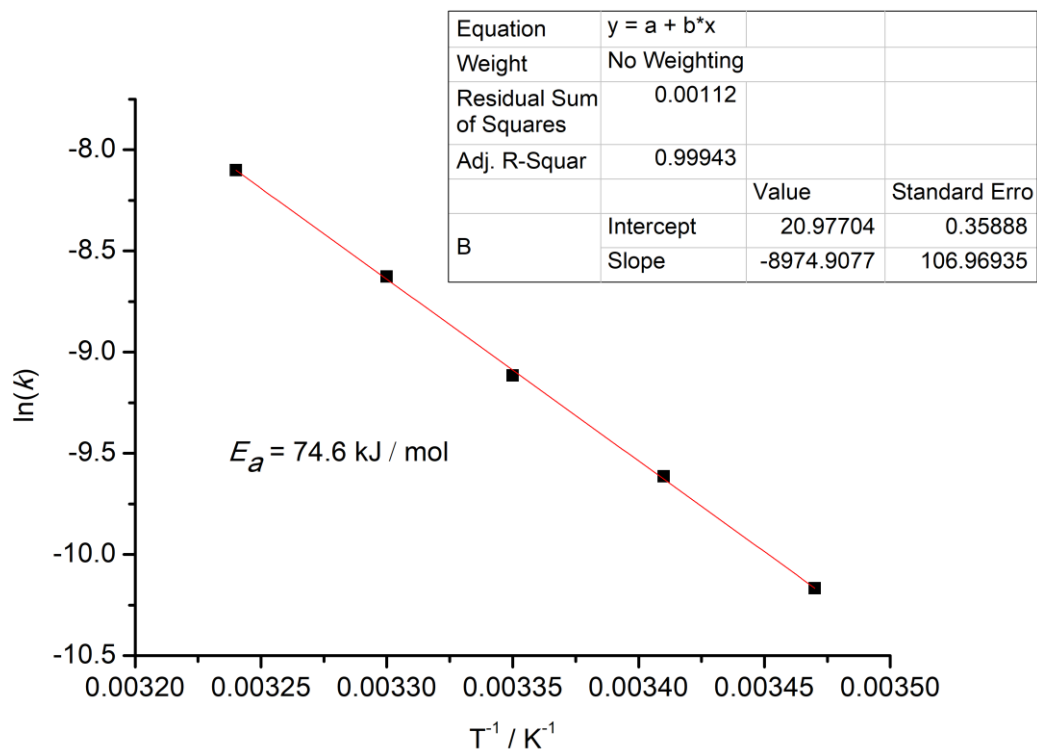


Figure 111: Arrhenius plot of PAT 9. Calculated activation energy (E_a) is mentioned.

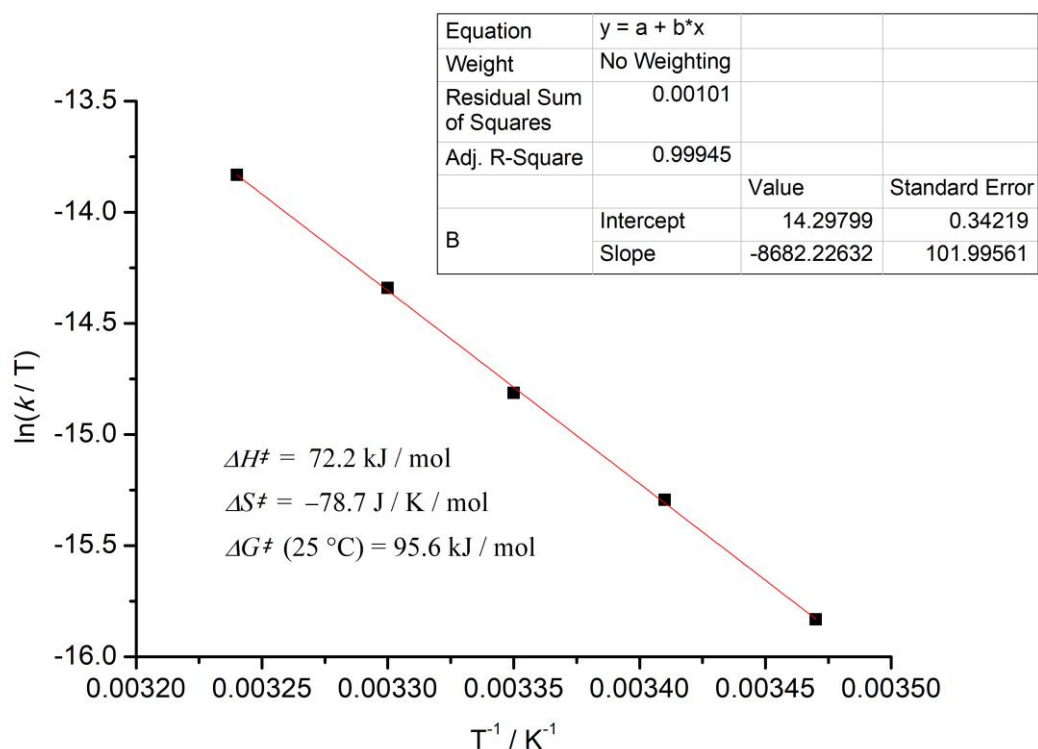


Figure 112: Eyring plot of **PAT 9**. Calculated entropy of activation (ΔS^\ddagger), enthalpy of activation (ΔH^\ddagger) and Gibbs free energy (ΔG^\ddagger) are mentioned.

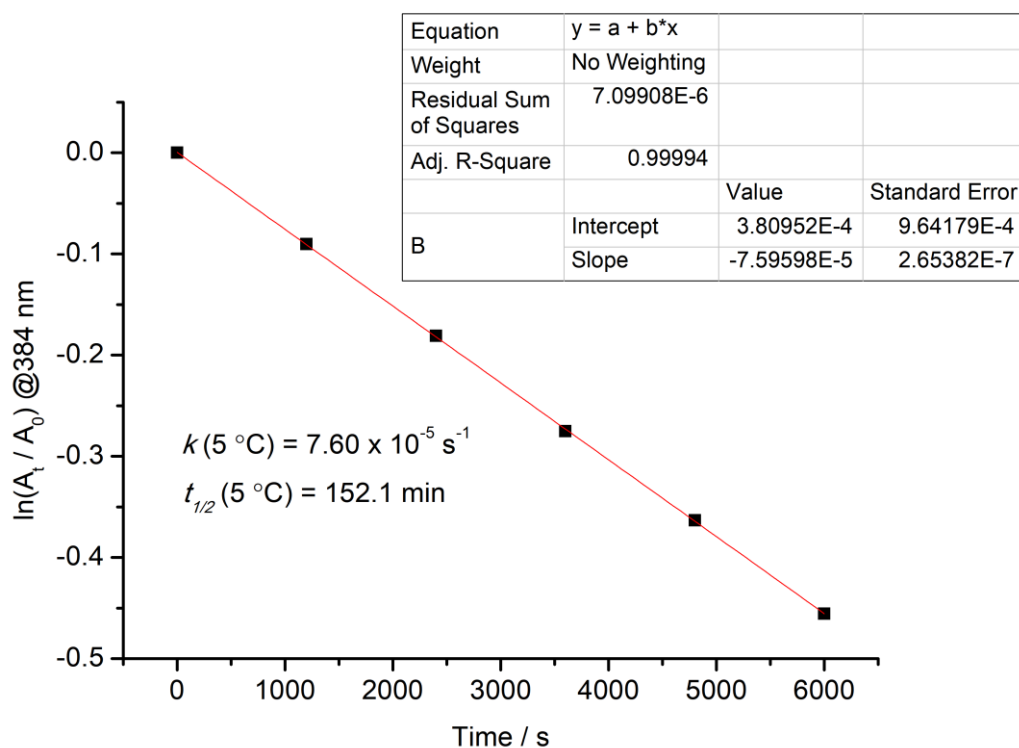


Figure 113: Graph showing the linear fit of the change in absorbance at 384 nm over time at 5°C (**PAT 11**). Rate constant k (= slope) and calculated $t_{1/2}$ are mentioned.

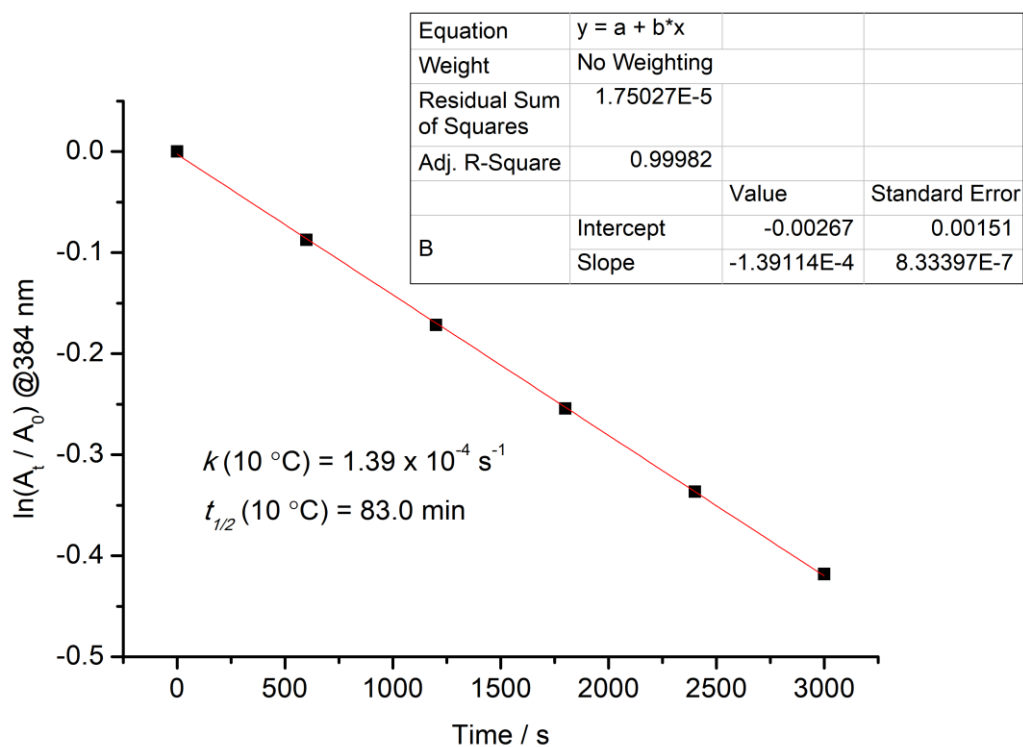


Figure 114: Graph showing the linear fit of the change in absorbance at 384 nm over time at 10 °C (PAT 11). Rate constant k (= slope) and calculated $t_{1/2}$ are mentioned.

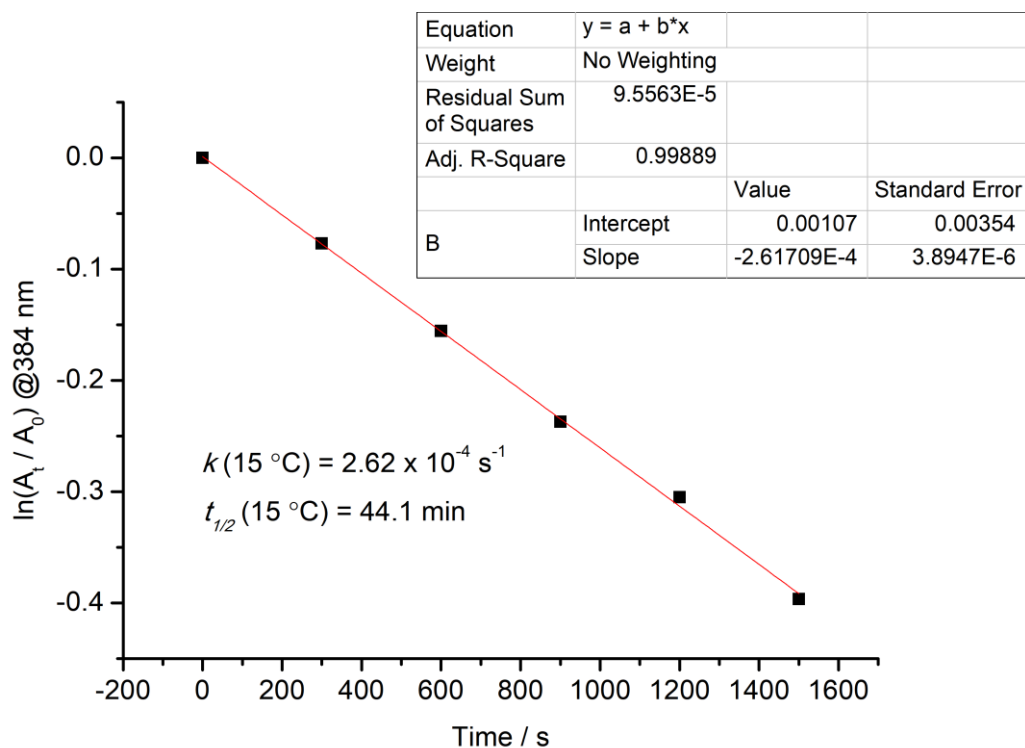


Figure 115: Graph showing the linear fit of the change in absorbance at 384 nm over time at 15 °C (PAT 11). Rate constant k (= slope) and calculated $t_{1/2}$ are mentioned.

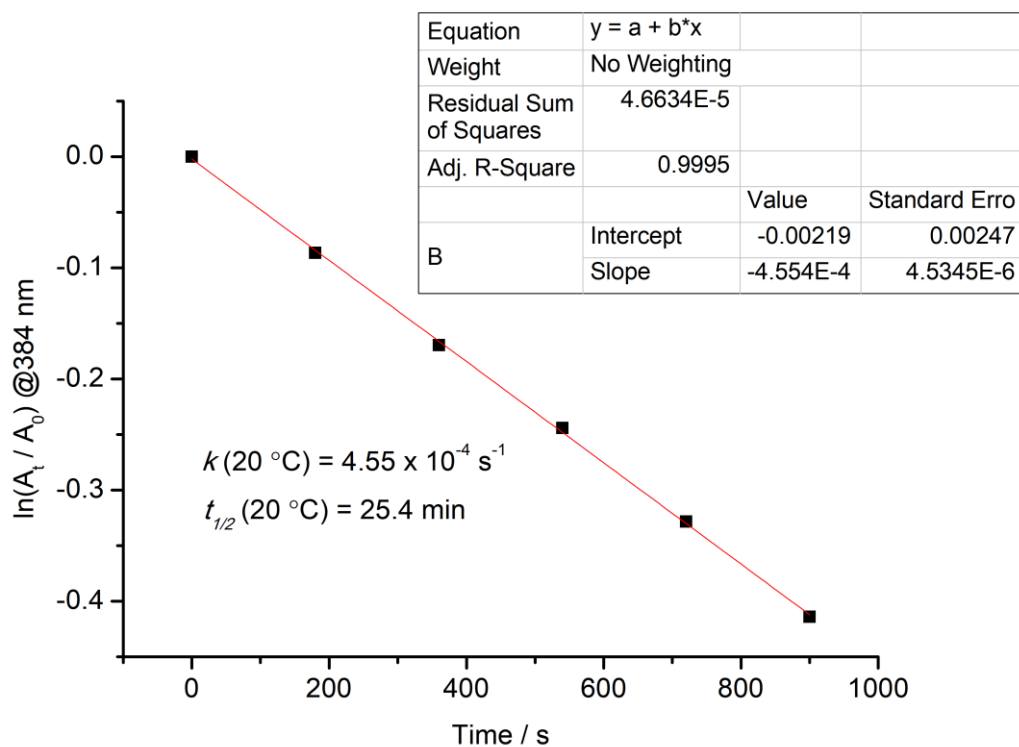


Figure 116: Graph showing the linear fit of the change in absorbance at 384 nm over time at 20 °C (PAT 11). Rate constant k (= slope) and calculated $t_{1/2}$ are mentioned.

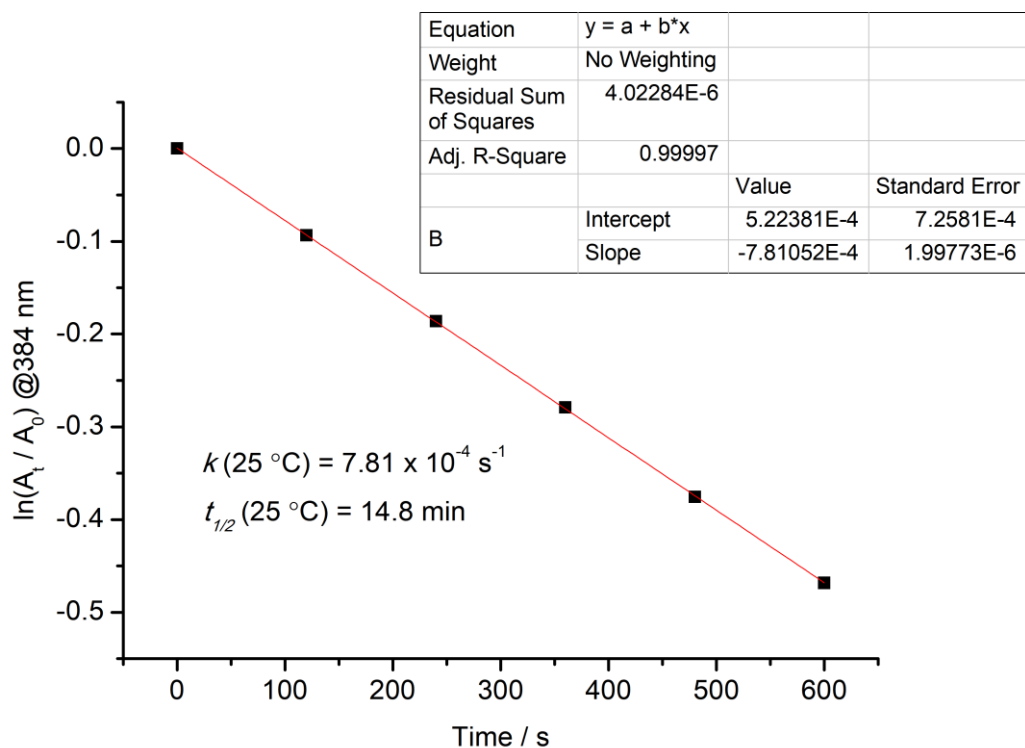


Figure 117: Graph showing the linear fit of the change in absorbance at 384 nm over time at 25 °C (PAT 11). Rate constant k (= slope) and calculated $t_{1/2}$ are mentioned.

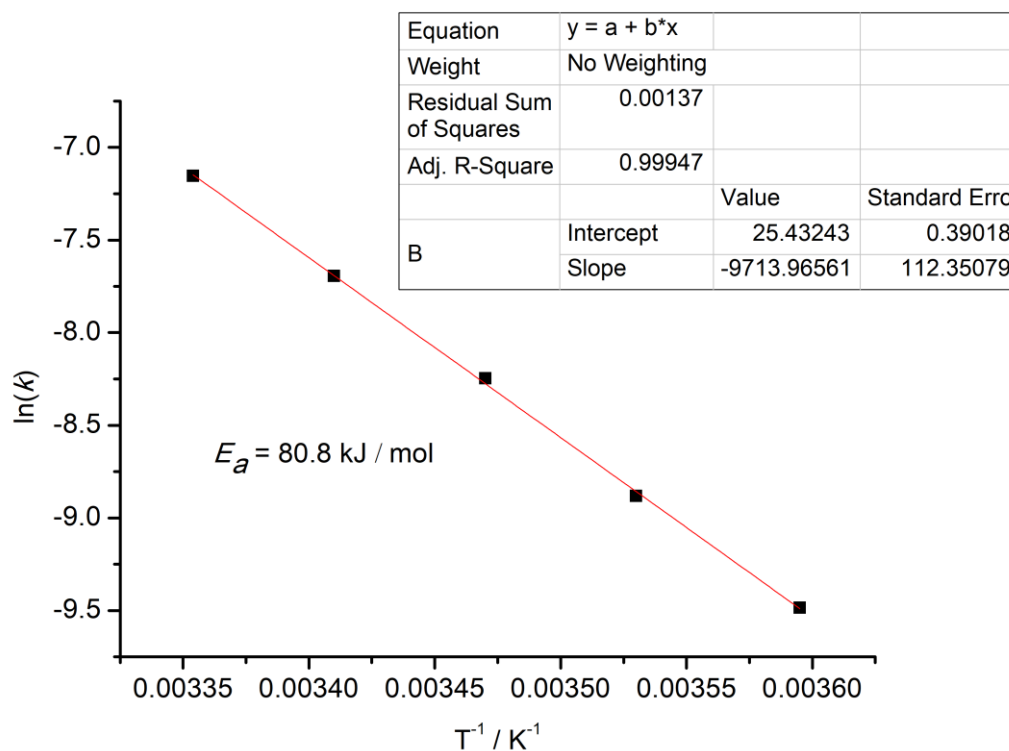


Figure 118: Arrhenius plot of **PAT 11**. Calculated activation energy (E_a) is mentioned.

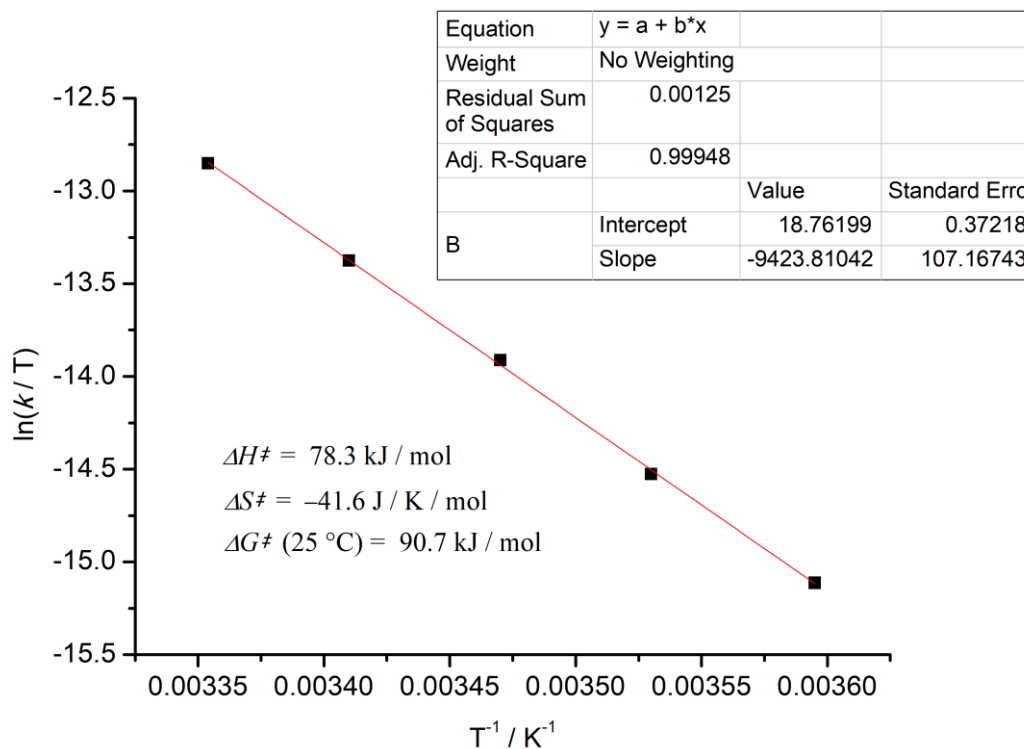


Figure 119: Eyring plot of **PAT 11**. Calculated entropy of activation (ΔS^\ddagger), enthalpy of activation (ΔH^\ddagger) and Gibbs free energy (ΔG^\ddagger) are mentioned.

2.2.6 Photophysical and thermal isomerization properties of PATs in aqueous media.

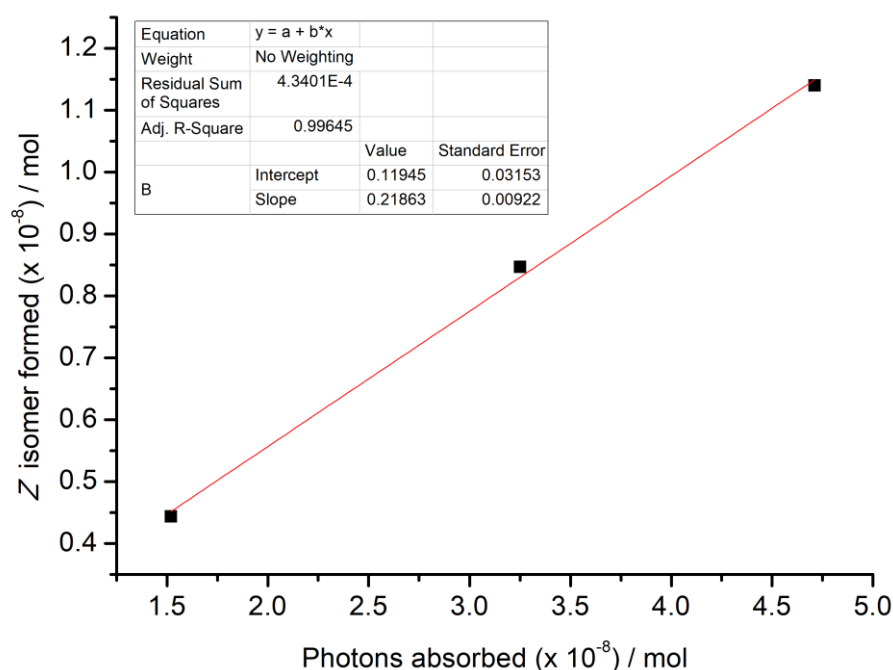


Figure 120: Graph showing the amount of Z-isomer of **PAT 1** formed for the different light intensity in H₂O / acetonitrile (95 / 5). Photons absorbed by **PAT 1** were calculated and the slope of the graph gives the quantum yield for the *E*→*Z* isomerization of **PAT 1**.
E → *Z* quantum yield = 0.22
Z → *E* quantum yield = 0.52

Table 9 Peak wavelength of absorption band ($\pi \rightarrow \pi^*$) and isomer ratio at photostationary states and half-life of Z-isomer of **PAT 1** in various solvents at 25 °C.

Solvent	λ_{\max} (nm)	PSS ₄₀₅ (Z%)	PSS ₅₂₅ (E%)	$t_{1/2}$ (h)
CH ₃ CN	364	88	78	2.77
CH ₃ CN:H ₂ O (50:50)	365	87	83	2.89
CH ₃ CN:H ₂ O (5:95)	365	85	83	2.90
CH ₃ CN:Buffer (5:95) pH = 5	367	86	89	2.62
CH ₃ CN:Buffer (5:95) pH = 7	367	85	78	2.92
CH ₃ CN:Buffer (5:95) pH = 11	367	85	85	2.84

Table 10 Peak wavelength of absorption band and half-life of Z-isomer of **PAT 6** in various solvents at 25 °C.

Solvent	λ_{\max} (nm)	$t_{1/2}$
Acetonitrile	482	2 s
1:1 Acetonitrile/ water	490	11 ms
Chloroform	478	21 s
Toluene	476	42 s

Table 11 Peak wavelength of absorption band and half-life of Z-isomer of **PAT 10** in various solvents at 25 °C.

Solvent	λ_{max} (nm)	$t_{1/2}$
Acetonitrile	484	2 s
1:1 Acetonitrile/ water	498	1.85 ms

2.3 X-ray single-crystal structures of Phenylazothiazoles

For a deeper understanding regarding the molecular geometry of PAT photoswitches, I examined the X-ray single-crystal structures of the *E* and *Z* isomers. The *E* isomers of **1** and **3** adopted a conformation in which the phenyl and thiazole parts were coplanar (Figure 121a), as in the case of azobenzene. However, the *Z* isomers adopted an unusual T-shaped conformation with orthogonal geometry of the two aromatic rings in which the S atom of thiazole was facing the phenyl aromatic ring. This is in sharp contrast to the *Z* isomer of azobenzene, which possesses a twisted geometry in the two phenyl rings are twisted. Although calculations have predicted this type of perfect T-shaped conformation in the *Z* isomer of some heteroaryl azo compounds, this has not been demonstrated experimentally.^{54, 58} In our case, the X-ray crystal structure of *Z*-**1** clearly showed a perfect T-shaped conformation with a dihedral angle of 89.7°(Phenyl-CNNC). For *Z*-**3** with a bulky Cl substituent, the dihedral angle for Phenyl-CNNC was 98.4°, which slightly deviated from the T-shaped conformation (Figure 121a).

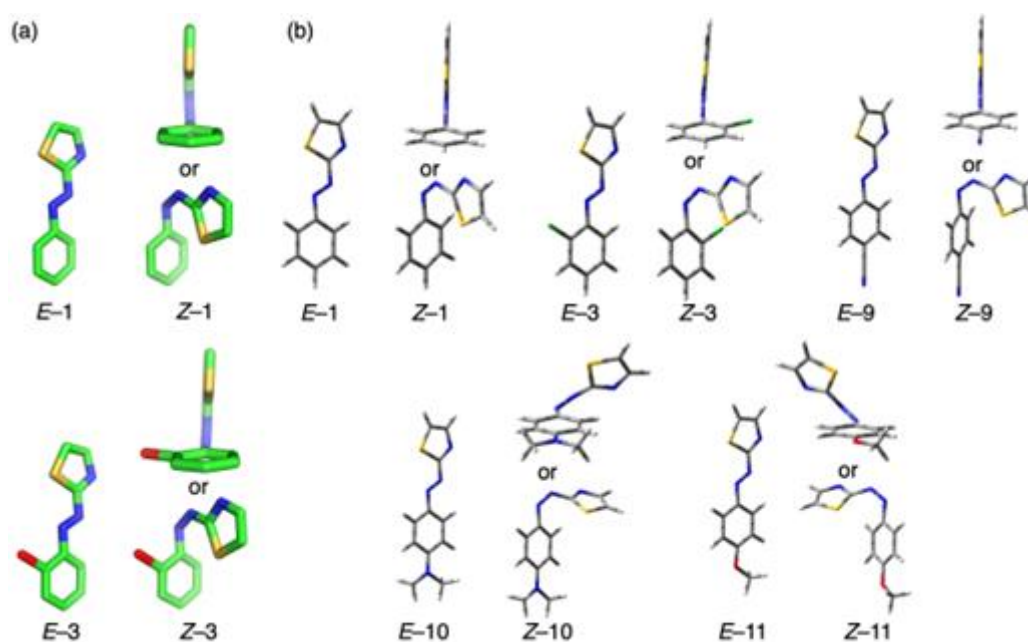


Figure 121. (a) Single-crystal X-ray structures of both *E* and *Z* isomers of **1** and **3** (green = C; blue = N; golden = S; red = Cl). Hydrogens are omitted for clarity. (b) Geometry optimized calculated conformations of *E* and *Z* isomers of **1**, **3**, **9**, **10**, and **11**.

2.4 Theoretical calculations.

To gain further insights into the molecular structures, molecular orbital energy levels, and energy barriers for isomerization, we performed density functional theory (DFT) calculations using a 6-31+G(d,p) basis set with Becke's three-parameter hybrid exchange and the Lee–Yang–Parr correlation functional (B3LYP) including the Grimme dispersion correction in acetonitrile medium. The most stable optimized geometry in the ground state of both the *E* and *Z* isomers of **1**, **3**, **9**, **10**, and **11** are shown in Figure 121b and Tables 12–21 and the less stable conformers are shown in Figure 124. A planar geometry was observed in the *E* isomers of **1**, **3**, **9**, **10**, and **11** with the phenyl, azo, and thiazole moieties in the same plane. However, in the *Z* isomers of the same PAT derivatives (**1**, **3**, and **9**), an orthogonal geometry was observed with the S atom of the thiazole ring facing the phenyl ring (Figure 121b). For *Z*–**1** and *Z*–**3**, the X-ray crystal structure analysis unambiguously revealed the orthogonal geometry with the S atom of the thiazole ring facing the phenyl ring. In contrast, the calculated conformers of *Z*–**10** and *Z*–**11** showed a twisted conformation (Figures 121b and 125). This calculation result and the X-ray crystal structures of the *Z* isomers are explained as follows: the origin of the attractive force stabilizing the T-shaped conformation in *Z*–**1** and *Z*–**3** was the electron transfer from the S lone pair to the π^* antibonding orbital in the phenyl ring. This effect was weakened in *Z*–**10** and *Z*–**11** with electron-donating NMe₂ and OMe substituents, respectively.^{66, 67} The n-orbital of the S atom extended farther than that of the N atom, which explains the favored orientation of the thiazole in the T-shaped conformer with the S atom rather than the N atom facing the phenyl ring, which provides a π^* orbital on the ring plane.

We then simulated the theoretical absorption spectra of both the *E* and *Z* isomers of **1**, **3**, **9**, **10**, and **11** in acetonitrile, which showed strong $\pi \rightarrow \pi^*$ and weak $n \rightarrow \pi^*$

electronic transitions (Figure 126). For instance, the λ_{max} of the calculated spectra of *E*-**1** appeared at 397 nm (oscillatory strength (f) = 0.704) and 477 nm (f = 0.000), whereas that of *Z*-**1** appeared at 350 nm (f = 0.024) and 502 nm (f = 0.001). The λ_{max} ($\pi \rightarrow \pi^*$) of the substituted **PAT** (*E*-**3** (411 nm), *E*-**9** (412 nm), *E*-**10** (475 nm), and *E*-**11** (430 nm)) was further redshifted compared with the parent **PAT** (*E*-**1** (397 nm)), which was similar to the trend observed in the experimental spectra. The relative intensities of the $n \rightarrow \pi^*$ transitions of *Z*-**10** ($f_{527 \text{ nm}} = 0.202$) and *Z*-**11** ($f_{529 \text{ nm}} = 0.113$) were much higher than that of *Z*-**1** ($f_{502 \text{ nm}} = 0.001$). The $n \rightarrow \pi^*$ transition was symmetry-allowed for *Z*-**10** and *Z*-**11** because of their twisted orthogonal geometry, but symmetry-forbidden for *Z*-**1**.³⁸ The experimentally obtained molar extinction coefficient (ϵ) of *Z*-**11** corresponding to the $n \rightarrow \pi^*$ transition was 2044 M⁻¹cm⁻¹. The $n \rightarrow \pi^*$ transition at 550 nm in the calculated absorption spectra of *Z*-**10** was supported by the flash photolysis results, in which a sudden increase in the absorbance at 550 nm was observed (Figure 56). Figure 122 shows the frontier molecular orbitals and the electron distribution at each group in the *E* isomers of **1** and **10**. The highest occupied molecular orbital (HOMO), lowest unoccupied molecular orbital (LUMO), and HOMO-1 have a π , π^* , and n nature, respectively.⁶⁸ During the $\pi \rightarrow \pi^*$ transition, the electron density of thiazole decreases more than that of phenyl, whereas that of the azo group increases. The nature of this intramolecular charge transfer from electron-rich thiazole to azo upon the $\pi \rightarrow \pi^*$ transition of **1** could be the origin of the red-shift in absorbance compared with azobenzene.⁶⁹ An enormous electron-density shift from the NMe₂-substituted phenyl to azo and to thiazole is observed in **10**, which contributes to its further red-shift in the $\pi \rightarrow \pi^*$ transition band.

We then calculated the potential energy diagrams for the *Z* \rightarrow *E* isomerization using the B3LYP/6-31+G(d,p) level of theory. To determine the preferred thermal

isomerization pathway, we calculated the activation energies for the inversion and rotation pathways separately (Figures 127–129). The inversion pathway can occur either via the azo phenyl (inversion-*Ph*) or azo thiazole (inversion-*Th*) segments. The obtained relative energies of the *Z* isomers of **1**, **3**, **10**, and **11** were 62–75 kJ mol⁻¹ higher than those of the *E* isomers, indicating the reduced stability of the *Z* isomer than the *E* isomer (Figure 127). We found that **1**, **3**, and **11** isomerized via inversion-*Th*, whereas **9** isomerized via inversion-*Ph*. Interestingly, **10** isomerized via the rotation of the azo segment (Figure 123a and Table 14). The calculated potential energy barriers for the *Z*→*E* thermal isomerization ($\Delta E_{Z\rightarrow E}$) of **10** (67.86 kJ mol⁻¹) and **11** (88.14 kJ mol⁻¹) having electron-donating NMe₂ and OMe substituents, respectively, were much lower than that of **1** (94.06 kJ mol⁻¹) (Figure 123b). The calculated activation energies (E_a^{cal}) for the *Z*→*E* thermal isomerization followed a similar trend as the experimentally obtained activation energies (Table 1).

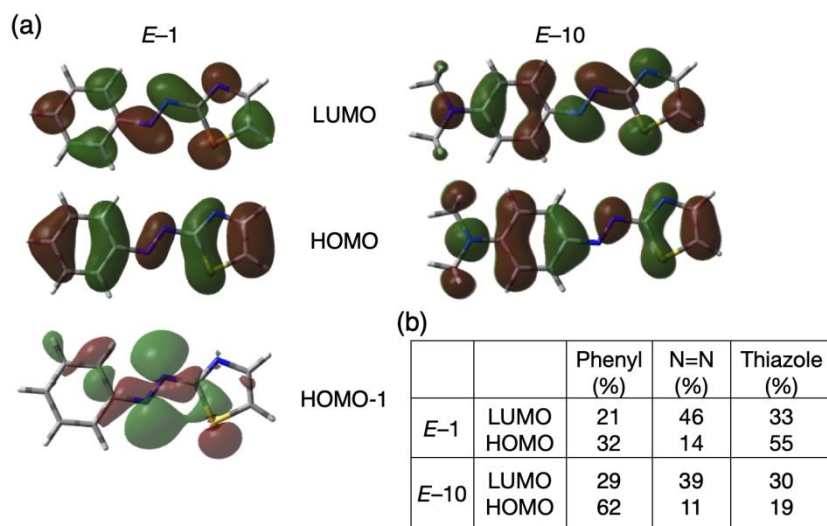


Figure 122. (a) LUMO, HOMO, and HOMO-1 of *E*-1 and *E*-10. (b) HOMO and LUMO electron distributions at different groups having π and π^* natures (phenyl, N=N, and thiazole units) in *E*-1 and *E*-10.

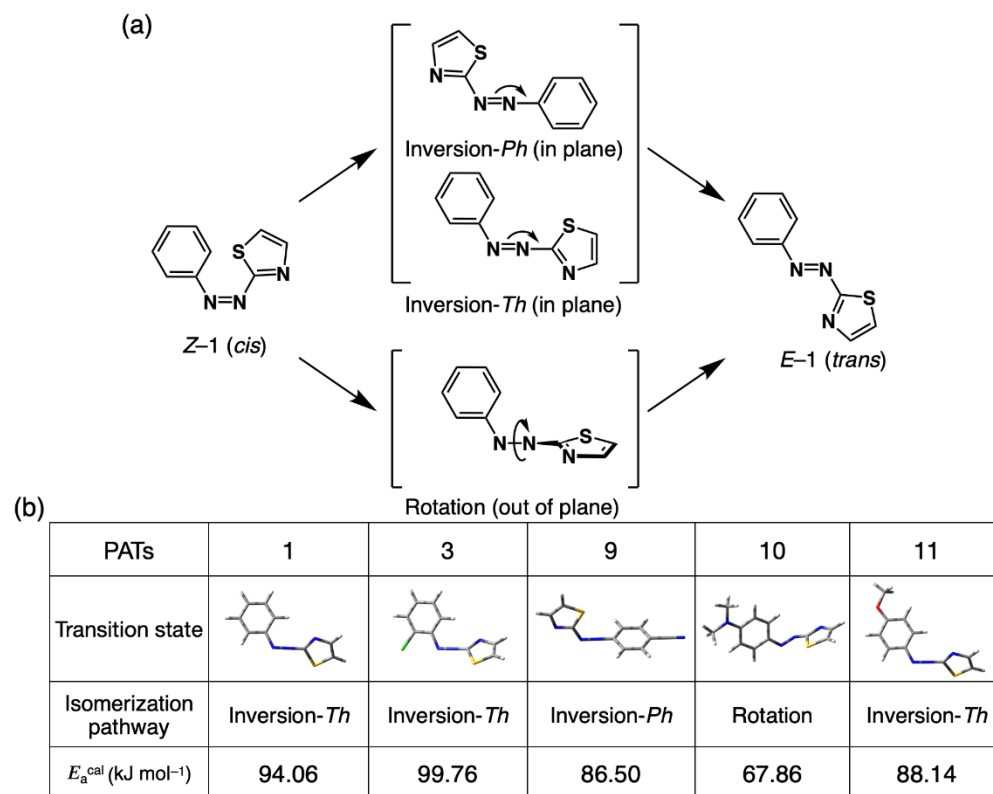


Figure 123. (a) Scheme showing the inversion and rotation pathways for the isomerization of 1. (b) Transition states and calculated activation energies (E_a^{cal}) of PAT derivatives.

2.4.1 Time-dependent density-functional theory (TDDFT) calculations

Theoretical calculations were performed using Gaussian 09 (Revision D.01).⁷⁰ GaussView 6.0 was used to draw and visualize the molecular structures and to feed the inputs.⁷¹ Density functional theory (DFT) and time dependent density functional theory (TDDFT) were employed to optimize the geometries and to obtain the electronic transition in the ground state, respectively.⁷²⁻⁷⁴ The 6-31+G(d,p) basis set with Becke's three-parameter hybrid exchange and the Lee-Yang-Parr's correlation functional (B3LYP) was used for geometry optimization.⁷⁵ The solvent stabilization of different isomers was incorporated by considering integral equation formalism-polarizable continuum model (IEF-PCM) and choosing acetonitrile as medium.⁷⁶ Potential energy diagram for the *E*-*Z* isomerization is obtained from the dihedral scan by 0° to 180° rotation of the C-N=N-C dihedral angle or by inversion along -N=N-C bond.

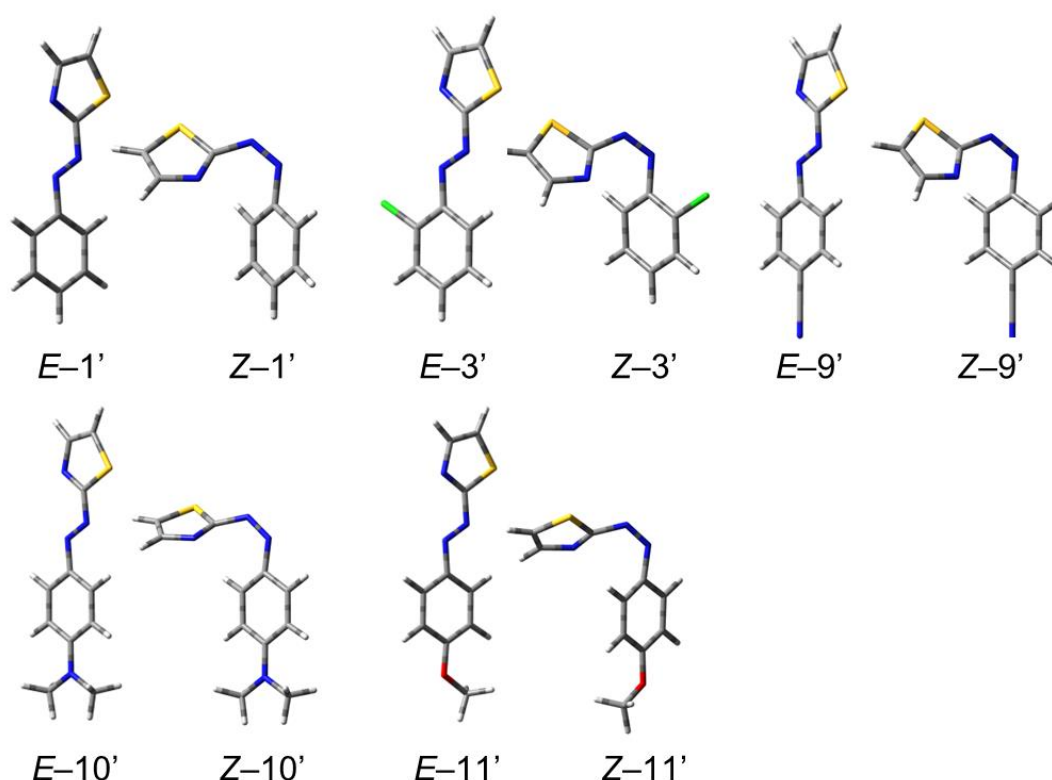


Figure 124. Optimized geometry of conformers of PAT **1**, **3**, **9**, **10** and **11**. These are less stable conformer compared to the more stable conformer shown in Figure 121b.

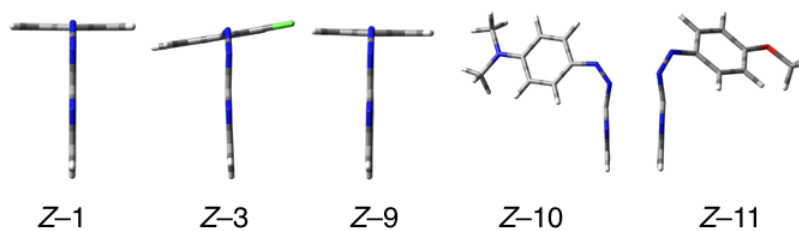


Figure 125. Calculated conformation of *Z*-isomers of **PAT 1, 3, 9, 10** and **11** showing “T-shape” or tilted (deviation) “T-shape”. Thiazole ring and azo bond are in the vertical plane with respect to the phenyl ring in the horizontal plane. In the case of *Z*-**10** and *Z*-**11**, deviation from “T-shape” geometry is clearly visible.

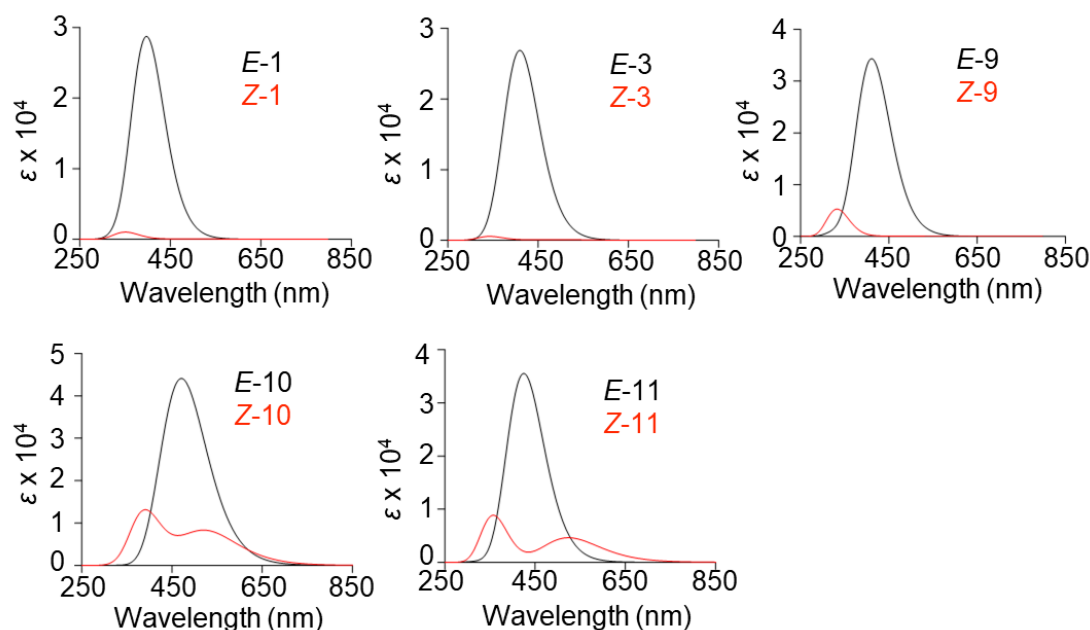


Figure 126. Calculated absorption spectra of *E* and *Z* isomers of **1, 3, 9, 10** and **11**.

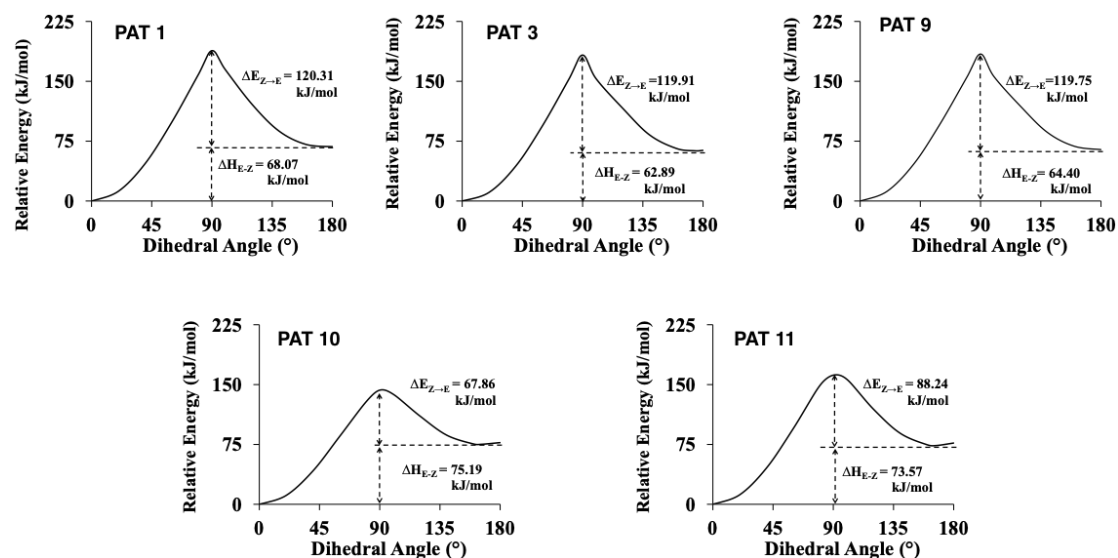


Figure 127. Potential energy diagram for *E*–*Z* isomerization obtained from the dihedral scan (0–180 °C) in S_0 along C–N=N–C (rotation) for **PAT 1, 3, 9, 10** and **11**. The calculated energy barrier ($\Delta E_{Z \rightarrow E}$) and the relative enthalpy (ΔH_{E-Z}) are shown with arrows.

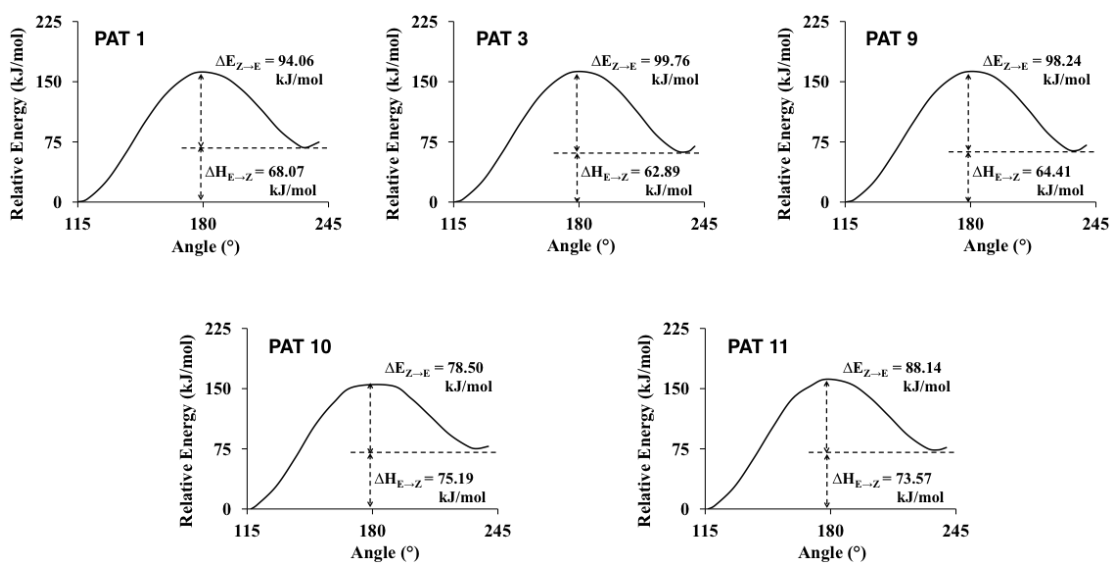


Figure 128. Potential energy diagram for *E*–*Z* isomerization obtained from the bond angle scan in S_0 along –N=N–C (inversion at thiazole segment) for PAT **1**, **3**, **9**, **10** and **11**. The calculated energy barrier ($\Delta E_{Z \rightarrow E}$) and the relative enthalpy ($\Delta H_{E \rightarrow Z}$) are shown with arrows.

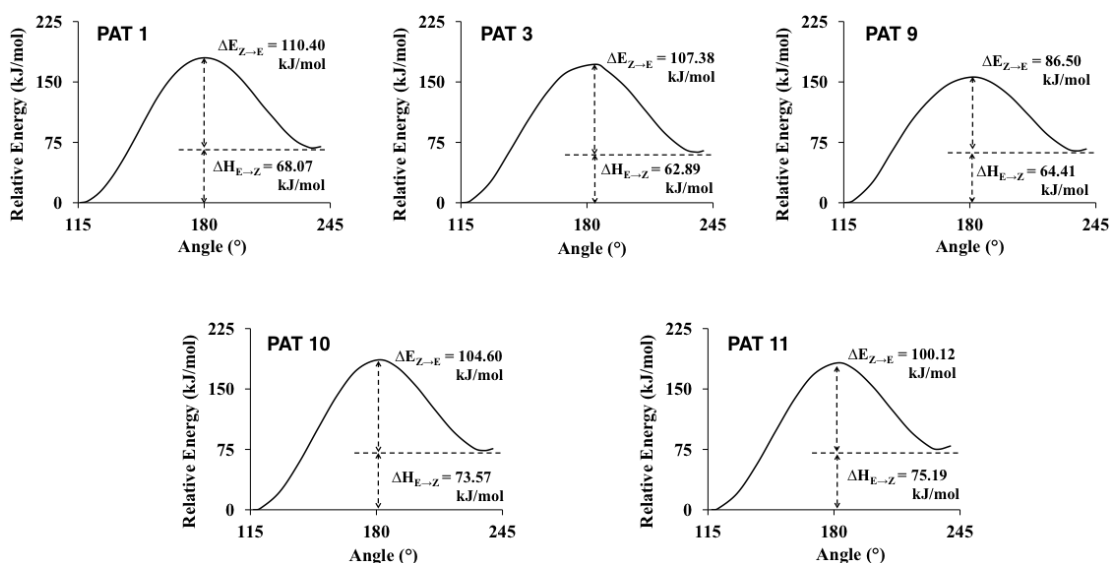
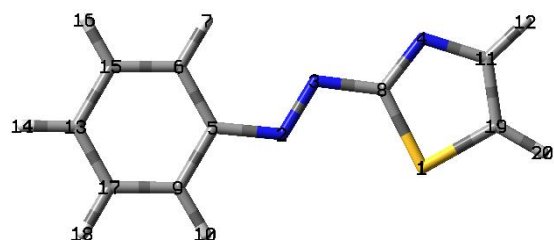


Figure 129. Potential energy diagram for *E*–*Z* isomerization obtained from the bond angle scan in S_0 along –N=N–C (inversion at phenyl segment) for PAT **1**, **3**, **9**, **10** and **11**. The calculated energy barrier ($\Delta E_{Z \rightarrow E}$) and the relative enthalpy ($\Delta H_{E \rightarrow Z}$) are shown with arrows.

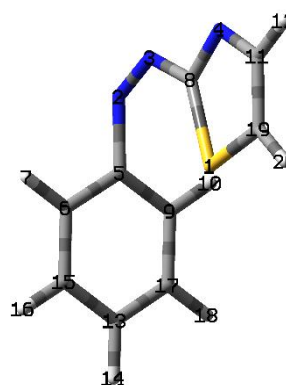
Table 12. The XYZ-coordinates of optimized E1 in the ground state.



Center Number	Coordinates (Angstroms)		
	X	Y	Z
1	2.50536	-	-
		1.18511	0.00017
2	-0.29138	-	0.00007
		0.32671	
3	0.43895	0.70400	0.00000
4	2.67964	1.41764	-
			0.00030
5	-1.68279	-	0.00006
		0.10139	
6	-2.29058	1.17114	-
			0.00001
7	-1.67222	2.06125	-
			0.00004
8	1.80181	0.44144	-
			0.00002
9	-2.47483	-	0.00011
		1.26211	
10	-1.98377	-	0.00015
		2.23015	
11	3.95715	0.92349	-
			0.00008
12	4.79468	1.61012	-
			0.00011
13	-4.46924	0.10351	0.00003
14	-5.55173	0.18793	0.00002
15	-3.67820	1.26401	-

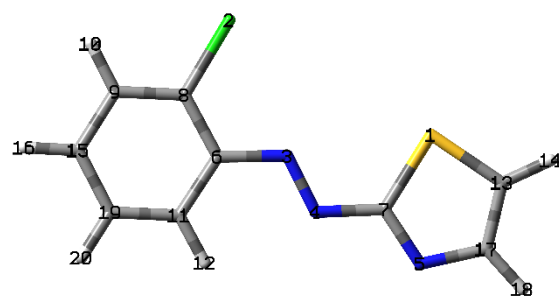
			0.00002
16	-4.15204	2.24091	-
			0.00007
17	-3.86628	-	0.00010
		1.15814	
18	-4.47666	-	0.00014
		2.05559	
19	4.06853	-	0.00043
		0.44488	
20	4.97209	-	0.00076
		1.03966	

Table 13. The XYZ-coordinates of optimized Z1 in the ground state.



Center Number	Coordinates (Angstroms)		
	X	Y	Z
1	0.97679	-	-
		1.01206	0.00091
2	-0.33707	2.03129	-
			0.00010
3	0.90669	1.87979	0.00008

4	2.91265	0.71949	0.00068
5	-1.25618	0.92386	0.00005
6	-1.75521	0.44495	1.21866
7	-1.37646	0.84771	2.15276
8	1.59541	0.65185	0.00013
9	-1.75664	0.44586	-
			1.21832
10	-1.37900	0.84934	-
			2.15256
11	3.48013	-	0.00033
		0.51829	
12	4.55892	-	0.00074
		0.61247	
13	-3.20625	-	0.00046
		1.07027	
14	-3.95991	-	0.00062
		1.85151	
15	-2.72312	-	1.21114
		0.56189	
16	-3.10184	-	2.15380
		0.94520	
17	-2.72450	-	-
		0.56103	1.21041
18	-3.10429	-	-
		0.94369	2.15290
19	2.60111	-	-
		1.57678	0.00062
20	2.82951	-	-
		2.63462	0.00112



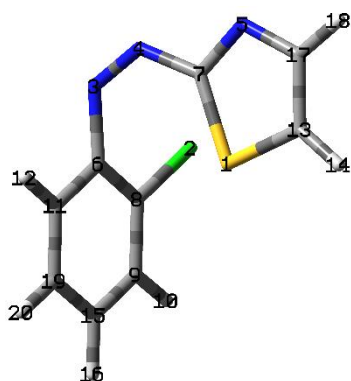
Center Number	Coordinates (Angstroms)		
	X	Y	Z
1	2.67358	1.06094	0.00012
2	-1.82957	2.29815	-
			0.00009
3	-0.02195	-	0.00002
		0.06319	
4	0.80361	-	-
		1.01951	0.00006
5	3.10164	-	-
		1.51265	0.00012
6	-1.37981	-	0.00001
		0.42560	
7	2.13281	-	-
		0.62543	0.00003
8	-2.33277	0.61596	-
			0.00002
9	-3.69968	0.33576	-
			0.00002
10	-4.41416	1.15111	-
			0.00006
11	-1.84056	-	0.00007
		1.75923	
12	-1.10676	-	0.00011
		2.55682	
13	4.29991	0.47718	0.00006
14	5.14104	1.15754	0.00012
15	-4.13138	-	0.00003
		0.99128	
16	-5.19544	-	0.00004
		1.20488	
17	4.32363	-	-
		0.89669	0.00007

Table 14. The XYZ-coordinates of optimized E3 in the ground state.

18	5.22446	-	-
		1.49775	0.00013
19	-3.20000	-	0.00007
		2.03983	
20	-3.53959	-	0.00012
		3.07041	

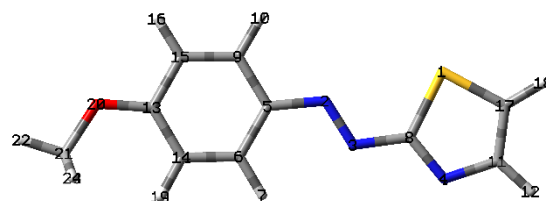
		0.06075	1.01936
10	-3.00619	0.41118	-
			1.90317
11	-1.50916	-	1.27592
		1.24577	
12	-1.08773	-	2.17345
		1.68702	
13	2.84567	-	-
		1.02025	1.21112
14	3.12073	-	-
		1.64200	2.05310
15	-2.97910	-	-
		1.34894	0.64427
16	-3.70663	-	-
		1.88350	1.24612
17	3.66361	-	-
		0.23106	0.43421
18	4.73181	-	-
		0.12414	0.57576
19	-2.43852	-	0.50236
		1.94001	
20	-2.74394	-	0.79924
		2.93802	

Table 15. The XYZ-coordinates of optimized Z3 in the ground state.



Center Number	Coordinates (Angstroms)		
	X	Y	Z
1	1.21782	-	-
		0.92098	0.66962
2	-1.15245	2.24189	-
			0.73190
3	-0.22857	0.78009	1.76775
4	1.01307	0.83375	1.61220
5	3.04755	0.44113	0.57561
6	-1.09077	0.03528	0.89051
7	1.75068	0.20067	0.60002
8	-1.65553	0.62787	-
			0.24772
9	-2.59119	-	-

Table 16. The XYZ-coordinates of optimized E11 in the ground state.

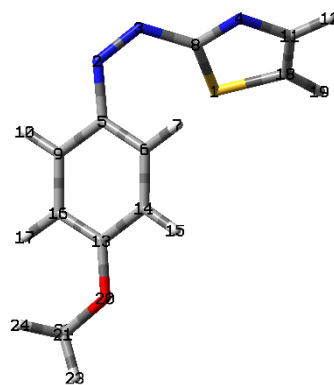


Center Number	Coordinates (Angstroms)		
	X	Y	Z

1	3.44443	1.10154	-
			0.00056
2	0.61323	0.39302	-
			0.00017
3	1.28641	-	-
		0.68108	0.00011
4	3.48989	-	-
		1.50724	0.00027
5	-0.77845	0.26143	-
			0.00003
6	-1.47770	-	0.00013
		0.96309	
7	-0.92386	-	0.00017
		1.89487	
8	2.65976	-	-
		0.49029	0.00013
9	-1.50591	1.46992	-
			0.00008
10	-0.96034	2.40826	-
			0.00020
11	4.79164	-	-
		1.07531	0.00007
12	5.59367	-	0.00002
		1.80331	
13	-3.58265	0.23412	0.00019
14	-2.86573	-	0.00024
		0.98141	
15	-2.89087	1.45998	0.00003
16	-3.46115	2.38259	-
			0.00001
17	4.97162	0.28423	0.00035
18	5.90345	0.83358	0.00070
19	-3.38360	-	0.00036
		1.93228	
20	-4.93342	0.32116	0.00027
21	-5.71435	-	0.00063
		0.88380	
22	-6.75373	-	0.00077
		0.55755	
23	-5.51452	-	-

		1.47908	0.89655
24	-5.51417	-	0.89792
		1.47878	

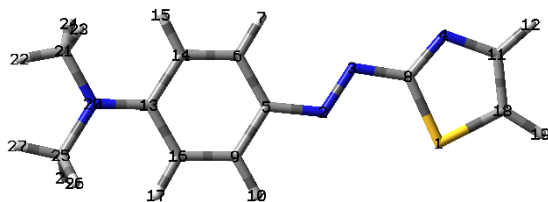
Table 17. The XYZ-coordinates of optimized Z11 in the ground state.



Center	Coordinates	(Angstroms)	
Number	X	Y	Z
1	-1.91739	0.70007	-
			1.11599
2	-0.71269	-	0.04662
		2.15747	
3	-1.91799	-	0.15517
		1.81525	
4	-3.38674	-	0.87390
		0.10343	
5	0.37720	-	0.13741
		1.25409	
6	0.44653	-	1.06673
		0.19329	
7	-0.38551	0.00869	1.73187
8	-2.38334	-	0.12249
		0.47925	
9	1.49696	-	-

		1.55064	0.65202				
10	1.45545	-	-	2	-0.98725	-	-
		2.39902	1.32786			0.32572	0.00002
11	-3.80403	1.16439	0.54162	3	-1.71215	0.72544	-
12	-4.61488	1.61860	1.09759				0.00007
13	2.69064	0.31789	0.30499	4	-3.95541	1.44115	-
14	1.59439	0.57385	1.15449				0.00006
15	1.67204	1.37924	1.87717	5	0.38332	-	-
16	2.63857	-	-			0.14560	0.00009
		0.75293	0.60275	6	1.04893	1.10655	-
							0.00026
17	3.47576	-	-	7	0.46366	2.01919	-
		0.98372	1.24887				0.00039
18	-3.15879	1.74981	-	8	-3.07011	0.47038	-
			0.51336				0.00002
19	-3.35118	2.71003	-	9	1.16914	-	0.00005
			0.97237			1.31959	
20	3.75386	1.14512	0.45701	10	0.66328	-	0.00022
21	4.91442	0.94260	-			2.28058	
			0.36219	11	-5.23415	0.93981	0.00003
22	4.66779	1.05088	-	12	-6.07230	1.62636	0.00002
			1.42394	13	3.22856	-	-
23	5.61939	1.71947	-			0.01101	0.00014
			0.06825	14	2.42503	1.17470	-
24	5.35506	-	-				0.00027
		0.04338	0.17983	15	2.89479	2.14969	-
							0.00045
				16	2.54991	-	0.00004
						1.26559	
				17	3.10816	-	0.00026
						2.19241	
				18	-5.34624	-	0.00013
						0.42512	
				19	-6.24889	-	0.00022
						1.02106	
				20	4.58842	0.06180	-
							0.00019
				21	5.26460	1.35850	0.00073
				22	6.34133	1.19817	0.00129
				23	5.00630	1.94362	-
							0.88971

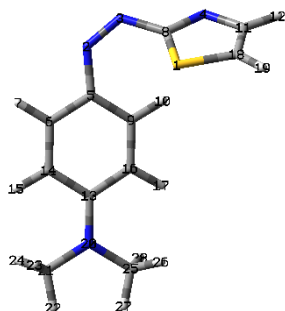
Table 18. The XYZ-coordinates of optimized E10 in the ground state.



Center	Coordinates (Angstroms)		
Number	X	Y	Z
1	-3.77505	-	0.00005
		1.16402	

24	5.00526	1.94287	0.89134
25	5.39274	-	-
		1.15891	0.00026
26	5.19202	-	-
		1.76699	0.89023
27	6.44806	-	-
		0.89164	0.00138
28	5.19359	-	0.89064
		1.76619	

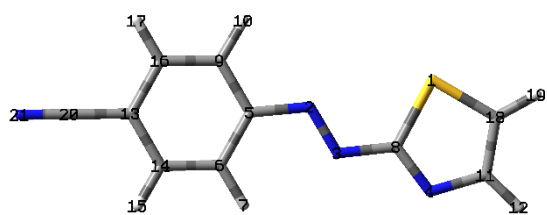
Table 19. The XYZ-coordinates of optimized Z10 in the ground state.



Center	Coordinates (Angstroms)		
Number	X	Y	Z
1	2.40705	-	1.29152
		0.43804	
2	1.12242	2.16092	-
			0.35515
3	2.31243	1.73572	-
			0.46245
4	3.51201	-	-
		0.23394	1.05722
5	-0.01756	1.35406	-
			0.28004
6	-1.15749	1.97342	0.27841
7	-1.06486	2.99207	0.64288
8	2.70357	0.39960	-
			0.24784
9	-0.16787	0.05185	-

			0.81752
10	0.65488	-	-
		0.42757	1.33409
11	3.89991	-	-
		1.44462	0.52086
12	4.55514	-	-
		2.08997	1.09321
13	-2.50874	-	-
		0.02252	0.09881
14	-2.36094	1.30560	0.39924
15	-3.19483	1.81579	0.86283
16	-1.37605	-	-
		0.61044	0.74305
17	-1.45364	-	-
		1.58951	1.19747
18	3.42785	-	0.72870
		1.72859	
19	3.62932	-	1.34567
		2.59360	
20	-3.68740	-	0.01149
		0.69664	
21	-4.84640	-	0.63322
		0.05899	
22	-5.67655	-	0.64659
		0.76315	
23	-4.63038	0.23318	1.66738
24	-5.15991	0.83229	0.07610
25	-3.82563	-	-
		2.04582	0.53432
26	-3.10028	-	-
		2.73206	0.08267
27	-4.82528	-	-
		2.41752	0.31568
28	-3.68658	-	-
		2.05522	1.62238

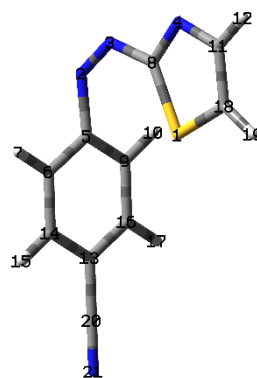
Table 20. The XYZ-coordinates of optimized E-9 in the ground state.



Center Number	Coordinates (Angstroms) X Y Z
1	-3.25555 1.16173 -0.00010
2	-0.43326 0.37218 0.00026
3	-1.14245 -0.67270 0.00010
4	-3.36007 -1.44531 0.00042
5	0.96269 0.16054 0.00015
6	1.58000 -1.10648 0.00037
7	0.97099 -2.00228 0.00063
8	-2.50863 -0.44399 0.00001
9	1.74181 1.32873 -0.00011
10	1.24457 2.29272 -0.00024
11	-4.64761 -0.98702 0.00025
12	-5.46744 -1.69451 0.00037
13	3.74386 -0.01925 0.00003
14	2.96375 -1.19535 0.00028
15	3.44928 -2.16511 0.00045
16	3.13021 1.24535 -0.00022
17	3.73518 2.14494 -0.00044
18	-4.79467 0.38039 0.00038

19	-5.71415	0.95037	0.00070
20	5.17385	-	-
21	6.33559	-	-
		0.11634	0.00012
		0.19608	0.00019

Table 21. The XYZ-coordinates of optimized Z-9 in the ground state.



Center Number	Coordinates (Angstroms) X Y Z
1	1.30337 -1.06498 0.00152
2	0.69789 2.18680 0.00008
3	1.87738 1.76633 0.00042
4	3.57720 0.19290 0.00119
5	-0.44882 1.32841 0.00008
6	-1.04911 0.98500 1.22022
7	-0.58468 1.28145 2.15448
8	2.27800 0.41995 0.00032
9	-1.05066 0.98721 -1.21991
10	-0.58742 1.28538 -2.15420
11	3.85413 -1.13917 0.00062
12	4.88431 -0.00130

			1.47265			0.03086	2.15872
13	-2.82126	-	0.00027	18	2.76063	-	-
			0.12509			1.97566	0.00089
14	-2.22886	0.24875	1.22058	19	2.74670	-	-
15	-2.69198	-	2.15927			3.05773	0.00165
			0.03463	20	-4.03612	-	0.00035
16	-2.23036	0.25089	-			0.88479	
			1.22010	21	-5.02270	-	0.00041
17	-2.69463	-	-			1.50377	

Table 22. Potential energy barrier (kJ/mol) for different isomerization pathways. $\Delta H_{E \rightarrow Z}$ is the calculated relative enthalpy (kJ/mol) between the most stable conformer of *E*- and *Z*-isomers.

	Inversion- <i>Th</i>	Inversion- <i>Ph</i>	Rotation	$\Delta H_{E \rightarrow Z}$
PAT-1	94.06	110.40	120.31	68.07
PAT-3	99.76	107.38	119.91	62.89
PAT-9	98.24	86.50	119.75	64.40
PAT-11	88.14	100.12	88.24	73.57
PAT-10	78.50	104.60	67.86	75.19

2.5 Reductant stability

For biological applications, the photoswitch should be stable in a reductive environment such as cell cytoplasm. Reductants such as DTT and glutathione may react at the azo moiety of the photoswitch resulting in hydrazine. We tested the stability of **1–3**, **9**, and **11** by incubating them in a mixture of BRB80 buffer and acetonitrile (50/50, v/v) containing DTT (0.1 mM) or glutathione (1 mM) reductants. The absorbance spectra were then measured before and after light irradiation (Figure 130 and 131). Interestingly, the absorbance originating from the azo chromophore remained unchanged, indicating the excellent stability of the *E* and *Z* isomers of **PATs** toward both DTT and glutathione reductants. However, the *Z* isomer of **9** with an electron-withdrawing CN group was unstable (Figure 130d).

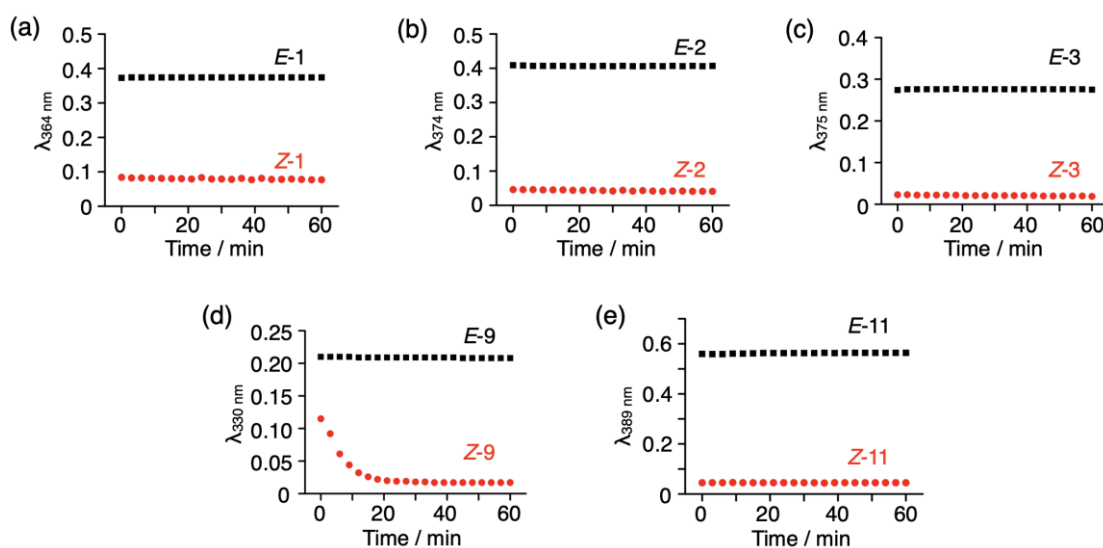


Figure 130. Absorbance changes of **1–3**, **9**, and **11** (20 μ M) over time after incubation for 60 min at 25°C in aqueous solution (BRB80 buffer: acetonitrile = 1:1 v/v) containing glutathione (1 mM) reductant. The black squares and red circles represent the absorbance before and after 405 nm light irradiation, respectively, followed by a 3-min incubation period before each measurement.

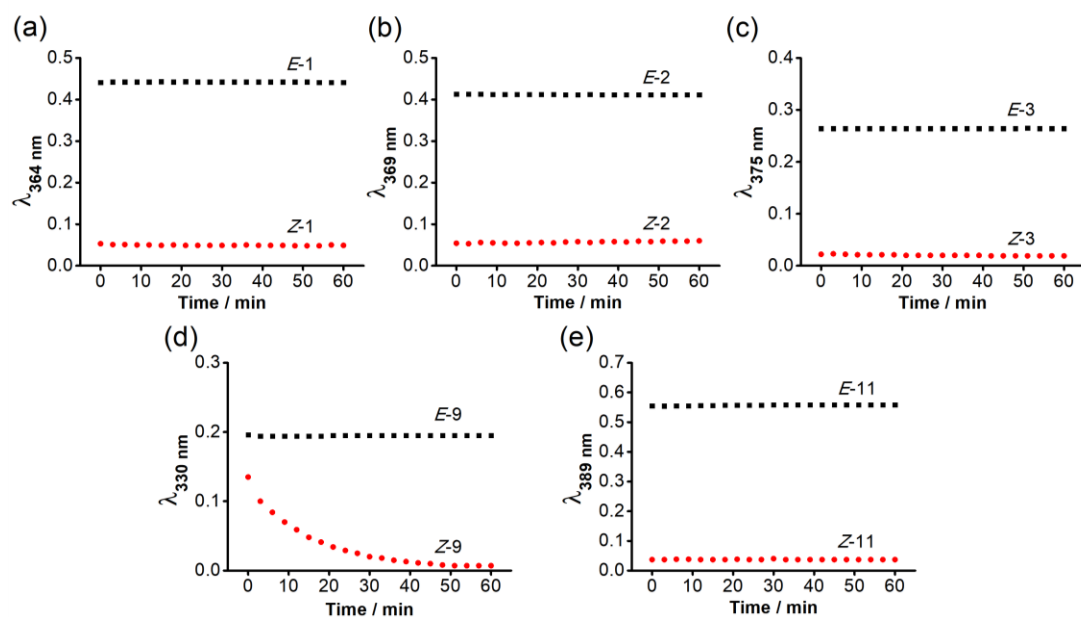


Figure 131. Graph showing the change in absorbance of PAT 1–3, 9 and 11 ($20 \mu\text{M}$) over time after incubation for 60 min at 25°C in aqueous solution (BRB80 buffer: acetonitrile = 1:1) containing DTT (0.1 mM) reductant. Black square and red circle represent the absorbance before and after 405 nm light irradiations followed by a 3-min incubation before each measurement, respectively.

3. Conclusions

We have demonstrated a novel class of five-membered “heteroaryl azo” photoswitches that reversibly isomerize on being exposed to visible light. The photoswitch with thiazole directly connected to a phenyl azo chromophore showed very different spectral characteristics than conventional azobenzene and other heteroaryl azo compounds. For instance, the λ_{\max} value ($\pi \rightarrow \pi^*$) of **1** was 363 nm, which is 47 nm and 35 nm redshifted compared with those of azobenzene and azopyrazole, respectively.³⁴ Furthermore, the spectral band attributed to the *E* and *Z* isomers of **1** was redshifted, allowing us to reversibly isomerize the photoswitch using visible-light (405 and 525 nm) irradiation, providing an excellent *E* and *Z* isomer ratio at the PSS and a long thermal half-life of the *Z* isomer. The photoswitch properties (λ_{\max} , $t_{1/2}$, and the PSS ratio) of **PAT** can be further tuned by introducing *ortho* and *para* substituents at the phenyl ring. In particular, **6**, having an *ortho* NH₂ substituent, showed reversible photoisomerization under longer wavelength visible light (525 and 625 nm) irradiation with a smaller thermal stability compensation effect and a longer half-life than visible-light switchable azobenzenes. Furthermore, **PAT** photoswitches showed excellent stability in the presence of reductants. Our calculation studies supported the experimental observations of the molecular energy parameters as well as the molecular geometries in both the *E* and *Z* isomers of the **PAT** photoswitches. We believe that the **PAT** class of photoswitches will provide unique applications, particularly in areas for which visible light is a requirement such as photopharmacology.⁷⁷ Such studies are currently underway.

4. Experimental section

4.1 Experimental and instrumental methods

Chemicals

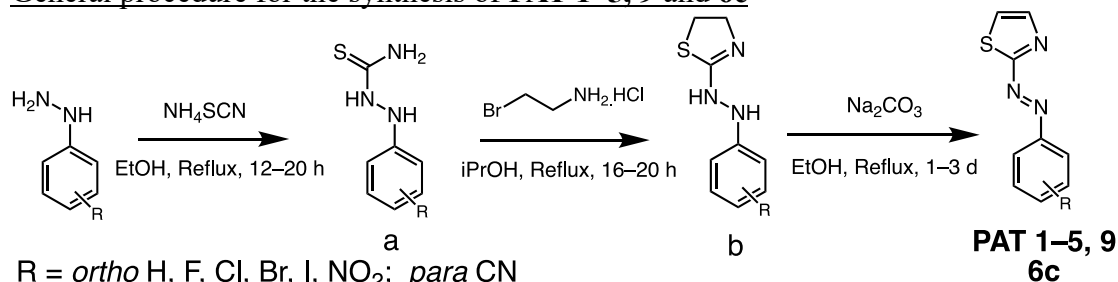
All reagents and solvents were purchased from commercial sources (FUJIFILM Wako Pure Chemical Corporation, Tokyo Chemical Industry, Merck, Kanto Chemical) and used without further purification.

Instrumentation

Reactions were monitored by thin-layer chromatography using TLC silica gel 60 F₂₅₄ (Merck). Column chromatography was performed using silica gel 60 N (spherical, neutral, 63-210 μ m, Kanto chemical). NMR spectra (¹H, ¹³C) were measured by a JEOL ECX-400 (400 or 600 MHz) spectrometer. A Shimadzu UV spectrophotometer (UV-1800) equipped with a TCC-100 Shimadzu temperature-controlled cell holder was used for UV-vis spectrophotometry. Photoisomerization studies of PAT derivatives were performed by a LED light source (Asahi Spectra, CL-1503) equipped with 405 nm, 430 nm, 470 nm, 525 nm and 625 nm LED heads. Flash photolysis experiments were carried out using a Q-switched Nd:YAG laser (Surelite I-10; Continuum).

4.2 Synthesis

General procedure for the synthesis of **PAT 1–5, 9** and **6c**



Scheme 2: Synthetic scheme for **PAT 1–5, 9** and **6c**.

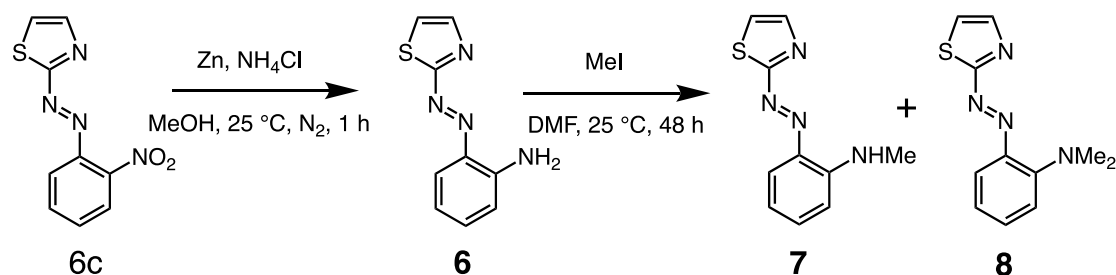
PAT 1–5, 9 and **6c** were synthesized according to a previously reported procedure with slight modifications.⁷⁸

a. Synthesis of 2-phenylhydrazine-1-carbothioamide derivatives: Phenylhydrazine hydrochloride (1.0 eq.) and ammonium thiocyanate (2.0 eq.) were suspended in a mixture of ethanol and water (9:1, v/v) [5 mL per 1 mmol of phenylhydrazine hydrochloride] and refluxed for 12–20 h. Then the solvent was removed under reduced pressure, add water to the residue, and the resulting precipitate was filtered, washed with water twice, and dried under vacuum to get pure 2-phenylhydrazine-1-carbothioamide derivatives.

b. Synthesis of 2-(2-phenylhydrazineyl)-4,5-dihydrothiazole derivatives: 2-phenylhydrazine-1-carbothioamide derivatives (1.0 eq.) and 2-bromoethylamine hydrobromide (1.0–1.2 eq.) were suspended in 2-propanol (5 mL per 1 mmol 2-bromoethylamine hydrobromide) and refluxed for 16–20 h. Precipitate formed was filtered off and the filtrate was evaporated under reduced pressure. The resulting residue was redissolved in hot water, added saturated sodium bicarbonate (pH >7) and cooled to room temperature. The slurry precipitate formed (containing the target compound) was extensively washed with water and dried under vacuum, which was directly used for the next reaction without further purification.

PAT. Synthesis of (*E*)-2-(phenyldiazenyl)thiazole derivatives: 2-(2-phenylhydrazineyl)-4,5-dihydrothiazole derivatives (1.0 eq.) and sodium carbonate (4.0 eq.) were suspended in ethanol (5 mL per 1 mmol sodium carbonate) and refluxed for 1–3 days. The solvent was removed by vacuum evaporation, add water to the residue, extracted the compound with ethyl acetate or dichloromethane, dried with MgSO₄, solvent removed by vacuum evaporation, and subjected to column chromatography on silica using the EtOAc (5–25%)/Hexane eluent to isolate pure compounds **PAT 1–5, 6c** and **8**. The oxidation reaction yield (<10%) of 4,5-dihydrothiazole compound to azothiazole compound was enhanced (>30%) in the synthesis of **PAT 4** and *o*-nitro derivative (**6C**) by using silver dioxide as oxidizing agent (4.0–8 eq, reflux in ethyl acetate or ethanol, 1–3 days) instead of air oxidation mentioned above.

Synthesis of **PAT 6 – 8**

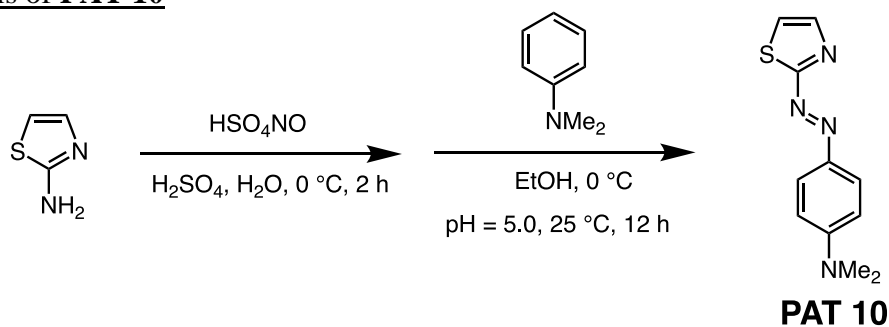


Scheme 3: Synthetic scheme for **PAT 6 – 8**.

PAT 6. The compound **6c** (100 mg, 0.4 mmol), ammonium chloride (70 mg, 1.3 mmol), and Zn powder (80 mg, 1.3 mmol) were mixed with dry MeOH (2 mL) under nitrogen atmosphere and stirred for 1 h at room temperature. The reaction mixture was then quenched with water and filtered through a celite bed. The filtrate was extracted with ethyl acetate, dried over anhydrous MgSO₄ followed by vacuum evaporation. The crude compound was then purified by silica gel column chromatography using 30% ethyl acetate in hexane solvent mixture (9 mg, yield = 10%).

PAT 7 and 8. The compound **6** (60 mg, 0.3 mmol) was mixed with K₂CO₃ (122 mg, 0.9 mmol) and dry DMF (2 mL) under nitrogen atmosphere. Methyl iodide (80 mg, 0.6 mmol) was added to this mixture dropwise and stirred for 48 hours at 25 °C. The reaction mixture was diluted with ethyl acetate and washed with water followed by brine solution. The organic layer was separated, dried over anhydrous MgSO₄ followed by vacuum evaporation. The crude compound containing both **PAT 7** and **8** was purified using silica gel column chromatography using 30% ethyl acetate in hexane solvent mixture **7** (4 mg, yield = 6%) and **8** (1.4 mg, yield = 2%).

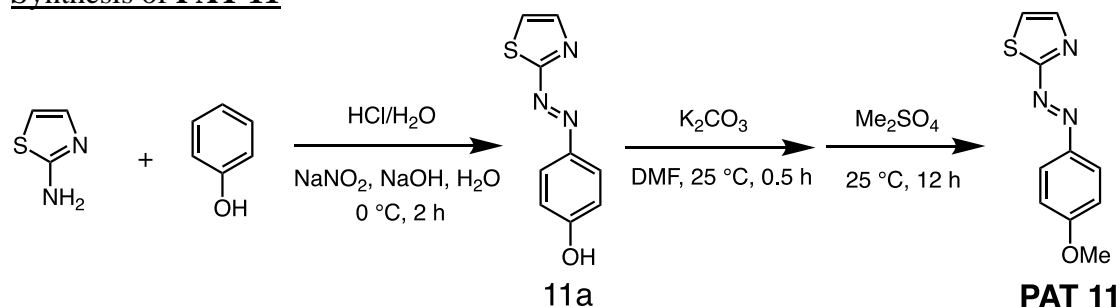
Synthesis of **PAT 10**



Scheme 4: Synthetic scheme of **PAT 10**.

PAT 10. Nitrosylsulfuric acid was prepared by adding sodium nitrite (1.1 g, 16 mmol) to the concentrated sulfuric acid (9.6 mL, 98%) followed by heating at $70\text{ }^\circ\text{C}$ and then cooling to $0\text{ }^\circ\text{C}$.⁷⁹ Separately, concentrated sulfuric acid (7.5 mL, 98%) was carefully added to an aqueous solution (150 mL) of 2-aminothiazole (2.0 g, 20 mmol) followed by cooling the solution to $0\text{ }^\circ\text{C}$. Nitrosylsulfuric acid was then slowly added to the above prepared 2-aminothiazole solution at $0\text{ }^\circ\text{C}$ and stirred for 2 hours at the same temperature. Then, EtOH solution (10 mL) of N, N-dimethylaniline (1.9 g, 16 mmol) was added at $0\text{ }^\circ\text{C}$, adjusted the pH to 5.0 using 1 M NaOH, and stirred for another 12 h at $25\text{ }^\circ\text{C}$. The crude product was extracted with ethyl acetate and purified by column chromatography on silica using EtOAc (50%) /Hexane eluent to isolate **PAT 10**.

Synthesis of **PAT 11**



Scheme 5: Synthetic scheme of **PAT 11**.

Compound 11a. 2-Aminothiazole (5.4 g, 54 mmol) was dissolved in a solution of deionized water (48 mL) and concentrated HCl (36%, 16 mL).⁸⁰ A mixed solution of sodium nitrite (3.9 g, 58 mmol), phenol (5.1 g, 54 mmol), sodium hydroxide (4.5 g, 0.11 mol) and deionized water was added dropwise to the above acidic solution at 0 °C and stirred for 2 h. The precipitate formed was filtered, and the crude product obtained was purified by column chromatography on silica using EtOAc (50%) /hexane eluent to isolate **11a**.

PAT 11. To a solution of compound **11a** (0.20 g, 0.98 mmol) in DMF (20 mL), potassium carbonate (270 mg, 1.96 mmol) was added. The mixture was stirred at room temperature for 30 min under nitrogen atmosphere. Dimethyl sulfate (0.12 g, 0.98 mmol) was then carefully added to the above mixture and stirred at room temperature for 12 h. Water was added to the reaction mixture, extracted with EtOAc, solvent removed by vacuum evaporation, and subjected to column chromatography on silica using EtOAc (30%)/hexane eluent to isolate pure **PAT 11**.

4.3 Measurement of isomer conversion at PSS by absorption spectra (PAT 11)

Due to short half-life of **PAT 11** (14 min at 25 °C), the isomer ratios at PSS obtained by NMR analysis were inaccurate and hence used the absorption spectroscopy for isomer ratios calculation at PSS. When the extinction coefficient of Z isomer of PAT 11 (ϵ_Z) at λ_{\max} (384 nm) was zero, then the isomer ratios at PSS was calculated using the equation:

$$\chi_E = \frac{A_0}{A_{PSS}}$$

χ_E E isomer ratio at PSS

A_0 Absorbance at initial state at λ_{\max}

A_{PSS} Absorbance at PSS at λ_{\max}

4.4 Methods for isomerization quantum yields

E–*Z* isomerization quantum yields were determined as follows

$$\phi_{E-Z} = \frac{\text{number of events}}{\text{number of photons absorbed}} = \frac{\text{number of } Z \text{ isomers formed (mol)}}{\text{number of photons absorbed (mol)}}$$

4.8a: Determination *Z* isomers formed

The *E*–*Z* conversion ratios were strictly kept minimum (5–10%) during the experiments to reduce the photons absorbed by *E* isomer. The number of *Z* isomers formed was calculated by the equation:

$$\text{Number of } Z \text{ isomers formed} = \frac{A_{BI} - A_{AI}}{(\varepsilon_E - \varepsilon_Z)l} V$$

A_{BI}	Absorbance at λ_{\max} before irradiation
A_{AI}	Absorbance at λ_{\max} after irradiation
ε_E	Extinction coefficient of <i>E</i> isomers at λ_{\max}
ε_Z	Extinction coefficient of <i>Z</i> isomers at λ_{\max}
l	Optical length of cuvette (<i>i.e.</i> 1 cm)
V	Total volume of the PAT solutions

Extinction coefficient at the λ_{\max} (ε_Z) can be obtained by following equation

$$\varepsilon_Z = \frac{A_{PSS} - A_0\chi_E}{c_0\chi_Z}$$

A_{PSS}	Absorbance at observation wavelength at 405 _{PSS}
A_0	Absorbance at observation wavelength before irradiation
c_0	Concentration of the PAT solutions
χ_E	<i>E</i> isomer ratio at 405 nm PSS (obtained by ¹ H NMR)
χ_Z	<i>Z</i> isomer ratio at 405 nm PSS (obtained by ¹ H NMR)

4.4b: Determination of absorbed photons

Actinometry: Ferrioxalate actinometer was used to determine the absorbed photons.⁸¹ Ferrioxalate actinometer solution in a round-shaped cuvette (total volume = 3.1 mL, optical path length = 1 cm) was placed in front of a square-shaped cuvette (optical path length = 1 cm) equipped with a magnetic stirring bar to capture all photons passing through the square cuvette. These two cuvettes were fixed on a metal base so that the position of two cuvettes remained same for all experiments. (see image below).

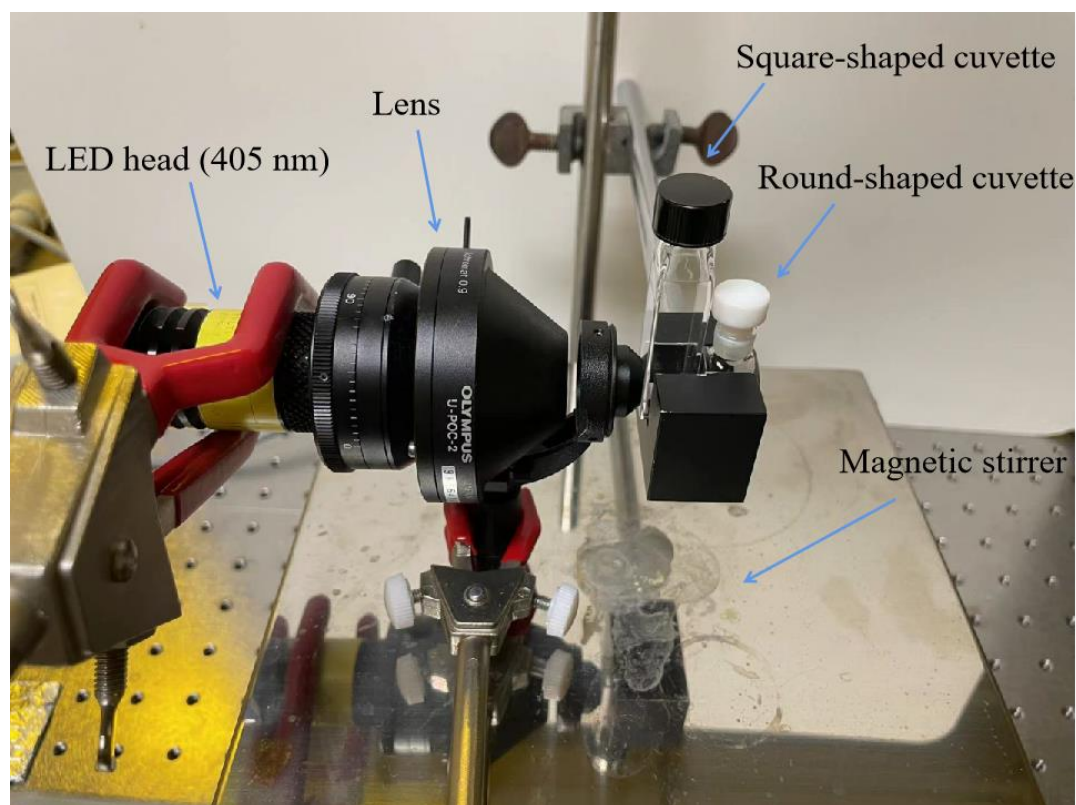


Figure 132: Experimental set up for quantum yield measurement. LED light source: (Asahi Spectra, CL-1503) equipped with 405 nm LED heads; Lens: Olympus microscope condenser U-POC-2.

4.4c: Procedure for the measurement

The procedure has two consecutive steps.

(1) Measurement of photon absorbed by blank solution. A 405 nm-light (0.15–0.56 W/cm²) was irradiated (60 sec) to the cuvettes containing blank solution (*i.e.* CH₃CN, 1.485 mL) in the square-shaped cuvette and ferrioxalate actinometer solution (0.15 M, 3 mL) in the round-shaped cuvette. Then manually shake the actinometer solution and transfer 1 mL of it to a glass vial and mix with sodium acetate buffer (0.15 M, 2 mL) containing phenanthroline (0.1 wt%, 300 µL). The mixed solution was incubated for ~60 min and measured absorbance at 510 nm using absorption spectroscopy.

(2) Measurement of photon absorbed by PAT sample solution. PAT stock solution (15 µL, 7.94 mM) was added to the same square-shaped cuvette containing CH₃CN solvent (1.485 mL) to prepare PAT sample solution (1.5 mL, 79.4 µM). A fresh ferrioxalate actinometer solution (0.15 M, 3 mL) was added into the round-shaped cuvette followed by light irradiation (405 nm, 0.15–0.56 W/cm², 60 sec). Then manually shake the actinometer solution and transfer 1 mL of it to a glass vial and mix with sodium acetate buffer (0.15 M, 2 mL) containing phenanthroline (0.1 wt%, 300 µL). The mixed solution was incubated for ~60 min and measured absorbance at 510 nm using absorption spectroscopy.⁸² All the experiments should be done in dark room (red light was used whenever necessary). We used the similar procedure for all the PAT derivatives. The number of absorbed photons was calculated using the equation:

$$\text{Photons absorbed} = \frac{(A_0 - A_1)V_1V_3}{\varepsilon_{510\text{ nm}}V_2\phi_{405\text{ nm}}}$$

A_0	Absorbance of ferrioxalate-phenanthroline solution at 510 nm (with blank solvent in the square-shaped cuvette)
A_1	Absorbance of ferrioxalate-phenanthroline solution at 510 nm (with PAT solutions in the square-shaped cuvette)
V_1	Volume of actinometer solution in round-shaped cuvette (<i>i.e.</i> 3 mL)
V_2	Volume of actinometer solution taken from round-shaped cuvette after irradiation (<i>i.e.</i> 1 mL)
V_3	Total volume of the ferrioxalate-phenanthroline solution (<i>i.e.</i> 3 mL).
$\varepsilon_{510\text{ nm}}$	Extinction coefficient of ferrioxalate-phenanthroline complex (ferroin) at 510 nm (obtained by calibration graph, $\varepsilon = 11410\text{ M}^{-1}\cdot\text{cm}^{-1}$ in our experimental condition) (Figure S52)
$\phi_{405\text{ nm}}$	Quantum yield of ferrioxalate actinometer at irradiation wavelength (1.14 at 405 nm)

4.4d: Method to calculate the *Z*–*E* quantum yields.

Z–*E* quantum yields were calculated by following equation in the case where the effect of thermal back isomerization reaction is negligible

$$\phi_{Z-E} = \frac{\chi_E \varepsilon'_E \phi_{E-Z}}{\varepsilon'_Z \chi_Z}$$

ε'_E Extinction coefficient of *E* isomers at irradiation wavelength

ε'_Z Extinction coefficient of *Z* isomers at irradiation wavelength

χ_E *E* isomer ratio at 405_{PSS} (obtained by ¹H NMR)

χ_Z *Z* isomer ratio at 405_{PSS} (obtained by ¹H NMR)

Extinction coefficient for the *Z*-isomer at irradiation wavelength (405 nm) (ε'_Z) can be obtained by following equation:

$$\varepsilon'_Z = \frac{A_{PSS} - A_0 \chi_E}{c_0 \chi_Z}$$

A_{PSS} Absorbance at observation wavelength at 405_{PSS}

A_0 Absorbance at observation wavelength before irradiation

c_0 Concentration of the PAT solutions

χ_E *E* isomer ratio at 405 nm PSS (obtained by ¹H NMR)

χ_Z *Z* isomer ratio at 405 nm PSS (obtained by ¹H NMR)

4.5 Half-lives, Arrhenius plots and Eyring Plots.

A freshly prepared solution was irradiated at 405_{PSS} or 470_{PSS} and immediately kept for thermal back Z–E isomerization in dark at temperatures (15, 20, 25, 30 and 35 °C for PAT 1–5; 16, 19, 22, 25 and 28 °C for PAT 6; 5, 10, 15, 20 and 25 °C for PAT 11). In all cases, 6–8 spectra at fixed time intervals were recorded in dark condition to minimize the effect of light beam on thermal back isomerization. Then, a first order rate constant (*k*) for the thermal back Z–E isomerization reaction was obtained using the equation

$$\ln \frac{A_t}{A_0} = \ln \frac{Abs(BI) - Abs(time)}{Abs(BI) - Abs(PSS)} = -kt$$

Abs(BI) = absorbance at initial state at λ_{max} .

Abs(PSS) = absorbance at photostationary state at λ_{max} .

Abs(time) = absorbance at λ_{max} at different time interval for thermal back isomerization from 405_{PSS}.

For a first order reaction, half-life ($t_{1/2}$) can be calculated using the equation:

$$t_{1/2} = \frac{0.693}{k}$$

Arrhenius equation was used to obtain activation energy (E_a) from $\ln k$ versus T^{-1} graph.

$$\ln k = -\frac{E_a}{R} \frac{1}{T} + \ln A$$

T = absolute temperature

A = pre-exponential factor

R = universal gas constant (8.314 J·K⁻¹·mol⁻¹)

Eyring equation was used to obtain entropy of activation (ΔS^\ddagger) and enthalpy of activation (ΔH^\ddagger) from $\ln k/T$ versus T^{-1} graph.

$$\ln \frac{k}{T} = -\frac{\Delta H^\ddagger}{R} \frac{1}{T} + \ln \frac{k_b}{h} + \frac{\Delta S^\ddagger}{R}$$

T = absolute temperature

k_b = Boltzmann constant (1.381 x 10⁻²³ J·K⁻¹)

h = Planck's constant (6.626 x 10⁻³⁴ J·Hz⁻¹).

The Gibbs free energy (ΔG^\ddagger) was obtained by the equation:

$$\Delta G^\ddagger = \Delta H^\ddagger - T \Delta S^\ddagger$$

4.6 Single crystal X-ray structure analysis.

Cryoloop was used to mount the single crystals. Crystallographic data was collected using a Rigaku XtaLab Synergy diffractometer with a single microfocus Mo K α X-ray radiation source (PhotonJet-S), equipped with a Hybrid Pixel (HyPix) Array detector (HyPix-6000HE). Data collection, cell refinement, and data reduction were carried out with CrysalisPRO (Rigaku Oxford Diffraction, 2017).

The initial structure was solved by SHELXT⁸³ and expanded using Fourier techniques and refined on F² by the full-matrix least-squares method SHELXL2018/3⁸⁴ package compiled into OLEX2 package.⁸⁵ All parameters were refined using anisotropic temperature factors, except for hydrogen atoms, which were refined using the riding model, with a fixed C–H bond distance.

CCDC 2201443 (*E*–1), 2201445 (*Z*–1), 2201444 (*E*–3) and 2201446 (*Z*–3) contain the supplementary crystallographic data for this paper.

5. References

- (1) Schwinghammer, T. L. et al. *Pharmacotherapy principles and practices*. McGraw-Hill, 2010.
- (2) Edwards, I. R.; Aronson, J. K. Adverse drug reactions: definitions, diagnosis, and management, *Lancet*, 2000, 356, 1255-1259.
- (3) Malhotra, V.; Perry, M. C. Classical Chemotherapy: Mechanisms, Toxicities and the Therapeutic Window, *Cancer Biol. Ther.* 2003, 2, S2-S4.
- (4) Longley, D. B.; Johnston, P. G. J. Molecular mechanisms of drug resistance, *Pathol.* 2005, 205, 275-292.
- (5) Deiters, A. Principles and applications of the photochemical control of cellular processes. *ChemBioChem*. 2010, 11, 47-53.
- (6) Mayer, G.; Heckel, A. Biologically active molecules with a “light switch”. *Angew. Chem. Int. Ed.* 2006, 45, 4900-4921.
- (7) Szymanski, W.; Beierle, J. M.; Kistemaker, H. A. V.; Velema, W. A.; Feringa, B. L. Reversible photocontrol of biological systems by the incorporation of molecular photoswitches. *Chem. Rev.* 2013, 113, 6114-6178.
- (8) Gardner, L.; Deiters, A. Light-controlled synthetic gene circuits. *Curr. Opin. Chem. Biol.* 2012, 16, 292-299.
- (9) Ackroyd, R.; Kelty, C.; Brown, N. and Reed M. The history of photodection and photodynamic therapy. *Photochem. Photobiol.* 2001, 74, 656-669.
- (10) MacDonald, I. J.; Dougherty, T. J. Basic principles of photodynamic therapy, *J. Porphyr. Phthalocyanines*, 2001, 5, 105-129.
- (11) Triesscheijn, M.; Baas, P.; Schellens, J. H. M.; Stewart, F. A. Photodynamic therapy in oncology. *Oncologist*, 2006, 11, 1034-1044.
- (12) Ellis-Davies, G. C. R. Caged compounds: photorelease technology for control of cellular chemistry and physiology. *Nat. Methods*, 2007, 4, 619-628.
- (13) Klan, P.; Solomek, T.; Bochet, C. G.; Blanc, A.; Givens, R.; Rubina, M.; Popik, V.; Kostikov, A.; Wirz, Photoremovable protecting groups in chemistry and biology: reaction mechanisms and efficacy. *J. Chem. Rev.* 2012, 113, 119-191.
- (14) Brieke, C.; Rohrbach, F.; Gottschalk, A.; Mayer, G. and Heckel, Light-controlled tools. *A. Angew. Chem., Int. Ed.* 2012, 51, 8446-8476.
- (15) Velema, W. A.; Szymanski, W.; Feringa, B. L. Photopharmacology: Beyond proof of principle. *J. Am. Chem. Soc.* 2014, 136, 2178–2191.
- (16) Velema, W.; Berg, J. V. D.; Hansen, M.; Szymanski, W.; Driessen, A. and Feringa, B. L. Optical control of antibacterial activity. *Nat. Chem.* 2013, 5, 924-928.
- (17) Mafy, N. N.; Matsuo, K.; Hiruma, S.; Uehara, R. and Tamaoki, N. Photoswitchable CENP-E inhibitor enabling the dynamic control of chromosome movement and mitotic progression. *J. Am. Chem. Soc.* 2020, 142, 1763-1767.
- (18) Fuchter, M. J. On the promise of photopharmacology using photoswitches: a medicinal chemist’s perspective. *J. Med. Chem.* 2020, 63, 11436-11447.
- (19) Hull, K.; Morstein, J. and Trauner, D. In vivo photopharmacology. *Chem. Rev.* 2018, 118, 10710-10747.
- (20) Knie, C.; Utecht, M.; Zhao, F.; Kulla, H.; Kovalenko, S.; Brouwer, A. M.; Saalfrank, P.; Hecht, S.; Bléger, D. ortho-Fluoroazobenzenes: Visible light switches with very long-Lived Z isomers. *Chemistry* 2014, 20, 16492–16501.
- (21) Bandara, H. M. D. and Burdette, S. C. Photoisomerization in different classes of azobenzene. *Chem. Soc. Rev.* 2012, 41, 1809-1825.

- (22) Irie, M.; Fulcaminato, T.; Matsuda, K.; Kobatake, S. Photochromism of diarylethene molecules and crystals: memories, switches, and actuators. *Chem. Rev.* 2014, 114, 12174–12277.
- (23) Klajn, R. Spiropyran-based dynamic materials. *Chem. Soc. Rev.* 2014, 43, 148–184.
- (24) Waldeck, D. H. Photoisomerization dynamics of stilbenes. *Chem. Rev.* 1991, 91, 415–436.
- (25) Hartley, G. S. The Cis-form of Azobenzene. *Nature*, 1937, 140, 281.
- (26) Cheng, H.; Yoon, J.; Tian, H. Recent advances in the use of photochromic dyes for photocontrol in biomedicine. *Coord. Chem. Rev.* 2018, 372, 66–84.
- (27) Welleman, I. M.; Hoorens, M. W. H.; Feringa, B. L.; Boersma, H. H.; Szymański, W. Photoresponsive molecular tools for emerging applications of light in medicine. *Chem. Sci.* 2020, 11, 11672–11691.
- (28) Volarić, J.; Szymanski, W.; Simeth, N. A.; Feringa, B. L. Molecular photoswitches in aqueous environments. *Chem. Soc. Rev.* 2021, 50, 12377–12449.
- (29) Thayyil, S.; Nishigami, Y.; Islam, M. J.; Hashim, P. K.; Furuta, K.; Oiwa, K.; Yu, J.; Yao, M.; Nakagaki, T.; Tamaoki, N. Dynamic control of microbial movement by photoswitchable ATP antagonists. *Chemistry* 2022, 28, e202200807.
- (30) Broichhagen, J.; Frank, J. A.; Trauner, D. A roadmap to success in photopharmacology. *Acc. Chem. Res.* 2015, 48, 1947–1960.
- (31) Hüll, K.; Morstein, J.; Trauner, D. In vivo photopharmacology. *Chem. Rev.* 2018, 118, 10710–10747.
- (32) Hammerich, M.; Schütt, C.; Stähler, C.; Lenters, P.; Röhricht, F.; Höppner, R.; Herges, R. Heterodiazocines: Synthesis and photochromic properties, trans to cis switching within the bio-optical window. *J. Am. Chem. Soc.* 2016, 138, 13111–13114.
- (33) Bandara, H. M.; Burdette, S. C. Photoisomerization in different classes of azobenzene. *Chem. Soc. Rev.* 2012, 41, 1809–1825.
- (34) Sadovski, O.; Beharry, A. A.; Zhang, F.; Woolley, G. A. Spectral tuning of azobenzene photoswitches for biological applications. *Angew. Chem. Int Ed Engl* 2009, 48, 1484–1486.
- (35) Beharry, A. A.; Sadovski, O.; Woolley, G. A. Azobenzene photoswitching without ultraviolet light. *J. Am. Chem. Soc.* 2011, 133, 19684–19687.
- (36) Samanta, S.; Beharry, A. A.; Sadovski, O.; McCormick, T. M.; Babalhavaeji, A.; Tropepe, V.; Woolley, G. A. Photoswitching azo compounds in vivo with red light. *J. Am. Chem. Soc.* 2013, 135, 9777–9784.
- (37) Bléger, D.; Schwarz, J.; Brouwer, A. M.; Hecht, S. o-Fluoroazobenzenes as readily synthesized photoswitches offering nearly quantitative two-way isomerization with visible light. *J. Am. Chem. Soc.* 2012, 134, 20597–20600.
- (38) Dong, M.; Babalhavaeji, A.; Samanta, S.; Beharry, A. A.; Woolley, G. A. Red-shifting azobenzene photoswitches for in vivo use. *Acc. Chem. Res.* 2015, 48, 2662–2670.
- (39) Dong, M.; Babalhavaeji, A.; Collins, C. V.; Jarrah, K.; Sadovski, O.; Dai, Q.; Woolley, G. A. Near-infrared photoswitching of azobenzenes under physiological conditions. *J. Am. Chem. Soc.* 2017, 139, 13483–13486.
- (40) Lameijer, L. N.; Budzak, S.; Simeth, N. A.; Hansen, M. J.; Feringa, B. L.; Jacquemin, D.; Szymanski, W. General Principles for the Design of Visible-Light-Responsive Photoswitches: Tetra-ortho-Chloro-Azobenzenes. *Angew. Chem. Int Ed Engl* 2020, 59, 21663–21670.

- (41) Crespi, S.; Simeth, N. A.; König, B. Heteroaryl azo dyes as molecular photoswitches. *Nat. Rev. Chem.* 2019, 3, 133–146.
- (42) Schütt, C.; Heitmann, G.; Wendler, T.; Krahwinkel, B.; Herges, R. Design and Synthesis of Photodissociable Ligands Based on Azoimidazoles for Light-Driven Coordination-Induced Spin State Switching in Homogeneous Solution. *J. Org. Chem.* 2016, 81, 1206–1215.
- (43) Devi, S.; Saraswat, M.; Grewal, S.; Venkataramani, S. Evaluation of Substituent Effect in Z-Isomer Stability of Arylazo-1 H-3,5-dimethylpyrazoles: Interplay of Steric, Electronic Effects and Hydrogen Bonding. *J. Org. Chem.* 2018, 83, 4307–4322.
- (44) Heindl, A. H.; Wegner, H. A. Rational Design of Azothiophenes-Substitution Effects on the Switching Properties. *Chemistry* 2020, 26, 13730–13737.
- (45) Gaur, A. K.; Kumar, H.; Gupta, D.; Tom, I. P.; Nampoothiry, D. N.; Thakur, S. K.; Mahadevan, A.; Singh, S.; Venkataramani, S. Structure–property relationship for visible light bidirectional photoswitchable azoheteroarenes and thermal stability of Z-isomers. *J. Org. Chem.* 2022, 87, 6541–6551.
- (46) Naim, M. J.; Alam, O.; Nawaz, F.; Alam, M. J.; Alam, P. Current status of pyrazole and its biological activities. *J. Pharm. Bioallied Sci.* 2016, 8, 2–17.
- (47) Alghamdi, S. S.; Suliman, R. S.; Almutairi, K.; Kahtani, K.; Aljatli, D. Imidazole as a promising medicinal scaffold: Current status and future direction. *Drug Des. Devel. Ther.* 2021, 15, 3289–3312.
- (48) Zhang, H. Z.; Zhao, Z. L.; Zhou, C. H. Recent advance in oxazole-based medicinal chemistry. *Eur. J. Med. Chem.* 2018, 144, 444–492.
- (49) Vitaku, E.; Smith, D. T.; Njardarson, J. T. Analysis of the structural diversity, substitution patterns, and frequency of nitrogen heterocycles among U.S. FDA approved pharmaceuticals. *J. Med. Chem.* 2014, 57, 10257–10274.
- (50) Bhunia, S.; Dolai, A.; Samanta, S. Robust bi-directional photoswitching of thiomethyl substituted arylazopyrazoles under visible light. *Chem. Commun. (Camb)* 2020, 56, 10247–10250.
- (51) Yang, Y.; Hughes, R. P.; Aprahamian, I. Near-infrared light activated azo-BF₂ switches. *J. Am. Chem. Soc.* 2014, 136, 13190–13193.
- (52) Weston, C. E.; Richardson, R. D.; Haycock, P. R.; White, A. J.; Fuchter, M. J. Arylazopyrazoles: Azoheteroarene photoswitches offering quantitative isomerization and long thermal half-lives. *J. Am. Chem. Soc.* 2014, 136, 11878–11881.
- (53) Otsuki, J.; Suwa, K.; Sarker, K. K.; Sinha, C. Photoisomerization and thermal isomerization of arylazoimidazoles. *J. Phys. Chem. A* 2007, 111, 1403, 1403–1409.
- (54) Calbo, J.; Weston, C. E.; White, A. J. P.; Rzepa, H. S.; Contreras-García, J.; Fuchter, M. J. Tuning Azoheteroarene Photoswitch Performance through Heteroaryl Design. *J. Am. Chem. Soc.* 2017, 139, 1261–1274.
- (55) Weston, C. E.; Richardson, R. D.; Fuchter, M. J. Photoswitchable basicity through the use of azoheteroarenes. *Chem. Commun.* 2016, 52, 4521–4524.
- (56) (a) Fang, D.; Zhang, Z. Y.; Shangguan, Z.; He, Y.; Yu, C.; Li, T. (Hetero)arylazo-1,2,3-triazoles: “Clicked” Photoswitches for Versatile Functionalization and Electronic Decoupling. *J. Am. Chem. Soc.* 2021, 143, 14502–14510. (b) He, Y.; Shangguan, Z.; Zhang, Z. Y.; Xie, M.; Yu, C.; Li, T. Azobispyrazole Family as Photoswitches Combining (Near-) Quantitative Bidirectional Isomerization and

- Widely Tunable Thermal Half-Lives from Hours to Years*. *Angew. Chem. Int Ed Engl* 2021, 60, 16539–16546.
- (57) Tuck, J. R.; Tombari, R. J.; Yardeny, N.; Olson, D. E. A modular approach to arylazo-1,2,3-triazole photoswitches. *Org. Lett.* 2021, 23, 4305–4310.
- (58) Slavov, C.; Yang, C.; Heindl, A. H.; Wegner, H. A.; Dreuw, A.; Wachtveitl, J. Thiophenylazobenzene: An Alternative Photoisomerization Controlled by Lone-Pair $\cdots \pi$ Interaction. *Angew. Chem. Int. Ed.* 2020, 59, 380–387.
- (59) Kumar, P.; Srivastava, A.; Sah, C.; Devi, S.; Venkataramani, S. Arylazo-3,5-dimethylisoxazoles: Azoheteroarene photoswitches exhibiting high Z-isomer stability, solid-state photochromism, and reversible light-induced phase transition. *Chem. Eur. J.* 2019, 25, 11924–11932.
- (60) Kennedy, A. D. W.; Sandler, I.; Andréasson, J.; Ho, J.; Beves, J. E. Visible-light photoswitching by Azobenzazoles. *Chemistry* 2020, 26, 1103–1110.
- (61) (a) Garcia-Amorós, J.; Maerz, B.; Reig, M.; Cuadrado, A.; Blancafort, L.; Samoylova, E.; Velasco, D. Picosecond switchable azo dyes. *Chemistry* 2019, 25, 7726–7732.
- (62) Schehr, M.; Ianes, C.; Weisner, J.; Heintze, L.; Müller, M. P.; Pichlo, C.; Charl, J.; Brunstein, E.; Ewert, J.; Lehr, M.; Baumann, U.; Rauh, D.; Knippschild, U.; Peifer, C.; Herges, R. 2-Azo-, 2-diazocine-thiazols and 2-azo-imidazoles as photoswitchable kinase inhibitors: Limitations and pitfalls of the photoswitchable inhibitor approach. *Photochem. Photobiol. Sci.* 2019, 18, 1398–1407.
- (63) Matsuo, K.; Thayyil, S.; Kawaguchi, M.; Nakagawa, H.; Tamaoki, N. A visible light-controllable Rho kinase inhibitor based on a photochromic phenylazothiazole. *Chem. Commun. (Camb)* 2021, 57, 12500–12503.
- (64) Wu, M. T.; Wakszynski, F. S.; Hoff, D. R.; Fisher, M. H.; Egerton, J. R.; Patchett, A. A. Anthelmintic 2-Arylhydrazino- and 2-Arylazo-2-thiazolines. *J. Pharm. Sci.* 1977, 66, 1150–1153.
- (65) Whitten, D. G.; Wildes, P. D.; Pacifici, J. G.; Irick, G. Solvent and substituent on the thermal isomerization of substituted azobenzenes. Flash spectroscopic study. *J. Am. Chem. Soc.* 1971, 93, 2004–2008.
- (66) Zhou, F.; Liu, R.; Li, P.; Zhang, H. On the properties of $S\cdots O$ and $S\cdots \pi$ noncovalent interactions: The analysis of geometry, interaction energy and electron density. *New J. Chem.* 2015, 39, 1611–1618.
- (67) Motherwell, W. B.; Moreno, R. B.; Pavlakos, I.; Arendorf, J. R. T.; Arif, T.; Tizzard, G. J.; Coles, S. J.; Aliev, A. E. Noncovalent interactions of π systems with sulfur: The atomic chameleon of molecular recognition. *Angew. Chem. Int Ed Engl* 2018, 57, 1193–1198.
- (68) The calculation result for the frontier molecular orbitals showing that the energy difference between n orbital and π^* (HOMO-1 and LUMO) is larger than that between π and π^* (HOMO and LUMO) seems to be inconsistent with the fact that n- π^* transition band appear at lower energy region than π - π^* . But this can be ascribed to the difference in exciton binding energies. see ref 40(b).
- (69) Bureš, F. Fundamental aspects of property tuning in push-pull molecules. *RSC Adv.* 2014, 4, 58826–58851.
- (70) M. J. Frisch, G. W. Trucks, H. B. Schlegel, G. E. S.; M. A. Robb, J. R. Cheeseman, G. Scalmani, V. Barone, B. M.; G. A. Petersson, H. Nakatsuji, M. Caricato, X. Li, H. P. H.; A. F. Izmaylov, J. Bloino, G. Zheng, J. L. Sonnenberg, M. H.; M.

- Ehara, K. Toyota, R. Fukuda, J. Hasegawa, M. Ishida, T. N.; Y. Honda, O. Kitao, H. Nakai, T. Vreven, J. A. Montgomery, J.; J. E. Peralta, F. Ogliaro, M. Bearpark, J. J. Heyd, E. B.; K. N. Kudin, V. N. Staroverov, T. Keith, R. Kobayashi, J. N.; K. Raghavachari, A. Rendell, J. C. Burant, S. S. Iyengar, J. T.; M. Cossi, N. Rega, J. M. Millam, M. Klene, J. E. Knox, J. B. C.; V. Bakken, C. Adamo, J. Jaramillo, R. Gomperts, R. E. S.; O. Yazyev, A. J. Austin, R. Cammi, C. Pomelli, J. W. O.; R. L. Martin, K. Morokuma, V. G. Zakrzewski, G. A. V.; P. Salvador, J. J. Dannenberg, S. Dapprich, A. D. D.; O. Farkas, J. B. Foresman, J. V. Ortiz, J. C.; Fox., and D. J. Gaussian 09, Revision D.01. Gaussian, Inc., Wallingford CT 2013.
- (71) Roy Dennington, Todd A. Keith, and J. M. M. GaussView, Version 6.1. Semichem Inc., Shawnee Mission, KS 2016.
- (72) Hohenberg, P.; Kohn, W. Inhomogeneous Electron Gas. *Phys. Rev.* 1964, 136 (3B), B864. <https://doi.org/10.1103/PHYSREV.136.B864/FIGURE/1/THUMB>.
- (73) Gross, E. K. U.; Dobson, J. F.; Petersilka, M. Density Functional Theory of Time-Dependent Phenomena. *Density Funct. Theory II* 1996, 81–172. <https://doi.org/10.1007/BFB0016643>.
- (74) Kohn, W.; Sham, L. J. Self-Consistent Equations Including Exchange and Correlation Effects. *Phys. Rev.* 1965, 140 (4A), A1133. <https://doi.org/10.1103/PHYSREV.140.A1133/FIGURE/1/THUMB>.
- (75) Lee, C.; Yang, W.; Parr, R. G. Development of the Colle-Salvetti Correlation-Energy Formula into a Functional of the Electron Density. *Phys. Rev. B* 1988, 37 (2), 785. <https://doi.org/10.1103/PhysRevB.37.785>.
- (76) Miertuš, S.; Scrocco, E.; Tomasi, J. Electrostatic Interaction of a Solute with a Continuum. A Direct Utilizaion of AB Initio Molecular Potentials for the Prevision of Solvent Effects. *Chem. Phys.* 1981, 55 (1), 117–129. [https://doi.org/10.1016/0301-0104\(81\)85090-2](https://doi.org/10.1016/0301-0104(81)85090-2).
- (77) Sharma, P. C.; Bansal, K. K.; Sharma, A.; Sharma, D.; Deep, A. Thiazole-containing compounds as therapeutic targets for cancer therapy. *Eur. J. Med. Chem.* 2020, 188, 112016.
- (78) M.T. Wu, F.S. Waksmunski, D.R. Hoff, M.H. Fisher, J.R. Egerton, A.A. Patchett, *J. Pharm. Sci.*, 1977, 66, 1150–1153.
- (79) Masaki Matsui, Mitsugu Kushida, Kazumasa Funabiki, Katsuyoshi Shibata, Hiroshige Muramatsu, Kazuo Hirota, Masahiro Hosoda, Kazuo Tai, *Dyes Pigm.*, 1998, 37, 283–289.
- (80) Heyun Huang, Fei Chen, Zhiming Chen, Mengjun Jiang, *Polym. Bull.*, 2016, 73, 1545–1552.
- (81) C. G. Hatchard, C. A. Parker, *Proc. R. Soc. Lond. A*, 1956, 235, 518–536.
- (82) Günter Gauglitz, Stephan Hubig, *J. Photochem.*, 1985, 30, 121–125.
- (83) G. M. Sheldrick, *Acta. Cryst.*, 2015, A71, 3–8.
- (84) G. M. Sheldrick, *Acta. Cryst.*, 2015, C71, 3–8.
- (85) O. V. Dolomanov, L. J. Bourhis, R. J. Gildea, J. A. K. Howard, H. Puschmann, *J. Appl. Cryst.*, 2009, 42, 339–341.